A NUMERICAL STUDY OF VORTICITY-ENHANCED HEAT TRANSFER

A Thesis
Presented to
The Academic Faculty

by

Xiaolin Wang

In Partial Fulfillment
of the Requirements for the Degree
Doctor of Philosophy in
Computational Science and Engineering

School of Mathematics
Georgia Institute of Technology
August 2014

A NUMERICAL STUDY OF VORTICITY-ENHANCED HEAT TRANSFER

Approved by:

Haomin Zhou, Committee Chair
School of Mathematics
Georgia Institute of Technology

Haomin Zhou, Advisor
School of Mathematics
Georgia Institute of Technology

Silas Alben
School of Mathematics
University of Michigan

Yingjie Liu
School of Mathematics
Georgia Institute of Technology

Edmond Chow
School of Computational Science and Engineering
Georgia Institute of Technology

Jack Poulson
School of Computational Science and Engineering
Georgia Institute of Technology

Date Approved: 24 June 2014

To my parents

ACKNOWLEDGEMENTS

I would like to thank my advisor, Dr. Haomin Zhou, and co-advisor, Dr. Silas Alben, for many stimulating conversations, for sharing their enthusiasm for mathematics, and for the invaluable guidance and patience in completing this research.

It's a pleasure to thank Dr. Howie Weiss for involving me in the research of microbial population dynamics and providing me the opportunity to explore wider research topics. I'm grateful to Dr. Yingjie Liu for many inspiring discussions on numerical schemes and methods. I would also like to thank the other members of my committee, Dr. Edmond Chow and Dr. Jack Poulson for sharing their insights in scientific computing and providing valuable ideas on my research. I am truly indebted to the grad-coordinators of school of mathematics, Dr. Luca Dieci and Dr. John Etnyre for their help and guidance in many academic and non-academic issues.

I thank Yunlong He and Jingfang Liu for many inspiring discussions and perspectives on scientific computing, and I also thank Qingqing Liu and Rundong Du for stimulating office conversations and great help in many aspects. My friends have always been a source of entertainment, exploration, and stress release. Those of note are Ruidong Wang, Ruodu Wang, Qianyi Wang, Yi Xiao, Weizhe Zhang, Da Kuang, Danjue Chen, Mengni Zhang, Yushu Wang, Tao Wu. I especially want to thank Ying Liu, Mengdie Hu and Liwei Zhang for their great accompanies as roommates.

Finally, I'm deeply grateful to my father and mother for all the support that they have given me through the years. You have kept me who I am.

TABLE OF CONTENTS

LIST OF TABLES

LIST OF FIGURES

SUMMARY

In this work, we have numerically studied the effect of the vorticity on the enhancement of heat transfer in a channel flow. In the first part of the work, we focus on the investigation of a channel flow with a vortex street as the incoming flow. We propose a model to simulate the fluid dynamics. We find that the flow exhibits different properties depending on the value of four dimensionless parameters. In particularly, we can classify the flows into two types, active and passive vibration, based on the sign of the incoming vortices.

In the active vibration cases, we find that vortex blobs are able to maintain the same spatial structures as the inflow and mainly move in the downstream direction. In the passive vibration cases, the vortex blobs move towards the centerline and exchange their positions in the channel due to the interactions between the blobs and the separated vortices from the wall. Based on the flow's spatial and temporal properties, the passive vibration cases can be further identified as regular, irregular or non-periodic street. The flow of the regular street cases has symmetric time-averaged vorticity while it is asymmetric in the irregular street cases. The transition happens as the separated vortices become strong enough that the interactions between separated vortices are comparable to those between the blob and the wall separations.

In the second part of the work, we discuss the heat transfer process due to the flows just described and investigate how the vorticity in the flow improves the efficiency of the heat transfer. The temperature shows different characteristics corresponding to the active and passive vibration cases.

In active vibration cases, the vortex blob improves the heat transfer by disrupting the thermal boundary layer and preventing the decay of the wall temperature gradient

throughout the channel, and by enhancing the forced convection to cool down the wall temperature. The heat transfer performance is directly related to the strength of the vortex blobs and the background flow. In passive vibration cases, the corresponding heat transfer process is complicated and varies dramatically as the flow changes its properties.

Compared to the fluid parameters, we find that the thermal parameters of the solids have much less effect on the heat transfer enhancement. The thermal properties of the fluid on the other hand play an important role to determine the amount of the heat transfer by convection and by conduction. The Nusselt number can be largely improved by increasing the Péclet number of the fluid. However, this turns out to be a challenging task for commonly used fluid medium such as air or water. We realize that we can achieve the same heat transfer performance by simply adding vortices in the incoming flow, and this is an important result of our current work.

Finally, we propose a more realistic optimization problem which is to minimize the maximum temperature of the solids with a given input energy. Kinetic energy flux of the incoming flow is applied as a measurement for the input energy. We find that the best heat transfer performance is obtained in the active vibration case with zero background flow.

CHAPTER I

INTRODUCTION

Vorticity-enhanced heat transfer is drawing more and more interest these days. Due to the increased processing power of compact electronic devices, natural convection is not able to provide enough cooling for such devices, and heat sinks with better heat transfer efficiency are thus required.

The idea of enhancing heat transfer by vorticity has been studied for years, and much experimental, numerical and theoretical work has been carried out on the subject. This problem includes fundamental issues in both the fluid dynamics and the heat transfer process. In the first part of the work, we focus on the properties of the channel flows, as understanding of the fluid properties provides useful insights in characterizing the heat transfer process.

To simplify the problem, we only consider the 2-D channel heat sink where the heat source is placed on both channel walls. This model is simpler than the actual fin-shaped heat sinks that are used in most electronic equipment. However, we can treat the channel heat sink as the cross section of the straight fin heat sink viewed from the top, and therefore the results of the current work can provide useful information in the actual 3-D model.

In a channel flow, vortices are generated as the flow passes a vortex generator which can be either a bluff body or a vibrating plate. There are numerous previous works about the vortex shedding behind a bluff body. As early as the 1900s, Mallock [46] reported the observation of a vortex wake consist of alternating "right-handed" and "left-handed" eddies behind a cylinder. The vortex wake that consists of such zigzagging patterns of opposite signed vortices is named a "von Kármán vortex street"

as von Kármán first proposed a point vortex model to approximate such a street structure in inviscid flow [75]. The von Kármán street turns out to be a successful model in inviscid flow, and people have applied it to analyze the characteristics of vortex shedding by different body shapes including a cylinder [60], square [19] and inclined flat plate [36]. There are many studies concerning the vortex shedding in viscous flows as well. Some of the interesting topics include the formation of the vortex wakes [26, 69, 52], numerical methods for simulating vortex shedding by different body shapes [62, 39], shear layer instabilities and different different vortex wake structures [50, 76], etc.

Another type of vortex generator induces vortices by a vibrating plate. Depending on the rigidity of the plate, the Reynolds number, the frequency of the vibration and some other parameters, the vibrating plate can generate distinct vortex wakes from von Kármán street to reversed von Kármán street and to even more complicated patterns [37]. Schnipper *et al.* showed six different vortex wakes obtained by pitching oscillations of a foil in a vertically flowing soap film for different Strouhal numbers and amplitudes of the vibration [61]. Godoy *et al.* obtained a similar phase diagram which shows the transitions between vortex wakes as well [30].

Among those different vortex wakes, we are particularly interested in the vibration that leads to either the von Kármán street or the reversed von Kármán street. The former one is analogous to the vortex wake behind a bluff body and is often obtained by flapping of a flexible body through fluid-solid interactions [7, 21, 63]. This phenomena is first observed by Taneda [68] and later re-examined by Zhang *et al.* [80] where the flag and the corresponding vortices are visualized in a gravity-driven soap-film tunnel. Alben *et al.* [5] and Michelin *et al.* [48] showed the regime in which the motion of the flag is periodic and the von Kármán street is shed from the trailing edge of the flag. Their models are different which leads to different parameter description of the regime, but their results are in a good agreement with respect to

the positions of the centres of shed vorticity.

Under proper conditions [6], a vibrating plate can create a reversed von Kármán street in its wake. The fundamental mechanism of the flow induced by such a plate was outlined by Lighthill [43] where he discussed fish propulsion through the thrust force derived from the movement of the tail. This type of vibration has drawn tremendous attention in recent years, especially in the community of bio-fluids, as the flapping foil provides the basic source of locomotion and maneuvering forces in the flying and swimming of animals [73, 74].

Both types of vortex generators have wide applications in heat transfer enhancement. Li [41] performed numerical calculations to determine the variation of Nusselt number when a square cylinder is placed in a channel flow. He was able to obtain an increase of 42% in Nusselt number with the cylinder over a channel compared to the one without the cylinder. Fiebig *et al.* examined the effect of delta and rectangular wings, and found an increased of near 60% in global Nusselt number for a pair of delta-wing-shaped vortex generators. He also determined that the increase in Nusselt number is linear with the Reynolds number [25].

Recently, many new studies have been carried out on utilizing piezoelectrically-driven fans or actuators to enhance the heat transfer in microelectronics cooling. A common piezo-actuator is a thin plate with piezoelectric material bonded to it. When excited by an alternating signal, the piezo-material contracts and expands, causing the plate to vibrate accordingly. Açıkalın *et al.* measured the heat transfer performance of a surface that was placed perpendicular to the piezo-fan [2]. They developed a numerical model for such settings and found that the heat transfer performance depended on the strength of the shed vortex and the distance from the fan to the surface. They were able to decrease the temperature of the surface from $340K$ to $300K$ in the best performance. Gerty *et al.* placed the piezo-plate in the center of the channel and found that the local Nusselt number is improved throughout the channel

with the maximum improvement obtained at the end of the channel [29]. Liu *et al.* measured heat transfer on a flat surface under different fan-to-surface arrangements [44]. One is placed perpendicular to the surface and the other is placed parallel to the surface. They concluded that heat transfer augmentation was due to air flow entrained during each oscillation cycle and by jet-like air streams at the fan tip; with the two modes of heat transfer enhancement being nearly equivalent.

Given the fact that many studies have been conducted on the vorticity enhanced heat transfer, we realize that there are still several aspects of the problem that require further investigations. First, most of the previous work in the vortex wake focuses either on the formation mechanism of the vortices shed from the vortex generator, or on the development of the flows in an unbounded region. There are only several studies considering the development of the von Kármán street in a bounded channel [16, 64, 66, 67], and even fewer results for the reversed von Kármán street. Secondly, most previous works only study a specific type of vortex generator and its corresponding heat transfer enhancement without comparison between different types. This is reasonable as the fluid models are different for each vortex generator, especially between a vibrating plate and a bluff body. Therefore it is almost impossible to measure the heat transfer enhancement based a uniform criteria.

In this work, we first proposed a model to simulate the fluid dynamics of the channel flow. In particularly, our model can be applied to any type of vortex generators given that certain information about the shed vorticity can be obtained. Then we discuss the numerical method for solving the model. We apply the model to cases corresponding to different vortex dynamics, and discuss the behavior of the flow in the channel, especially how the wall confinement affects its dynamics under different fluid parameters. After that, we consider the temperature properties induced by the flow. We compare the heat transfer performance within large fluid and temperature parameter spaces. Finally, we propose an optimization problem which measures the

best heat transfer performance under certain conditions.

The current work is organized as the follows: Chapter II describes the model for the 2-D channel flow and discusses the numerical methods. Chapter III focuses on the analysis of flow properties. The temperature model is studied in Chapter IV as well as the results for heat transfer enhancement, and the conclusions follow in Chapter V.

CHAPTER II

MODEL OF THE 2-D CHANNEL FLOW

The study of the vortex enhanced heat transfer includes both the fluid dynamics and the heat transfer processes. The first part of the current work focuses on the properties of the induced flow. In this chapter, a model is proposed to simulate the vortex dynamics of a channel flow and a numerical method is discussed to solve the model.

2.1 Model

We model the fluid dynamics of a two-dimensional viscous flow in a channel. The channel is of length L and height H, and the fluid has kinematic viscosity ν. The flow satisfies the two-dimensional Navier-Stokes equations:

$$\frac{\partial \omega}{\partial t} + \mathbf{u} \cdot \nabla \omega = \nu \Delta \omega, \tag{1}$$

$$-\Delta \psi = \omega. \tag{2}$$

Here $\omega(x, y, t)$ and $\psi(x, y, t)$ denote the vorticity and the stream function of the flow respectively. The velocity $\mathbf{u} = (u, v)$ is obtained from the stream function by

$$u(x, y) = \frac{\partial \psi}{\partial y}, \quad v(x, y) = -\frac{\partial \psi}{\partial x}. \tag{3}$$

A schematic figure of the computational domain is shown in figure 1.

2.2 Boundary Conditions

To solve the Navier-Stokes equations, we need to propose proper boundary conditions for ω and ψ on each boundary. We first discretize the channel with a $N \times M$ spatial grid which has N points on the x direction and M points on the y direction. The

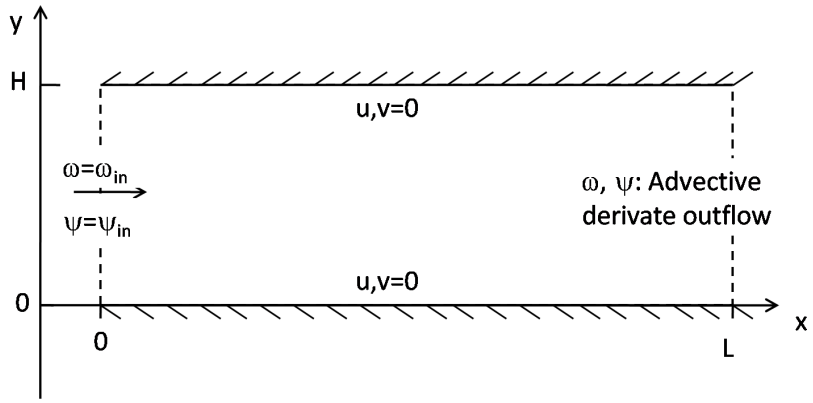

Figure 1: Schematic of the computational domain. The channel has a length L and height H. Dirichlet boundary conditions are applied at the entrance of the channel. No penetration and no slip conditions are used at the walls and advective derivative conditions are applied to both ω and ψ at the outflow.

indices $(1,1),(N,1),(M,N)$ and $(1,M)$ indicate the lower left, lower right, upper right and upper left corner of the computational domain respectively.

2.2.1 Wall Boundary Conditions

No slip and no penetration boundary conditions are applied for the velocity at the upper and lower wall boundaries of the channel:

$$u = \frac{\partial \psi}{\partial y} = 0 \tag{4}$$

$$v = -\frac{\partial \psi}{\partial x} = 0 \tag{5}$$

It turns out that both conditions are imposed on the stream function ψ while none is for the vorticity ω. To obtain a boundary condition for ω, Briley [12] proposed a fourth-order formula for the vorticity boundary values by using the near-boundary stream function values:

$$\omega_{i,1} = \frac{1}{18h^2}(85\psi_{i,1} - 108\psi_{i,2} + 27\psi_{i,3} - 4\psi_{i,4}) \quad \equiv \quad \omega_{i,1}^B \tag{6}$$

$$\omega_{i,M} = \frac{1}{18h^2}(85\psi_{i,M} - 108\psi_{i,M-1} + 27\psi_{i,M-2} - 4\psi_{i,M-3}) \quad \equiv \quad \omega_{i,M}^B. \tag{7}$$

Here $h = 1/(M-1)$ denotes the uniform grid spacing in the y direction. Equations (6) and (7) hold for any $i = 1, 2, \ldots, N$. Briley's formula is obtained by discretizing

Table 1: Summary of Variants of Thom's Formula

Reference	$\omega - \psi$ formulation
Thom [72], Burggraft [14]	$\omega_1 = \frac{2}{h^2}(\psi_1 - \psi_2)$
Woods [77]	$\frac{2}{3}\omega_1 = -\frac{1}{3}\psi_2 + \frac{2}{h^2}(\psi_1 - \psi_2)$
D'alessio and Dennis [23]	$\frac{1}{2}\omega_1 = -\frac{2}{3}\psi_2 + \frac{1}{6}\psi_3 + \frac{2}{h^2}(\psi_1 - \psi_2)$
Jensen [35]	$\omega_1 = \frac{1}{2h^2}(7\psi_1 - 8\psi_2 + \psi_3)$
Briley [12]	$\omega_1 = \frac{1}{18h^2}(85\psi_1 - 108\psi_2 + 27\psi_3 - 4\psi_4)$

the no slip condition $\partial\psi/\partial y = 0$ with a fourth-order finite difference approximation and then applying it to equation (2). It gives a Dirichlet boundary condition for ω. Further study shows that Briley's formula is able to provide a second-order-accurate value for ω on the boundary when the other equations are discretized with a second-order scheme [49].

Briley's formula is a variant of Thom's formula [72] where the Neumann condition $\partial\psi/\partial y = 0$ is approximated by finite difference schemes and then coupled with equation (2) on the boundary to get the value of ω. There are many variants of Thom's formula depending on the schemes to approximate the Neumann condition and equation of ψ [24, 49]. We list some of the well-known formulas in Table 1. The advantage of using a fourth-order instead of a second-order formula was discussed by Napolitano [49] as he reported smaller global errors in two numerical examples when using high-order scheme.

At the same time, the no-penetration condition $\partial\psi/\partial x = 0$ lead to a Dirichlet boundary condition for ψ as:

$$\psi_{i,1} = \psi_{1,1}, \quad \psi_{i,M} = \psi_{1,M}, \quad \forall i = 1, 2, \cdots, N \tag{8}$$

2.2.2 Outflow Boundary Conditions

Imposing proper boundary conditions for the outflow is a numerical challenge as we need to truncate the infinite length of flow into a finite computational domain. The boundary conditions therefore should approximate the flow conditions for an infinite

channel at the outflow boundary location.

If the outflow is laminar and the length of the channel is sufficient long, the flow will eventually become a Poiseuille flow at the exit with a moderate Reynolds number. The critical Reynolds number to guarantee a laminar flow depends on the flow geometry. For example, for a straight pipe with a circular cross-section, the laminar flow occurs when Re is smaller than 2100 [8, 34]. For the parallel flow in the straight channel, the critical Reynolds number is 2300 [10]. In such cases, the natural boundary condition is a good choice as discussed in [31, 71]:

$$\partial_{\mathbf{n}}\omega = 0, \quad \partial_n\psi = 0 \tag{9}$$

where $\mathbf{n}$ is the outward normal coordinate at the exit. This indicates that the vertical velocity v equals zero at the exit, which is true for fully developed steady laminar channel flows. However, when the channel is not long enough or the vorticity is strong inside the channel, the flow can still be transient at the outer boundary, and conditions based on unsteady problems are therefore required. Much previous work has been carried out on the proper outflow conditions in this case. Baker [9] developed the "least constraining condition" which sets the normal derivatives of u and v to zero at the boundary. Thus boundary conditions for ω and ψ become:

$$\frac{\partial\omega}{\partial\mathbf{n}} = \nabla\times\frac{\partial\mathbf{u}}{\partial\mathbf{n}} = 0 \tag{10}$$

$$\frac{\partial^2\psi}{\partial^2\mathbf{s}} = \Delta\psi - \frac{\partial^2\psi}{\partial^2\mathbf{n}} = -\omega \tag{11}$$

where $\mathbf{s}$ is the tangential coordinate along the boundary curve. Equation (11) can be easily solved numerically at the boundary with the condition that ψ = constant at the two end points of the boundary curve. Tezduyar *et al.* rewrote the "traction-free" conditions (i.e., zero normal and shear stress) for velocity-pressure variables into $\omega-\psi$ variables and applied it to the outflow condition [70, 71]. Ol'Shanskii and Staroverov [51] suggested using "drift conditions" for unsteady, viscous non-linear flow. A drift

condition is a transport type of equation

$$\frac{\partial \mathbf{u}}{\partial t} + U(\mathbf{x})\frac{\partial \mathbf{u}}{\partial \mathbf{n}} = 0 \tag{12}$$

$U(\mathbf{x})$ is the drift function and is the velocity of some known typical flow like Poiseuille flow or uniform flow.

In this work, we apply the advective derivative condition [11, 20, 59] for ω and ψ at the outflow boundary. Sani and Gresho [59] first proposed this condition for velocity variables:

$$\frac{\partial \mathbf{u}}{\partial t} + c\frac{\partial \mathbf{u}}{\partial \mathbf{n}} = 0 \tag{13}$$

where c is some average velocity, for example, they suggested using the averaged streamwise velocity across the exit, $\bar{u}$ [59]. This is a special type of drift condition where the drift function $U(\mathbf{x}) = c$. Later Comini *et al.* [20] derived the conditions for ω and ψ based on equation (13). By taking the curl of equation (13), we obtain the advective derivative condition for ω:

$$\frac{\partial \omega}{\partial t} + \bar{u}\frac{\partial \omega}{\partial n} = 0, \tag{14}$$

For the ψ equation, we used the fact that $v = -\partial\psi/\partial x$ and $\psi_{xx} = -\psi_{yy} - \omega$ to obtain that:

$$\frac{\partial}{\partial t}\left(\frac{\partial \psi}{\partial x}\right) + \bar{u}\left(-\frac{\partial^2 \psi}{\partial y^2} - \omega\right) = 0 \tag{15}$$

This equation is numerically solvable at the boundary given the condition that $\psi =$ constant at the two end points, which is naturally satisfied with the no-penetration condition on the wall. We also note that for steady flow, equations (14) and (15) are the same as the least constraining condition discussed above.

To illustrate the effect of the outflow boundary conditions, we show the results of our numerical scheme for different channel lengths $L = 4$ and $L = 8$, and plot the value of the vorticity, the stream-function, and the velocities at $x = 4$ across the channel in figures 2 and 3, for two different incoming flows: active and passive vibration cases.

Details of the numerical solver and the incoming flows will be discussed in the next sections. When $L = 4$, the values occur at the boundary points while when $L = 8$, the values occur at interior points.

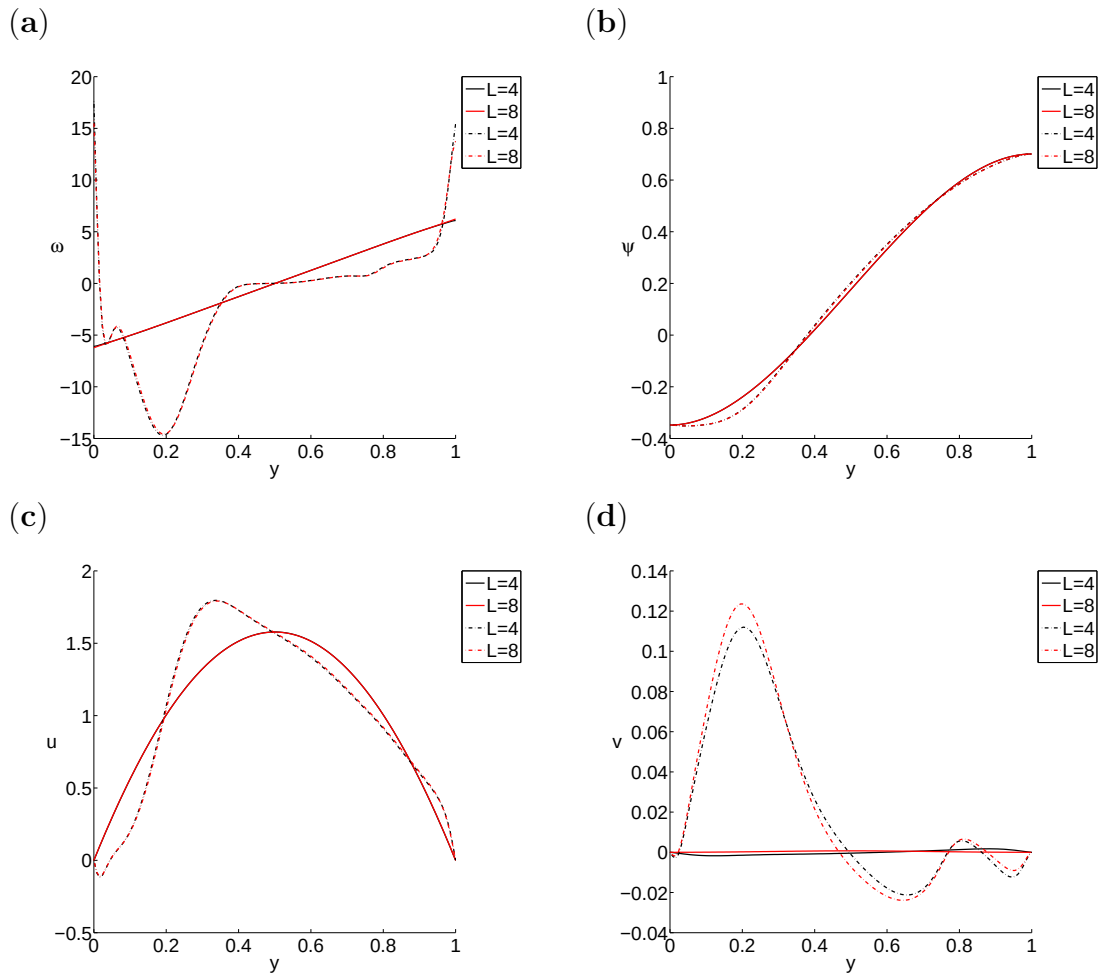

Figure 2: Values of the vorticity, stream-function, and velocities at $L = 4$ and $L = 8$ for active vibration cases with different Reynolds numbers. The solid lines indicate values for $Re = 20$ and the dashed lines show values for $Re = 1000$. (a) ω; (b) ψ; (c) u; (d) v.

In both figures, we notice that the values of ω, ψ and u at location $x = 4$ agree very well for different channel lengths. The values of v on the other hand have larger discrepancies. This numerical error is expected as v is neglected in the advective derivative conditions. The advantage of the condition is that this numerical error will only affect a local region close to the exit and will not cause discrepancies further

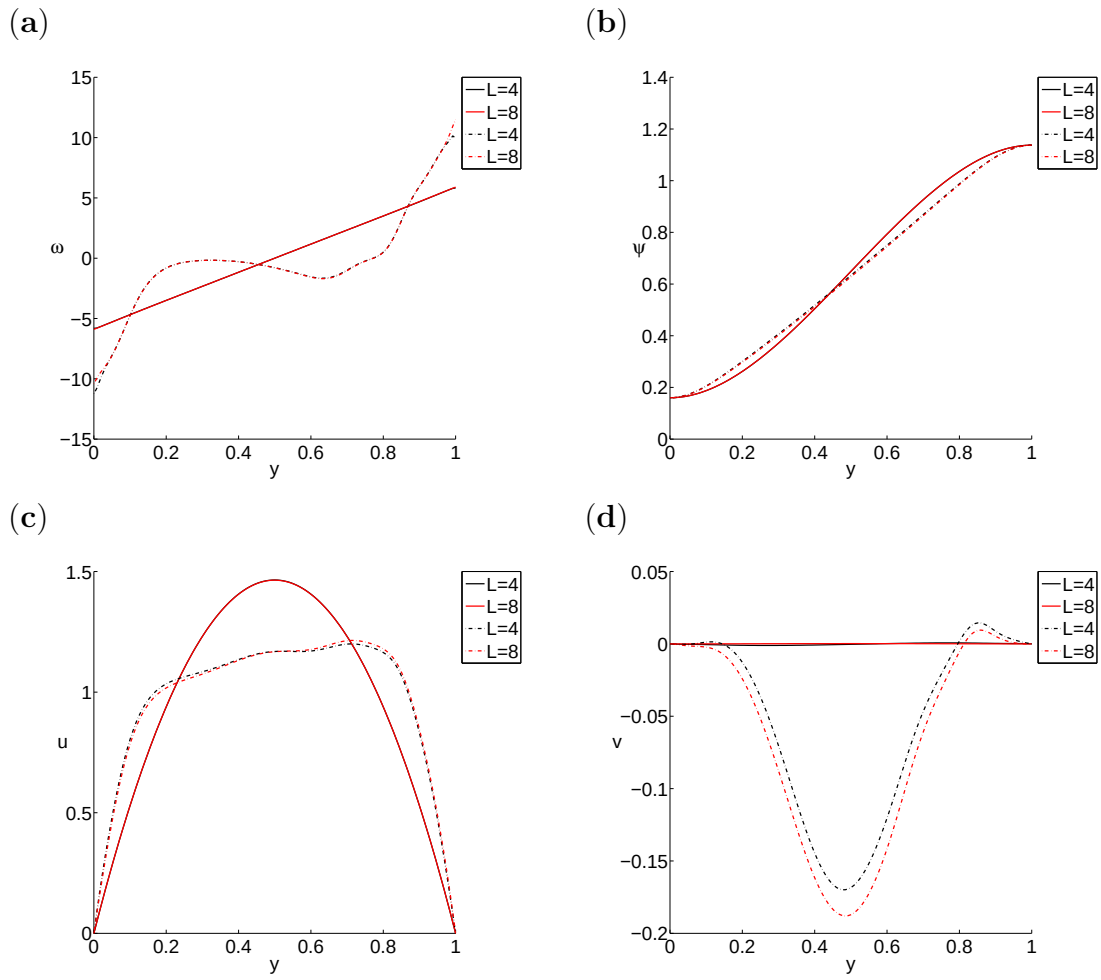

Figure 3: Values of the vorticity, stream-function, and velocities at $L = 4$ and $L = 8$ for passive vibration cases with different Reynolds numbers. The solid lines indicate values for $Re = 20$ and the dashed lines show values for $Re = 1000$. (a) ω; (b) ψ; (c) u; (d) v.

upstream [59]. In figure 4 we compare the value of vertical velocity v at $x = 3$ again for different channel lengths $L = 4$ and $L = 8$ for both active and passive vibration cases. The value of v is identical at this location and illustrates that the effect of the outflow condition is constrained only to the outflow boundary.

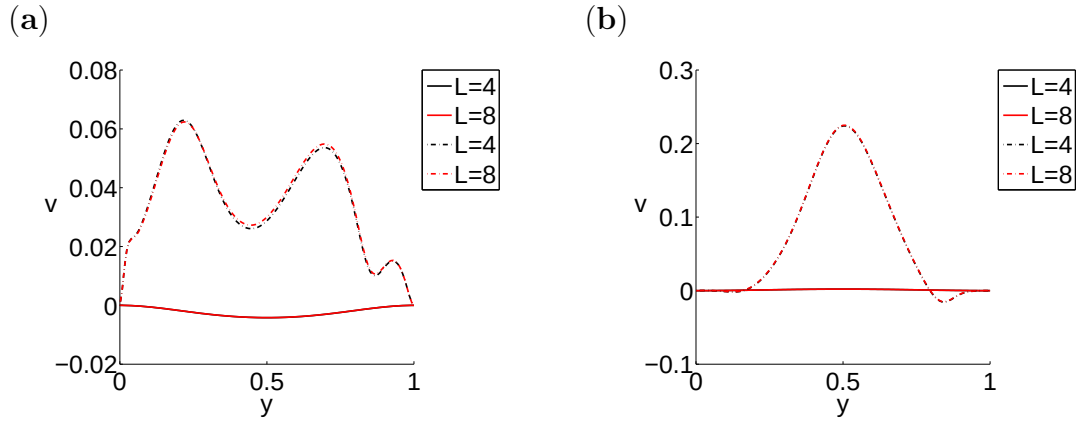

Figure 4: Values of the vertical velocity v at $L = 4$ and $L = 8$ with different Reynolds numbers. The solid lines indicate values for $Re = 20$ and the dashed lines show values for $Re = 1000$. (a) Active vibration; (b) Passive vibration.

2.2.3 Inflow Boundary Conditions

Finally, we discuss how to impose the inflow boundary conditions for the computation. We want to approximate the situation where some type of vortex generator is placed in front of the channel so that vortices are produced and driven into the channel as an imposed flow. In this work, we do not specify the type of vortex generators. They can be a bluff body like a cylinder, a square or a triangle, or a rigid or elastic vibrated plate. The only information required is the property of the flows that are produced by such vortex generators. In general, two types of vortex wakes will be generated by the vortex generators, a reversed von Kármán vortex street and a regular von Kármán vortex street. Many experimental, numerical and theoretical work has been conducted on this subject [22, 50, 53, 76, 61, 63]. People have discussed the mechanisms of the formation of such vortex street, its geometric property and pattern, the stability conditions to maintain the street and so on.

We define all the cases where a reversed von Kármán vortex street is generated as "active vibration", since a plate vibrated by external forces often produces such a vortex wake at the trailing edge [13, 30, 37, 61, 78]. And we define the cases where a von Kármán vortex street is generated as "passive vibration" since a plate vibrated passively by a fluid-solid interaction will generate such wakes [4, 7, 21, 63]. Therefore we impose the inflow vorticity ω_{in} and stream function ψ_{in} boundary conditions in such a way that they approximate the actual vortex wake that enters the channel.

In inviscid flow, a fully formed von Kármán vortex street is represented by two arrays of point vortices with the same strengths and opposite signs placed in staggered locations as shown in figure 5.

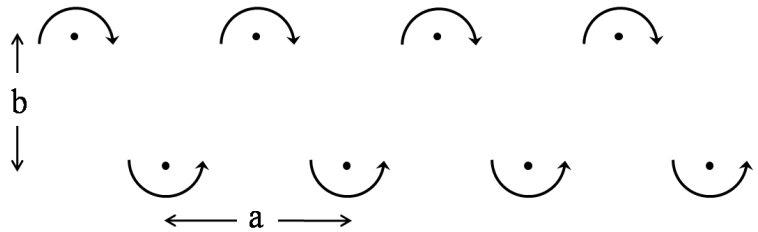

Figure 5: Point vortex representation of a von Kármán street.

Such flow can be represented by a complex potential [1, 57] as:

$$w = \phi + i\psi = \frac{i\Gamma}{2\pi}\log\left(\sin\frac{\pi}{a}(z - z_0)\right) - \frac{i\Gamma}{2\pi}\log\left(\sin\frac{\pi}{a}\left(z - z_0 - \frac{1}{2}a - ib\right)\right) \quad (16)$$

and the corresponding complex velocity is obtained by taking derivative of w:

$$\frac{dw}{dz} = u - iv(z) = \frac{i\Gamma}{2a}\cot\left(\frac{\pi}{a}(z - z_0)\right) - \frac{i\Gamma}{2a}\cot\left(\frac{\pi}{a}\left(z - z_0 - \frac{1}{2}a - ib\right)\right) \quad (17)$$

where the point vortices with strength Γ are placed at $z = z_0 + (m + \frac{1}{2})a + ib$, and those with strengths $-\Gamma$ are placed at $z = z_0 + ma, m = 0, \pm1, \pm2, \cdots$. When Γ is positive, this leads to the reverse von Kármán street while negative Γ gives the complex velocity for the regular von Kármán street. The velocity derived in equation (17) is singular at the point vortex regions due to the singularity of the cotangent

function. However the point vortex itself has a finite velocity because the vortex does not induce velocity at its center [1, 57]. The velocity at $z = z_0$ is

$$U_p = \frac{\Gamma}{2a} \tanh \frac{\pi b}{a} \tag{18}$$

By symmetry, each vortex moves with the same velocity U_p relative to the flow at infinity. The flow is periodic with a period length a. Adding the background flow U_b, we can rewrite the complex velocity as

$$u(z) - iv(z) = U_b + \frac{i\Gamma}{2a} \cot\left(\frac{\pi}{a}(z - z_0)\right) - \frac{i\Gamma}{2a} \cot\left(\frac{\pi}{a}\left(z - z_0 - \frac{1}{2}a - ib\right)\right) \tag{19}$$

with the point vortex velocity

$$U = U_b + \frac{\Gamma}{2a} \tanh \frac{\pi b}{a} \tag{20}$$

It should be noted that for a von Kármán street with Γ negative, the point vortices will generate a velocity in the upstream direction. Therefore, the background flow is necessary for the vortices to move in the downstream direction.

In simulations of viscous flow, the vortex blob method is a common method in which the point vortices are replaced by vortices with finite length cores to account for diffusion by viscosity [38, 40, 57]. In this method, the vorticity is treated as a collection of individual vortex blobs and the motion of the blobs are then determined by the vortex induced flow. The vortex blob method has a good accuracy for viscous flow. Hald [33] showed that as the blob's radius tends to zero, the solution converges to the solution of the Euler equations. On the other hand, the method is also computationally cost as it requires evaluation on each individual blob and their interactions.

Since the inflow only provides a boundary condition for the computation and the full Navier-Stokes equations is solved in the channel, we do not apply the vortex blob method directly to the inflow. Instead, we apply the idea of the vortex blob to seek

for an approximate solution which is computationally efficient but still carries the important properties of the inflow.

We replace the point vortices in equation (19) by vortex blobs with a finite radius δ. The velocity inside the blob is then computed by subtracting the point-vortex induced singularity from the von Kármán street solution and adding a desingularized kernel to account for viscous diffusion. The complex velocity inside the pth blob is defined as:

$$u - iv(z) = u_{vk}(z) - \frac{i\Gamma}{2\pi}\frac{1}{z - z_p} + \frac{i\Gamma}{2\pi}\frac{\bar{z} - \bar{z}_p}{\|z - z_p\|^2 + \delta^2} \tag{21}$$

Here u_{vk} denotes the von Kármá street solution given in equation (19), and z_p is the location of the pth blob. The δ-term is an artificial smoothing kernel that regularizes the point vortex. It is an analogous to the desingularized kernel used by Krasny [38]. And as $\delta \to 0$ the velocity is expected to converge to the solution of a point vortex model. In the region 2δ away from the vortex blob, we keep the velocity unchanged as for the point vortex von Kárman street in equation (19). And a Hermite interpolation is used to obtain a smooth transition between the two different velocities. A schematic figure of the vortex blob model is shown in figure 6. The vortex blobs still move

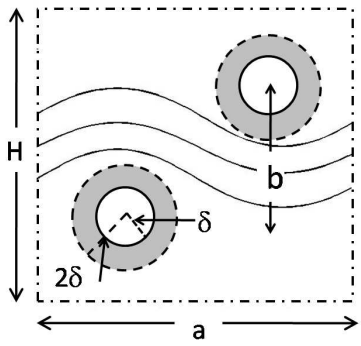

Figure 6: A schematic figure of the vortex blob model. The blobs have radii of δ. The horizontal and vertical displacement between two blobs are $\frac{1}{2}a$ and b respectively. H is the height of the channel and the flow is periodic with period length a.

downstream with the same velocity

$$U = U_b + \frac{\Gamma}{2a} \tanh \frac{\pi b}{a} \tag{22}$$

because the blob does not contribute to its own velocity and all the other vortex blobs are 2δ away and their contributions are the same as the point vortex model.

Similarly, inside the pth blob, the stream function and the vorticity are:

$$\psi = \psi_{vk} + \frac{\Gamma}{2\pi} \log(\|z - z_p\|) - \frac{\Gamma}{2\pi} \log(\sqrt{\|z - z_p\|^2 + \delta^2}) \tag{23}$$

$$\omega = \frac{\Gamma \delta^2}{\pi(\|z - z_p\|^2 + \delta^2)^2} \tag{24}$$

In the region 2δ away from the vortex blob, we still use complex potential of the von Kármán street for ψ and set $\omega = 0$. And Hermite interpolations are applied for a smooth transition between different profiles.

The inflow modeled as above is periodic in x (with length a) and time (with period $\tau_p = a/U$). It is a good approximation of the early stage of the vortex street when the viscosity only exhibit a local diffusion effect. In the actual numerical simulation, we pre-compute the values of the velocities, voriticy and stream function over one period, and then at each time instant t, we choose the values corresponding to t and use them as a Dirichlet boundary condition $\omega = \omega_{in}, \psi = \psi_{in}, u = u_{in}$ and $v = v_{in}$.

In figure 7 and 8, we plot the value of velocities, vorticity and stream function at three time instants $t = 1/4\tau_p$, $t = 1/2\tau_p$ and $t = 3/4\tau_p$, for active and passive vibration cases respectively. We also show the velocity field and the contour plot of the vorticity in one period in both figures.

We summarize and list all the boundary conditions for solving the fluid equations

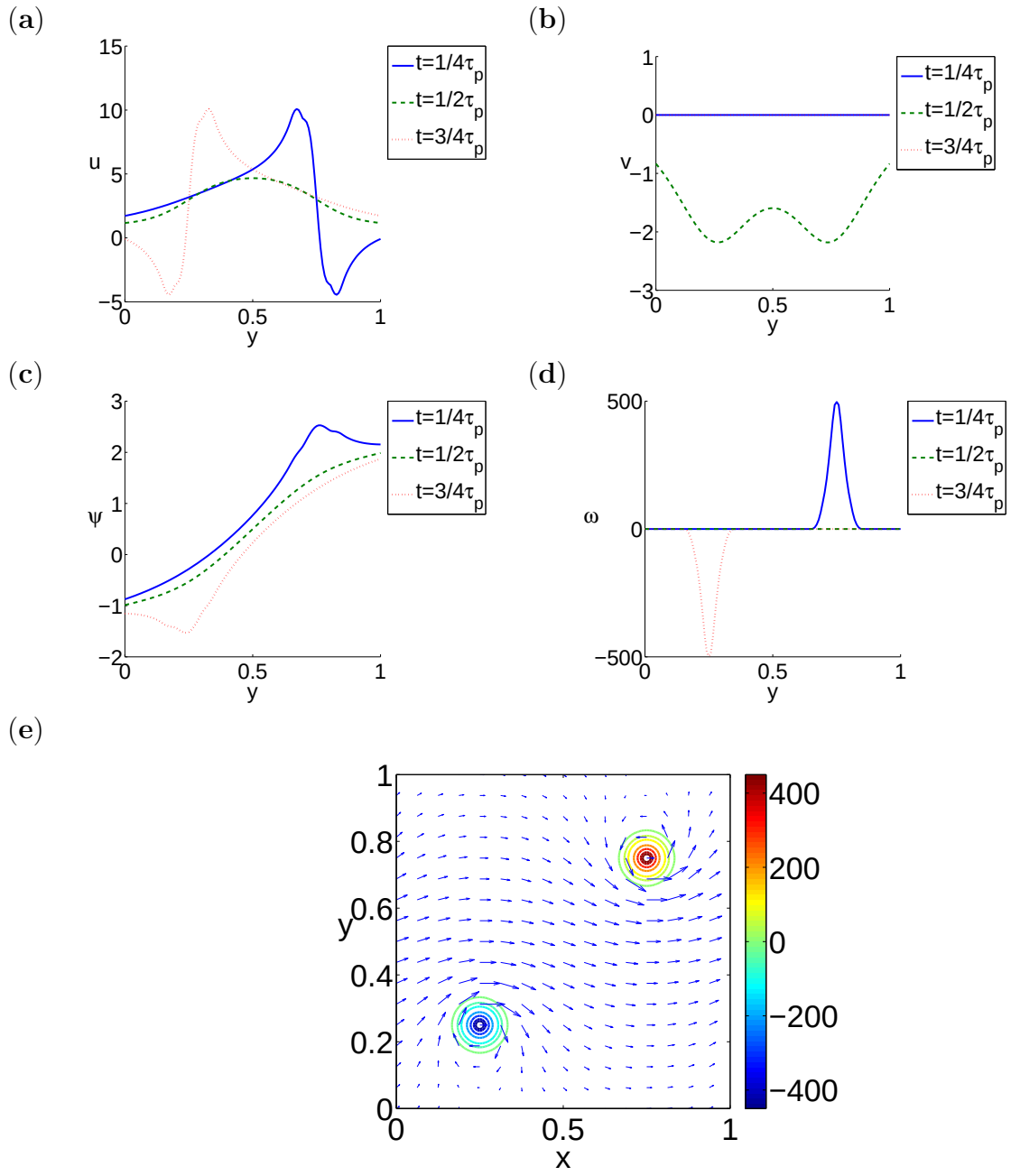

Figure 7: Active vibration corresponding to $\Gamma = 4$ and $U_b = 1$. Other parameters used in the figure are $a = 1$, $b = 0.5$, and $H = 1$. Two vortex blobs are located at $(0.25, 0.25)$ and $(0.75, 0.75)$. (a) Value of u; (b) value of v; (c) value of ψ; (d) value of ω; (e) Velocity field and corresponding vorticity contours in one period.

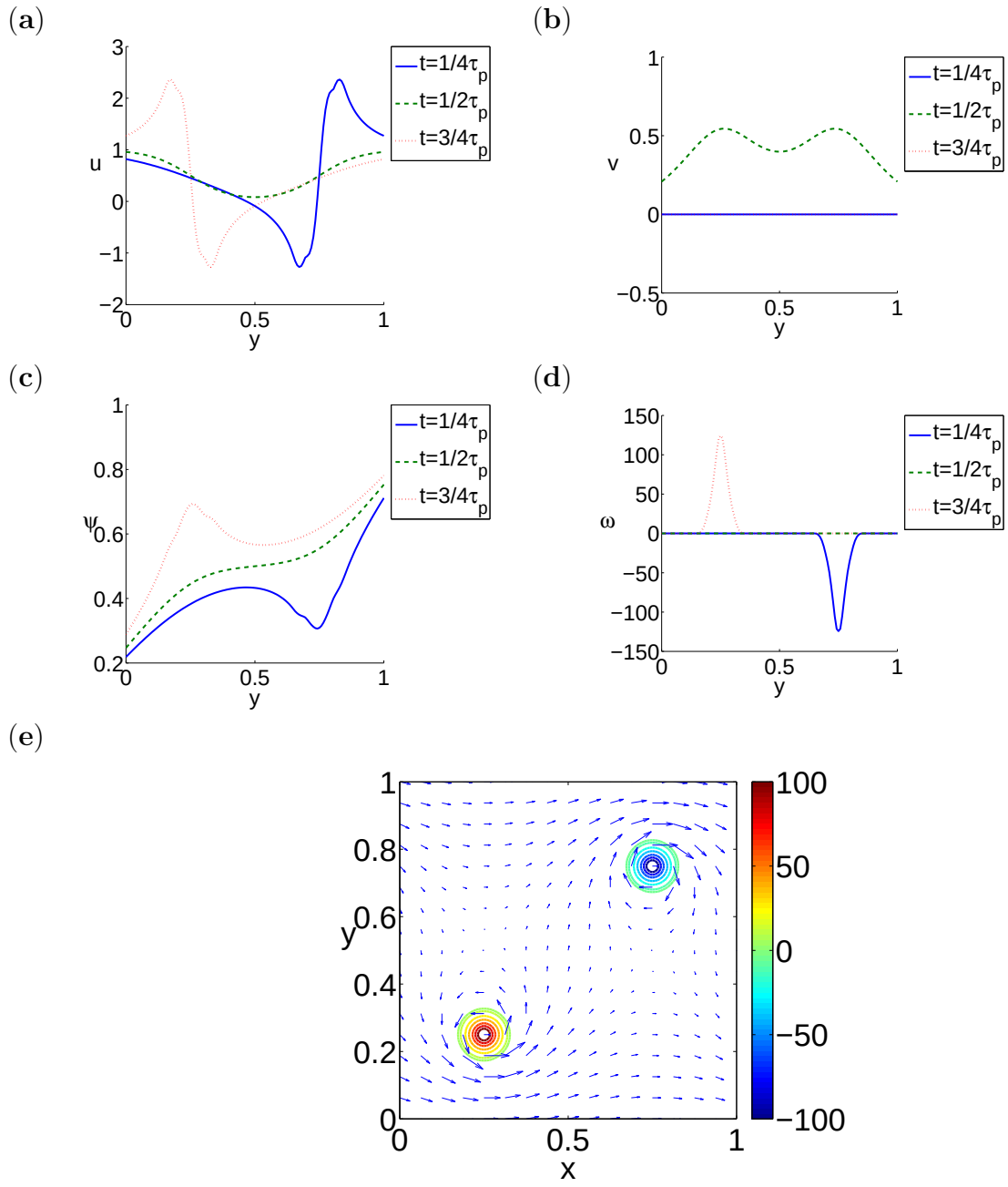

Figure 8: Passive vibration corresponding to $\Gamma = -1$ and $U_b = 1$. Other parameters used in the figure are $a = 1$, $b = 0.5$, and $H = 1$. Two vortex blobs are located at $(0.25, 0.25)$ and $(0.75, 0.75)$. (a) Value of u; (b) value of v; (c) value of ψ; (d) value of ω; (e) Velocity field and corresponding vorticity contours in one period.

(1) and (2) here:

$$\omega = \omega_{in}, \quad \psi = \psi_{in}, \qquad x = 0, 0 < y < H \tag{25}$$

$$\frac{\partial \omega}{\partial t} + \bar{u}\frac{\partial \omega}{\partial x} = 0, \quad \frac{\partial}{\partial t}\left(\frac{\partial \psi}{\partial x}\right) + \bar{u}\left(-\frac{\partial^2 \psi}{\partial y^2} - \omega\right) = 0, \qquad x = L, 0 < y < H \tag{26}$$

$$\omega = \omega_1^B, \quad \psi = \psi_{1,1}, \qquad 0 \le x \le L, y = 0 \tag{27}$$

$$\omega = \omega_M^B, \quad \psi = \psi_{1,M}, \qquad 0 \le x \le L, y = H \tag{28}$$

2.3 Nondimensionalization

We nondimensionalize the equations based on the height of the channel H and the velocity of the incoming vortex blob U. The following dimensionless variables are obtained:

$$x^* = \frac{x}{H}, \quad y^* = \frac{y}{H}, \quad t^* = \frac{tU}{H}$$
$$\mathbf{u}^* = \frac{\mathbf{u}}{U}, \quad \omega^* = \frac{\omega H}{U}, \quad \psi^* = \frac{\psi}{UH},$$

For simplicity, we use the original notation to indicate all the dimensionless variables, then equations (1) - (3) become:

$$\frac{\partial \omega}{\partial t} + \mathbf{u} \cdot \nabla \omega = \frac{1}{Re}\Delta \omega \tag{29}$$

$$-\Delta \psi = \omega \tag{30}$$

$$u = \frac{\partial \psi}{\partial y}, \quad v = -\frac{\partial \psi}{\partial x} \tag{31}$$

with several important dimensionless parameters:

1. $Re = \frac{HU}{\nu}$, the Reynolds number.
2. $\Gamma_r = \frac{\Gamma}{U_b H}$, the ratio of the vortex blob strength and background flow, i.e. relative vortex strength.
3. $S_b = \frac{b}{H}$, the dimensionless vertical space between two arrays of vortices.
4. $S_a = \frac{a}{H}$, the dimensionless period length.

Note that the velocity of the vortex blob is determined by equation (22) and can be rewritten with the above dimensionless parameters as:

$$U = U_b \left(1 + \frac{\Gamma_r}{2S_a} \tanh \frac{\pi S_b}{S_a}\right) \tag{32}$$

In the actual computation, $U = 1$ is fixed after the nondimensionalization, and by varying Γ_r, S_a and S_b and using equation (32), the corresponding values of Γ and U_b are obtained.

2.4 More Discussions on Inflow Boundary Conditions

The vortex blob model is a good approximation of the vortex wake in an infinite domain. However, in a channel, this inflow will lead to singularities at the leading edges of the channel wall as the inflow conditions violate the no-penetration and no-slip wall conditions. As we can see in panels (a) and (b) from figures 7 and 8, the u and v at $y = 0$ and $y = 1$ which correspond to the positions of the two walls are nonzero at most times.

The current model approximates the situation when a vortex generator is placed in front of the channel [3]. On the other hand, many vortex generators can be placed inside the channel, for example, the synthetic jet is attached in the middle of the heat sink to improve the heat transfer efficiency [27, 28]. Therefore, we wish to further explore the inflow conditions and construct vortex streets influenced by channel walls.

2.4.1 Infinite Array of von Kármán Street

We start our discussion by considering the no-penetration condition for the classic point vortex von Kármán street in inviscid flow. If only one point vortex exists near the wall, to obtain a complex potential such that it satisfy $v = 0$ at the wall, we need to place an "image" point vortex with the same strength and opposite sign at its reflection point in the wall. Then according to the method of images, the complex potential of the point vortex pair will satisfy the no-penetration condition.

A schematic figure of the vortex pair is shown in figure 9.

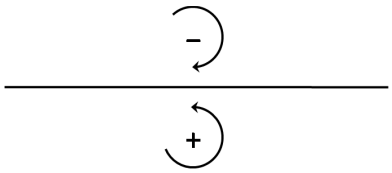

Figure 9: A schematic figure of the method of image for one point vortex.

With the existence of two walls, an infinite array of von Kármán streets is required to satisfy the boundary conditions on both walls. We show the configuration of the vortex street in figure 10. Two walls are located at $y = 0$ and $y = H$, and

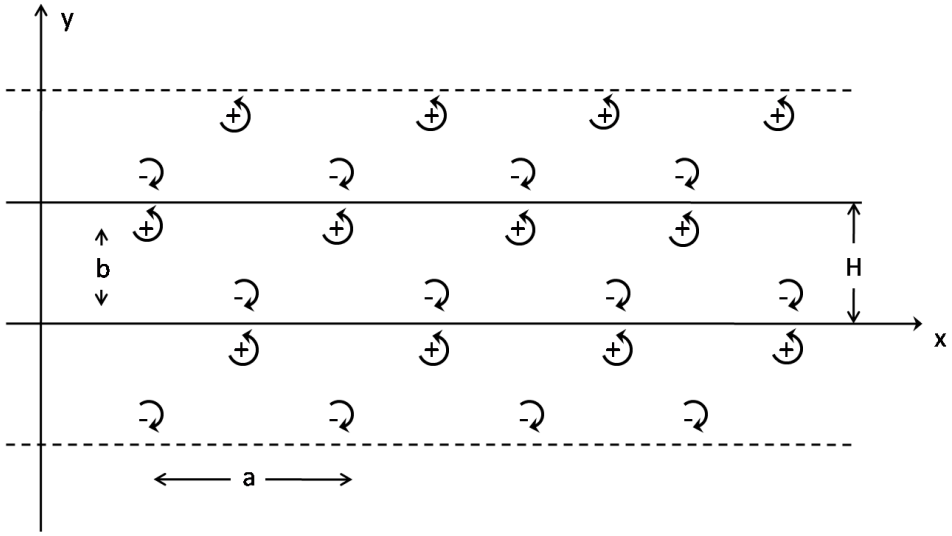

Figure 10: Configuration of an infinite array of von Kármán streets. Two walls are located at $y = 0$ and $y = H$.

a von Kármán street is placed between two walls with the negative point vortices on $z = z_0 + ma$ and positive point vortices on $z = z_0 + (m + \frac{1}{2})a + ib$, where $m = 0, \pm 1, \pm 2, \cdots$. We reflect the whole street through the wall at $y = 0$ and obtain an image of vortex street with opposite sign from $y = -H$ to $y = 0$. Similarly, reflecting the street through the wall at $y = H$ leads to another image of the vortex street from $y = H$ to $y = 2H$. For the two image streets, the negative point vortices are located at $z = z_0 + (m + \frac{1}{2})a + iH$ and $z = z_0 + (m + \frac{1}{2})a - iH$ and the positive

point vortices are located at $z = z_0 + ma + i(b+H)$ and $z = z_0 + ma + i(b-H)$. These vortex streets lead to another two image vortex streets from $y = -2H$ to $y = -H$ and from $y = 2H$ to $y = 3H$, and by continuing this process, we obtain an infinite array of von Kármán streets whose complex potential satisfy the no penetration condition at two walls. The negative vortices are located $z = z_0 + (m + \frac{1}{2})a + i(2n+1)H$ and the positive point vortices are located at $z = z_0 + ma + i(b + (2n+1)H)$, where $n = 0, \pm 1, \pm 2, \cdots$.

We write out the complex potential of the infinite array of vortex streets:

$$\begin{aligned} w &= \lim_{N\to\infty, M\to\infty} \sum_{n=-N}^{N} \sum_{m=-M}^{M} \frac{-i\Gamma}{2\pi} \log \frac{z - z_0 - (m+\frac{1}{2})a - i(b+2nH)}{z - z_0 - ma - i2nH} \\ &\quad + \sum_{n=-N}^{N-1} \sum_{m=-M}^{M} \frac{-i\Gamma}{2\pi} \log \frac{z - z_0 - ma - i(b+(2n+1)H)}{z - z_0 - (m+\frac{1}{2})a - i(2n+1)H} \end{aligned} \tag{33}$$

where N and M are integers ($N, M \in \mathbb{N}$). The first part of the equation corresponds to the original vortex street and its images at $y = 2nH$ to $y = (2n+1)H$, and the second part corresponds to the images at $y = (2n+1)H$ to $y = (2n+2)H$. The inner sum converges to an expression similar to that in equation (16), and we obtain the following complex potential:

$$\begin{aligned} w = &\lim_{N\to\infty} \sum_{n=-N}^{N} \frac{-i\Gamma}{2\pi} \log \frac{\sin\frac{\pi}{a}\left(z - z_0 - \frac{1}{2}a - i(b+2nH)\right)}{\sin\frac{\pi}{a}(z - z_0 - i2nH)} \\ &+ \sum_{n=-N}^{N-1} \frac{-i\Gamma}{2\pi} \log \frac{\sin\frac{\pi}{a}\left(z - z_0 - i(b+(2n+1)H)\right)}{\sin\frac{\pi}{a}(z - z_0 - \frac{1}{2}a - i(2n+1)H)} \end{aligned} \tag{34}$$

Similarly, the complex velocity at a point that does not coincide with a point vortex can be obtained by differentiating equation (34):

$$u - iv = \lim_{N\to\infty} \omega_n \tag{35}$$

where

$$\begin{aligned} \omega_n = &\frac{-i\Gamma}{2a} \sum_{n=-N}^{N} \left(\cot\frac{\pi}{a}\left(z - z_0 - \frac{1}{2}a - i(b+2nH)\right) - \cot\frac{\pi}{a}\left(z - z_0 - i2nH\right)\right) \\ &+ \sum_{n=-N}^{N-1} \left(\cot\frac{\pi}{a}\left(z - z_0 - ib - ix(2n+1)H\right) - \cot\frac{\pi}{a}\left(z - z_0 - \frac{1}{2}a - i(2n+1)H\right)\right) \end{aligned} \tag{36}$$

The point vortex does not induce velocity to itself, and the effect of vortices with the same sign in the arrays will cancel with each other due to the symmetry. Therefore, when calculating the velocity of a point vortex, we only need to include the vortices with the opposite sign. Similar to the equation (17), we obtain the same velocity for all point vortices:

$$u = \lim_{N\to\infty} \sum_{n=-N}^{N} \frac{\Gamma}{2a} \tanh \frac{\pi}{a}(b+2nH) + \sum_{n=-N}^{N-1} \frac{\Gamma}{2a} \coth \frac{\pi}{a}(b+(2n+1)H) \tag{37}$$

The convergence of equation (37) can be easily verified as we rewrite it as:

$$\begin{aligned} u = \frac{\Gamma}{2a} \tanh \frac{\pi b}{a} + \frac{\Gamma}{2a} \sum_{n=1}^{\infty} \Big(\tanh \frac{\pi}{a}(b+2nH) + \tanh \frac{\pi}{a}(b-2nH) \Big) \\ + \Big(\coth \frac{\pi}{a}(b+(2n-1)H) + \coth \frac{\pi}{a}(b-(2n-1)H) \Big) \end{aligned} \tag{38}$$

Then we can prove the convergence of the series in equation (38) by using the integral test and the fact that both hyperbolic tangent and cotangent functions are odd monotonic functions. In figure 11, we plot the velocity u (37) versus N with different H. In general, u converges quickly. In the actual computation, we fix $N = 5$ with

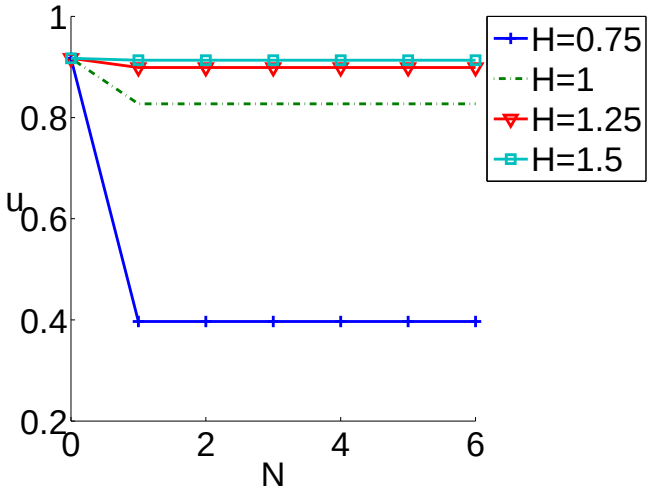

Figure 11: $u = \sum_{n=-N}^{N} \frac{\Gamma}{2a} \tanh \frac{\pi}{a}(b+2nH) + \sum_{n=-N}^{N-1} \frac{\Gamma}{2a} \coth \frac{\pi}{a}(b+(2n+1)H)$ vs. N for $H = 0.75, 1, 1.25$ and 1.5. Other parameters used here is $a = 1$ and $b = 0.5$.

less than 1% error. When $N = 0$, the velocity u corresponds to the regular von

Kármán street velocity with no walls. From figure 11, we notice that the existence of walls will slow down the flow, as u decreases with N. When H is large so the walls are far from the vortex street, the velocity profile is similar to the unconstrained von Kármán street velocity as expected.

2.4.2 Infinite array of vortex blobs

In the viscous flow, we apply the same strategy by replacing the point vortex with vortex blobs with radius δ. Similar to equation (21), the velocity within the blob can be written as:

$$u - iv = u_{vkinf}(z) - \frac{i\Gamma}{2\pi}\frac{1}{z - z_p} + \frac{i\Gamma}{2\pi}\frac{\bar{z} - \bar{z_p}}{\|z - z_p\|^2 + \delta^2} \tag{39}$$

where u_{vkinf} refers to equation (36). In figure 12, we compare the inflow velocities obtained with walls in equation (39) with those obtained in unbounded flow for both active and passive vibrations at time instants $t = 1/4\tau_p$, $t = 1/2\tau_p$ and $t = 3/4\tau_p$. All the solid lines indicate the values for unbounded cases and all the dashed lines show the values with walls. The parameters used in the figures are the same as in figure 7 and 8.

2.4.3 Poiseuille Background Flow

By applying the model of an infinite array of von Kármán streets, the no penetration conditions are satisfied at the leading edges of the walls. However, the no slip conditions are still violated as $u \neq 0$ at the entrance, and it results in a singularity at the leading edge of the wall.

One possible solution is to apply the model of infinite array von Kármán street with a Poiseuille flow as the background flow instead of a uniform flow. The Poiseuille flow describes the pressure-induced flow in a long channel. Supposing the channel is placed between $y = 0$ and $y = 1$, the flow is uni-directional along the x-direction as:

$$u(y) = cy(1 - y), \tag{40}$$

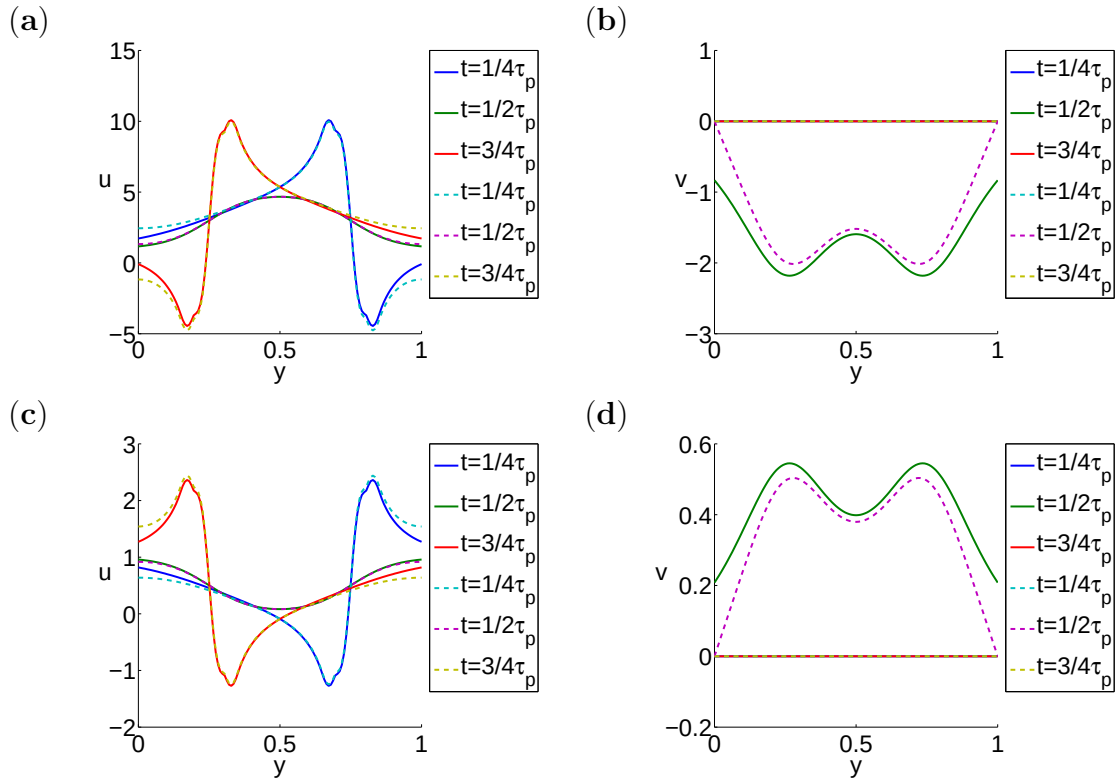

Figure 12: Value of velocities in unbounded and bounded situations at time instants $t = 1/4\tau_p$, $t = 1/2\tau_p$ and $t = 3/4\tau_p$. The solid lines indicate the value for unbounded cases and the dashed lines show the values with walls. Parameters include $a = 1$, $b = 0.5$ and $H = 1$ for all four panels. (a), (b) value of u and v in active vibration with $\Gamma = 4$ and $U_b = 1$; (c), (d) value of u and v in passive vibration with $\Gamma = -1$ and $U_b = 1$.

The constant c depends on the pressure drop Δp, the dynamic viscosity μ and the length of the duct L [65] as

$$c = \Delta p / 4\mu L. \tag{41}$$

Unlike the uniform flow, the Poiseuille flow satisfies the no-slip and no-penetration conditions at the wall. Therefore, when the vortex blob induced wall velocity is small compared to the speed of the vortex blob, the wall velocity will approximately satisfy the no-slip condition after the nondimensionalization.

In most cases, the value of the wall velocity is equal to or less than the magnitude of 10^{-1}, and this model may be a good approximation to the no-slip condition. However, when the ratio of S_b/S_a and $|\Gamma_r|$ are both large, for example, when $\Gamma_r = -0.75$, $S_b = 0.75$ and $S_a = 0.5$, the velocity at $t = 1/4\tau_p$ is around 4.3, the wall velocity can be far away from zero. The advantage of this model is that the set up of the model is based on physical situations and approximates the typical realistic flows.

2.5 The Numerical Methods

We design our numerical scheme to solve the Navier-Stokes equations (1) and (2) accurately and efficiently in the regime of laminar flow. We discretize the equations with an implicit Crank-Nicolson scheme as most explicit schemes for Navier-Stokes equations only allow small time steps for stability [54, 55]. One particularly important aspect of the system of equations is that the advection term in the vorticity equation is nonlinear, as involving ω and partial derivatives of ψ. To deal with this issue, either a nonlinear solver or a linearization to the advection term is required. A Newton-type of method can be used to solve the resulting nonlinear system [47]. However, this approach is mainly used for steady problems as the expense of constructing and solving the Jacobian matrix is very large. In this problem, we instead linearize the advection term and solve the resulting linear system.

We solve the problem on a regular uniform rectangular mesh with $N \times M$ gird

points. The mesh sizes in the x and y directions are $dx = 1/(N-1)$ and $dy = 1/(M-1)$. The equations are solved with a time-stepping Crank-Nicolson scheme. All spatial derivatives are discretized with a second-order central difference scheme except near boundaries where one sided second-order schemes are applied and at the channel walls where a fourth-order Briley's formula is used. Denoting the current time step as $n+1$, the time discretization is:

$$\frac{\omega^{n+1}-\omega^n}{dt} + \frac{1}{2}\mathbf{u}^{n+1/2}\cdot(\nabla\omega^{n+1}+\nabla\omega^n) = \frac{1}{2}\frac{1}{Re}(\Delta\omega^{n+1}+\Delta\omega^n) \quad (42)$$

$$-\Delta\psi^{n+1} = \omega^{n+1} \quad (43)$$

The velocity $\mathbf{u}^{n+1}$ is then obtained from ψ^{n+1} by using a second-order central difference.

The nonlinear term is linearized by a second-order extrapolation from previous steps:

$$\mathbf{u}^{n+1/2} = \frac{3}{2}\mathbf{u}^n - \frac{1}{2}\mathbf{u}^{n-1} \quad (44)$$

Since two previous time level solutions are required for the extrapolation, we have to change the scheme at the first step. There we first use $\mathbf{u}^{1/2} = \mathbf{u}^0$ to compute the value of ω, ψ and $\mathbf{u}$ at step 1, and then we correct the results by taking $\mathbf{u}^{1/2} = \frac{1}{2}(\mathbf{u}^0 + \mathbf{u}^1)$, which is also a second-order extrapolation, and solve the equations again to obtain $\{\omega^1, \psi^1, \mathbf{u}^1\}$.

This linearization may be expected to cause an instability for large time steps. One possible solution is to iterate on the nonlinear term. At each iteration step k, we can reconstruct the $(n+1/2)$ velocity with the newly computed $n+1$ step solution at step $k-1$ as $\mathbf{u}_k^{n+1/2} = \frac{1}{2}(\mathbf{u}^n + \mathbf{u}_{k-1}^{n+1})$ to solve for $\mathbf{u}_k^{n+1}$. This procedure requires more computation cost but may be necessary when dt is large or the flow changes rapidly. However, we findx that for most parameters in the region of interest, a time step of $dt = 1/128$ is good enough for a stable result and only a few iterations are required. We show in figure 13 that the difference between each iteration becomes smaller than

the numerical error in the discretization $O(dt^2)$ after few steps.

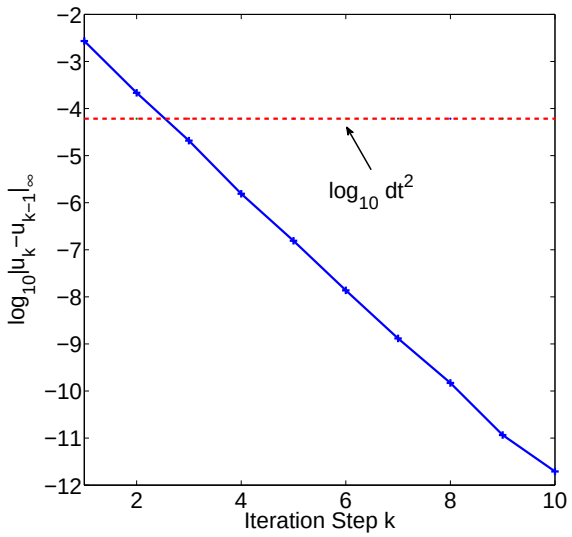

Figure 13: $\log_{10} \|u_k - u_{k-1}\|_\infty$ vs. the interation step k. Other parameters are $Re = 1000$, $S_a = 1$, $S_b = 0.5$ and $\Gamma_r = 4$.

With the linearization on the advection term, we realize that equation (42) and (43) are only coupled through Briley's formula and if we arrange the boundary conditions carefully, we can write the linear system as follows:

$$\left(\begin{array}{cccc|cccc}
B & & & & I & & & \\
\hline
 & 0 & & & & I(\omega_{in}) & & \\
\hline
 & & -\Delta & & & & I & \\
\hline
 & & & adv. & & & & cI \\
\hline
 & & & B & & & & I \\
\hline
I(\psi_w) & & & & 0 & & & \\
\hline
 & I(\psi_{in}) & & & & 0 & & \\
\hline
 & & 0 & & & & L & \\
\hline
 & & & 0 & & & & adv. \\
\hline
 & & & I(\psi_w) & & & & 0
\end{array}\right)
\left(\begin{array}{c}
\\
\\
\psi \\
\hline
\\
\\
\omega \\
\\
\end{array}\right)$$

Where B stands for the Briley's formula, $L = -\Delta + \mathbf{u} \cdot \nabla$ is the elliptic operator and $c = -dt\,\bar{u}$. The linear system can be written in the block matrix form as:

$$\begin{pmatrix} A_{11} & A_{12} \\ A_{21} & A_{22} \end{pmatrix} \begin{pmatrix} \psi \\ \omega \end{pmatrix} = \begin{pmatrix} b_1 \\ b_2 \end{pmatrix} \tag{45}$$

Therefore, we can solve the block matrix as

$$\begin{pmatrix} A_{11} & A_{12} \\ A_{21} - A_{22}A_{12}^{-1}A_{11} & 0 \end{pmatrix} \begin{pmatrix} \psi \\ \omega \end{pmatrix} = \begin{pmatrix} b_1 \\ b_2 - A_{22}A_{12}^{-1}b_1 \end{pmatrix} \tag{46}$$

and the problem becomes solving the linear system

$$(A_{21} - A_{22}A_{12}^{-1}A_{11})\psi = b_2 - A_{22}A_{12}^{-1}b_1 \tag{47}$$

This matrix can be formed explicitly as all the four blocks are sparse matrices and the right-upper block A_{12} is actually a diagonal matrix given $\bar{u} \neq 0$. In fact, A_{21} only has $2N+M+1$ nonzeros on the diagonal, and both A_{11} and A_{22} are close to pentadiagonal matrices except at boundary points. The computational cost to explicitly form the matrix in equation (47) is $O(NM)$. We show the sparsity pattern of the matrix in figure 14 which is a pentadiagonal block matrix.

The linear matrix can be solved by iterative methods like GMRES with a preconditioner [56]. However, we find a direct solver is reasonably fast and scalable as well. For a spatial grid size of 513×129 and $dt = 1/128$, it takes about 150 seconds to run the simulation for one period. And we notice that the computational cost is approximately $O((NM)^{1.3})$.

Once ψ is obtained, we obtain ω by the following equation:

$$\omega = A_{12}^{-1}b_1 - A_{12}^{-1}A_{11}\psi \tag{48}$$

Again, since A_{12} is a diagonal matrix, only matrix-vector multiplication is required to obtain ω from ψ.

The verification of the numerical method is described in the Appendix.

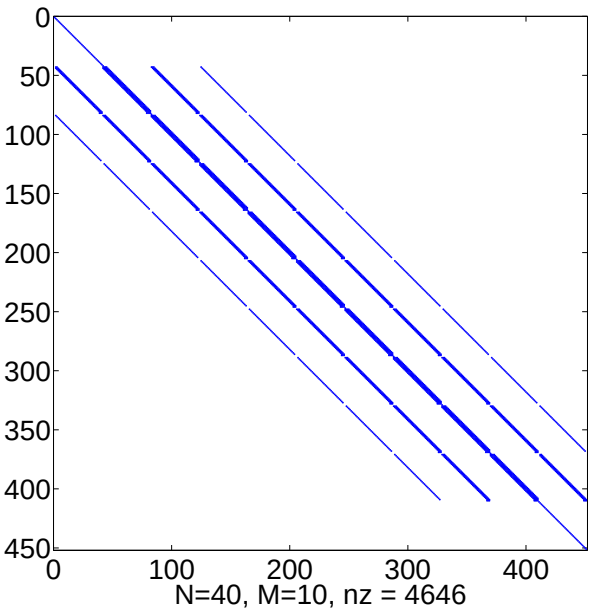

Figure 14: The sparsity pattern of the mattrix $A_{21} - A_{22}A_{12}^{-1}A_{11}$, $N = 40$, $M = 10$, and the nonzeros is approximately $10NM$.

CHAPTER III

CHANNEL FLOW RESULTS AND DISCUSSIONS

In this chapter, we discuss the results of the channel flow based on two types of incoming flows: active and passive vibration cases as describe in chapter 2. Unlike flows in an unbounded region, the flow behaves dramatically different for those two type of incoming flows due to the existence of walls. We are particularly interested in the property of the vorticity as it plays a significant role in the heat transfer performance.

3.1 Flows in the Active Vibration Case

In the active vibration case, a periodic inflow consisting of two arrays of vortex blobs enters the channel with positive vortices in the upper half and negative vortices in the lower half. As a result, the flow in the channel eventually becomes time periodic as well.

We show the contour plot of the vorticity, the stream function and the speed $\|\mathbf{u}\| = \sqrt{u^2 + v^2}$ over the whole channel at one time instant (beginning of a period) in figure 15.

In figure 15, we notice that the vortex blobs mainly move in the downstream direction and the structure of the reversed von Kármán vortex street is therefore maintained in the channel. The blobs diffuse due to the viscosity in the channel, and their shape become half of a dipole due to the wall's presence. An upstream flow is induced between the blob and the wall which decreases the horizontal velocity of the flow in that region. This deceleration therefore generate opposite signed vorticity at the boundary layer right below the corresponding vortex blobs. Therefore, we observe that the boundary layer over the entire channel is composed of alternating positive

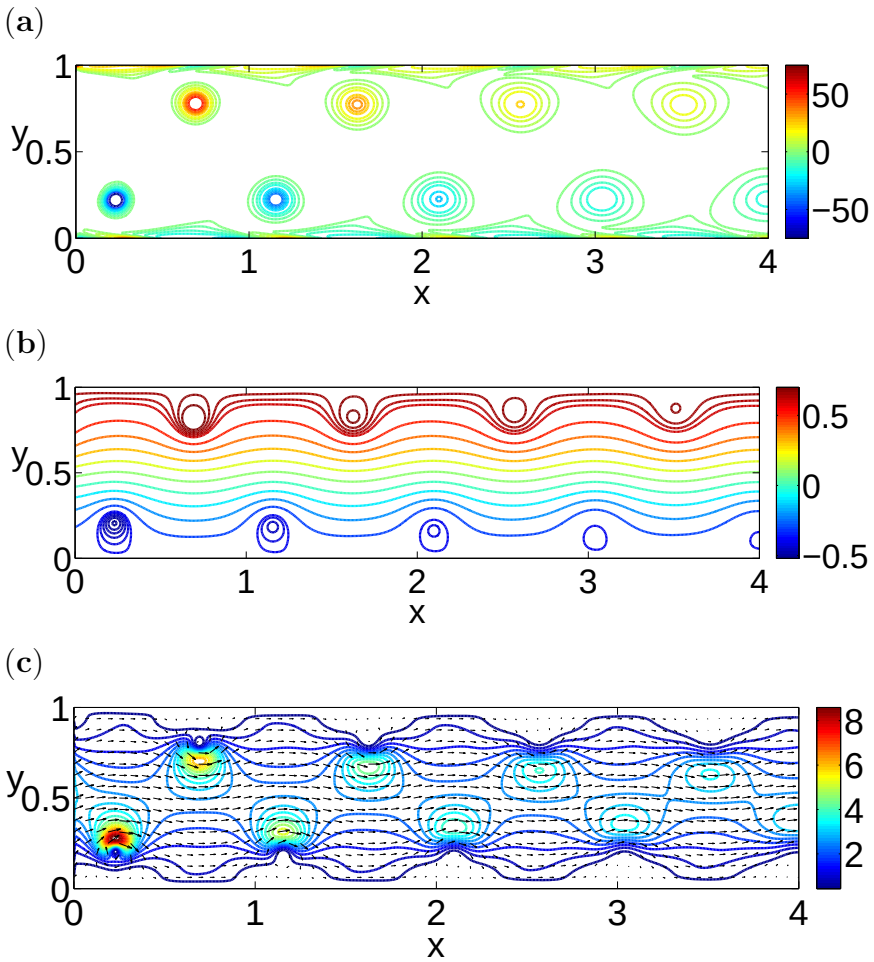

Figure 15: Contour plot obtained with $Re = 1000$, $\Gamma_r = 6$, $S_a = 1$ and $S_b = 0.5$, (a) vorticity; (b) steam function. (c) Contour plot of speed $\|\mathbf{u}\|$ and the quiver plot.

and negative vorticity in figure 15.

We recover the pressure from the velocity through equations:

$$\nabla p = -\frac{\partial \mathbf{u}}{\partial t} - \mathbf{u} \cdot \nabla \mathbf{u} + \frac{1}{Re} \Delta \mathbf{u} \tag{49}$$

with the dimensionless density ρ set to be 1. By setting the pressure value at the lower left corner of the channel, we can then obtain pressure value of the whole channel by integration over the above equation. The time instant pressure contour is shown in figure 16 (a). In panel b of the figure, we define Δp as the averaged pressure difference between the exit and the entrance of the channel. The solid line indicate time instant values and the dashed line is for the time-averaged value. If there is no

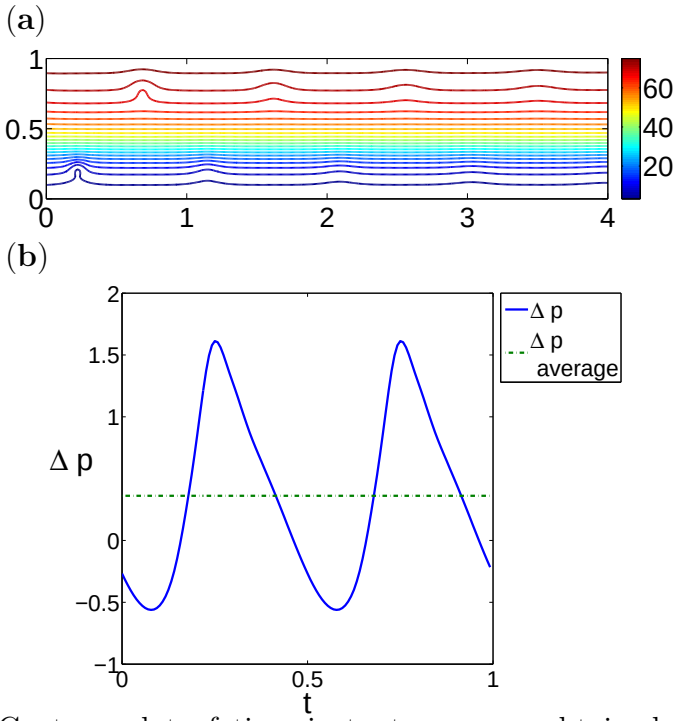

Figure 16: (a) Contour plot of time instant pressure obtained with $Re = 1000$, $\Gamma_r = 6$, $S_a = 1$ and $S_b = 0.5$; (b) pressure difference Δp vs. t. The solid line indicate time instant values and the dashed line is for the time-averaged value.

vortex blob, the time-periodic solution is close to a Poiseuille flow and the pressure in the downstream direction is smaller. However, in the active vibration cases, we notice the pressure in the downstream direction increases as Δp is positive for most of the period. This phenomena is also observed by Gerty in the experiments with

piezoelectronic reed as the vibrating plate [29].

The is due to the deceleration by vortex blobs at the boundary layer. When the blobs are strong enough, in the deceleration region right below the vortex blobs, the boundary layer is in the upstream direction. Therefore, the shear stress $\mu\frac{\partial u}{\partial y}$ is also in the upstream direction which leads to a positive work of the wall to the fluids, and the pressure thus increases.

We also evaluate the time averaged vorticity over one period as

$$\overline{\omega} = \frac{1}{\tau_p}\int_0^{\tau_p} \omega dt$$

and show the contour plot in figure 17.

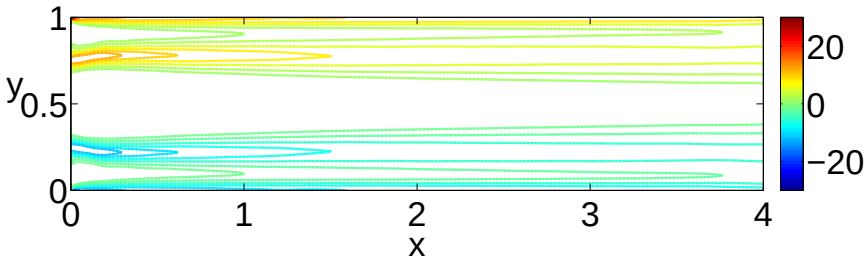

Figure 17: Contour plot of time averaged vorticity $\overline{\omega}$ obtained with $Re = 1000$, $\Gamma_r = 6$, $S_a = 1$ and $S_b = 0.5$.

The time averaged flow behaves as two vortex layers with opposite signs enter the channel. Eventually the channel flow is composed of four vortex layers: two boundary layers and two incoming vortex layers. We show the vertical slices of $\overline{\omega}$ at several positions in figure 18 (a). The two peaks at $x = 0$ indicate the center of the incoming vortex layers. We take $S_b = 0.5$, therefore the positive one comes into the channel at $y = 0.75$ and the negative one is at $y = 0.25$. We plot the y position of the peak for the positive vortex layer in figure 18 (b), and we can see it moves towards the wall at beginning, and then goes back and eventually shifts towards the wall again.

We show the cross section values of time-averaged horizontal and vertical velocity

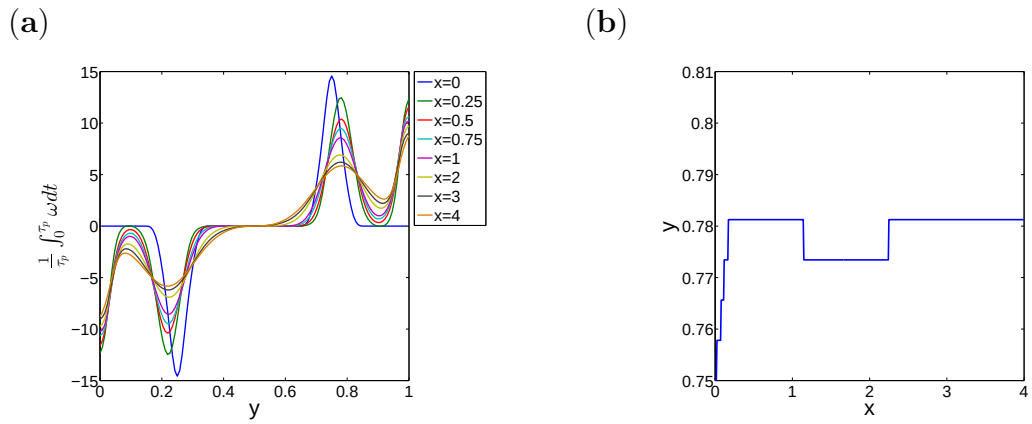

Figure 18: Parameters used here are $Re = 1000$, $\Gamma_r = 6$, $S_a = 1$ and $S_b = 0.5$. (a) Cross section value of $\overline{\omega}$ at $x = 0, 0.25, 0.5, 0.75, 1, 2, 3, 4$. (b) Position of the positive vortex layer across the channel.

in figure 19. We notice that the horizontal velocity is simply smoothed out in the

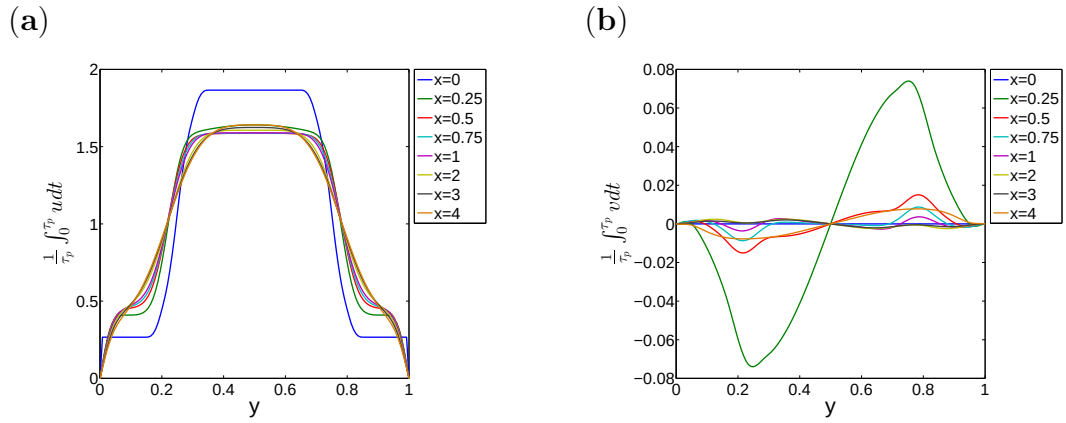

Figure 19: Cross section value of time-average horizontal and vertical velocity at $x = 0, 0.25, 0.5, 0.75, 1, 2, 3, 4$. Other parameters used here are $Re = 1000$, $\Gamma_r = 6$, $S_a = 1$ and $S_b = 0.5$. (a) $\frac{1}{\tau_p}\int_0^{\tau_p} u dt$ vs. y; (b) $\frac{1}{\tau_p}\int_0^{\tau_p} v dt$ vs. y.

channel. But the vertical velocity jumps from zero at the entrance to a nonzero value at $x = 0.25$, then the value becomes smaller until $x = 3$ and finally becomes large again at $x = 4$.

When the vortex sheet develops in the channel, it will be driven towards the wall by the boundary layer and be diffused by the viscous effect at the same time. Near the entrance of the channel, a very strong boundary layer will be generated and the vortex sheet is attracted to the wall. As the boundary layer becomes weaker in the

channel, the position of the vortex sheet shifts towards the centerline again. Later, the diffusion effect dominates and the flow tends toward a Poiseuille flow where the vorticity becomes linear across the channel.

These properties hold not only for this particular parameter set. In fact for all the active vibration cases, we observe the same phenomena no matter which values we choose for Re, Γ_r, S_a and S_b. The structure of the reversed von Kármán vortex street is always maintained in the channel and the flow eventually becomes periodic in time. In figure 20 to figure 24, we show the time instantaneous vorticity contours of the flows for various dimensionless numbers, and we take all the contour curves at the same value for comparison.

In figure 20, we vary the Reynolds number from 100 to 2000 and keep the other parameters unchanged. The diffusion effect becomes weaker as the Reynolds number increases, and a stronger boundary layer is generated near the wall and thus the boundary layer becomes thinner.

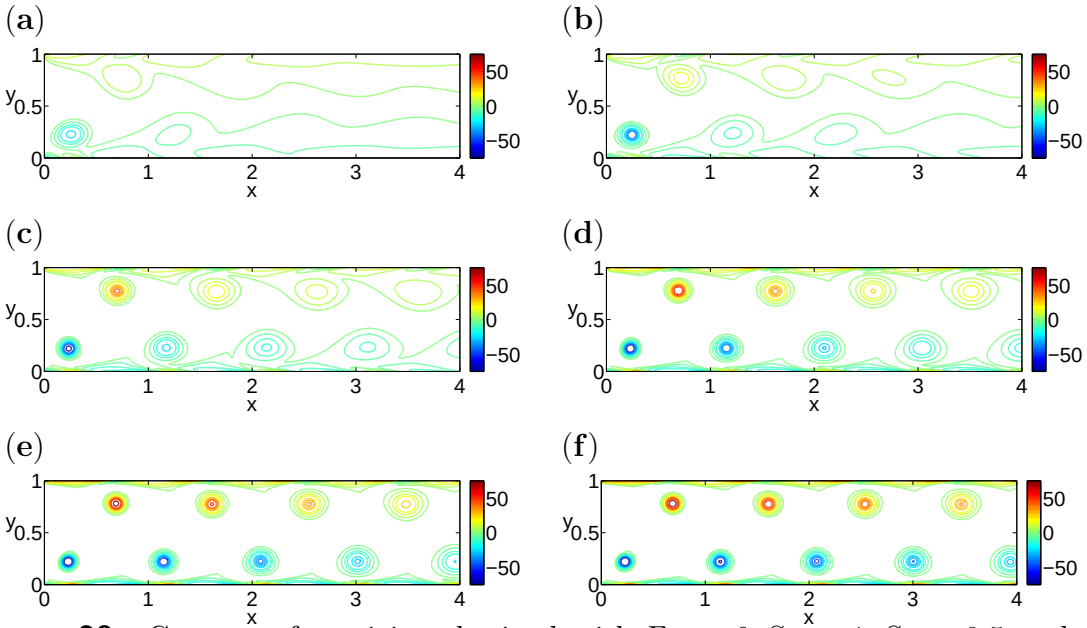

Figure 20: Contour of vorticity obtained with $\Gamma_r = 6, S_a = 1, S_b = 0.5$ and (a) Re=100; (b) Re=200; (c) Re=500; (d) Re=1000; (e) Re=1500; (f) Re=2000.

In figure 21, we change the relative vortex strength Γ_r and fix the other parameters. As Γ_r increases, the vortex blobs becomes stronger in the channel. The corresponding

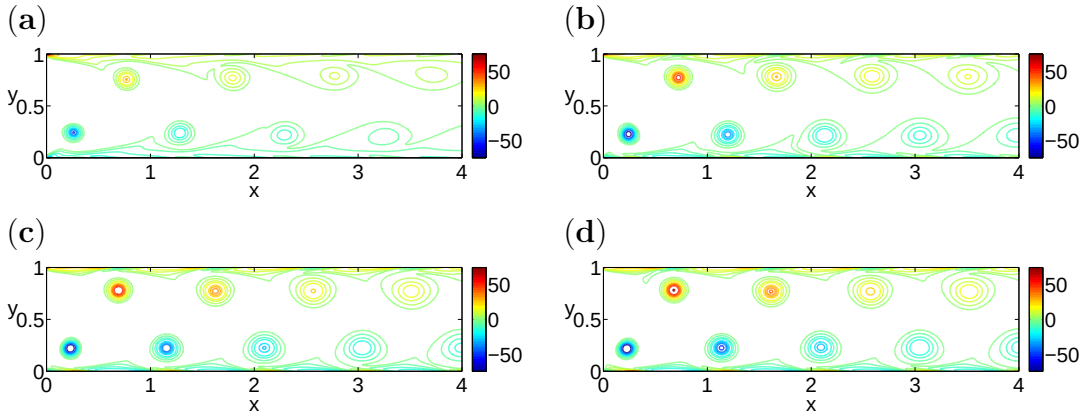

Figure 21: Contour of vorticity obtained with $Re = 1000, S_a = 1, S_b = 0.5$ and (a) $\Gamma_r = 1$; (b) $\Gamma_r = 3$; (c) $\Gamma_r = 6$; (d) $\Gamma_r = 9$.

opposite vorticity generated between the blobs and the walls becomes stronger as well.

For active vibration cases, the blob induced velocity moves in the downstream direction, therefore, we can consider the limited case as $\Gamma_r \to \infty$ which can be achieved by setting the background flow speed U_b to be zero. We show the contour plot of time instantaneous vorticity in figure 22. It is clear that even with the limited case, the flow behaves in the same pattern as the other active vibration cases where the reversed von Kármán street structure is maintained in the channel. A very strong opposite signed vorticity is generated in the boundary layer and we can observe two separations from the wall for the first positive blob and the second negative blob. Given that, the separated vorticity is still much weaker compared to the strength of the vortex blob and it is smoothed out quickly in the channel.

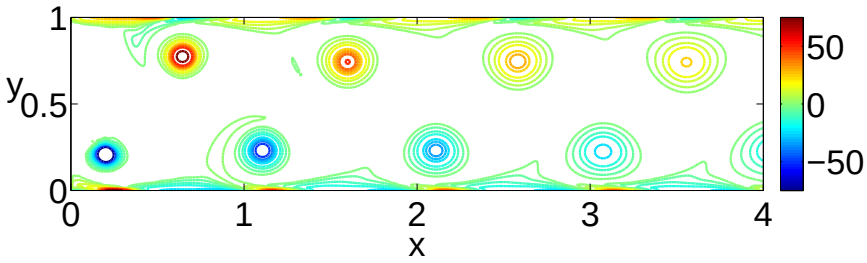

Figure 22: Contour plot of vorticity, $Re = 1000$, $S_a = 1$, $S_b = 0.5$ and $\Gamma_r = +\infty$

In figure 23, we change the value of S_b while keeping the other parameters fixed.

S_b defines the vertical space between two incoming blobs, and therefore cannot exceed

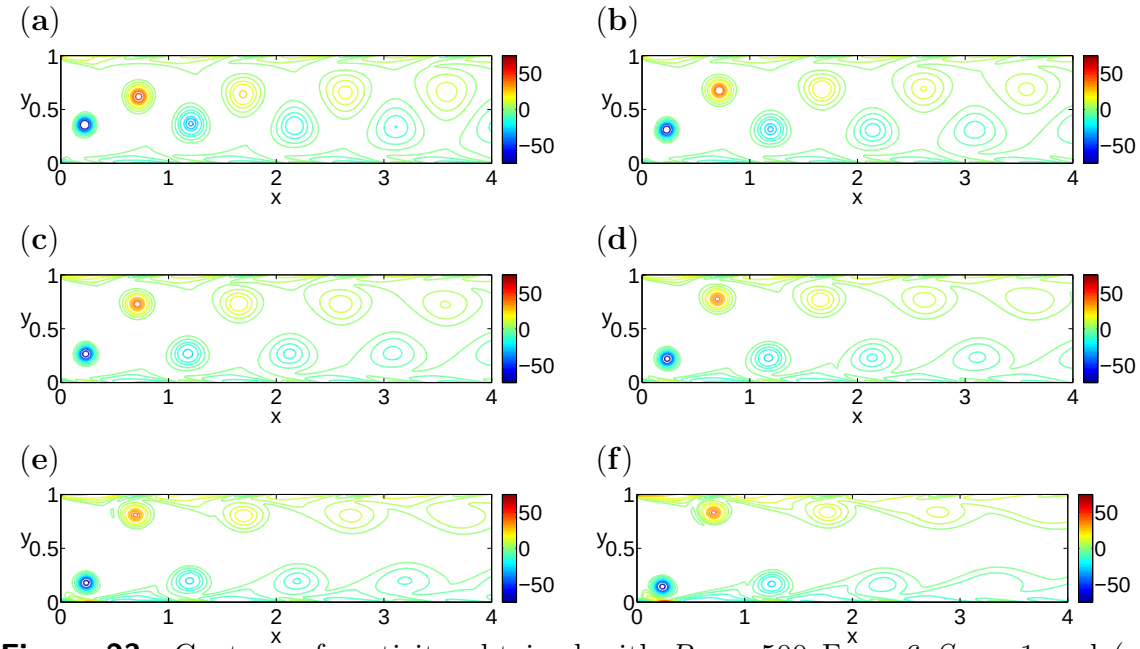

Figure 23: Contour of vorticity obtained with $Re = 500, \Gamma_r = 6, S_a = 1$ and (a) $S_b = 0.2$; (b) $S_b = 0.3$; (c) $S_b = 0.4$; (d) $S_b = 0.5$; (e) $S_b = 0.6$; (f) $S_b = 0.7$

1. In the actual computation, the vortex blob has a finite radius of 0.05 and to avoid the contact of the blob with the wall, we only take S_b no larger than 0.7.

As S_b increases, the vortex blobs are closer to the wall boundary and stronger interactions with the boundary layer are expected. On the other hand, with fixed Γ_r and S_a, both the background flow speed U_b which is given by equation (32) and the vortex blob strength $\Gamma = U_b H \Gamma_r$ will decrease. Therefore, as the vortex blobs get closer to the wall, a stronger boundary layer will be generate, but the blobs themselves are weaker and diffuse more quickly in the channel as shown in figure 23.

In figure 24, we change the value of S_a and fix the other parameters. S_a defines the horizontal space between two blobs and determines the length of the period. In the dimensionless form, its value is the same as the time period. As S_a increases, both U_b and Γ increase as well. Therefore, we expect a stronger boundary layer in the channel and the blobs diffuse more slowly as shown in figure 24.

When S_a tends to zero, the incoming flow is composed of two vortex layers and

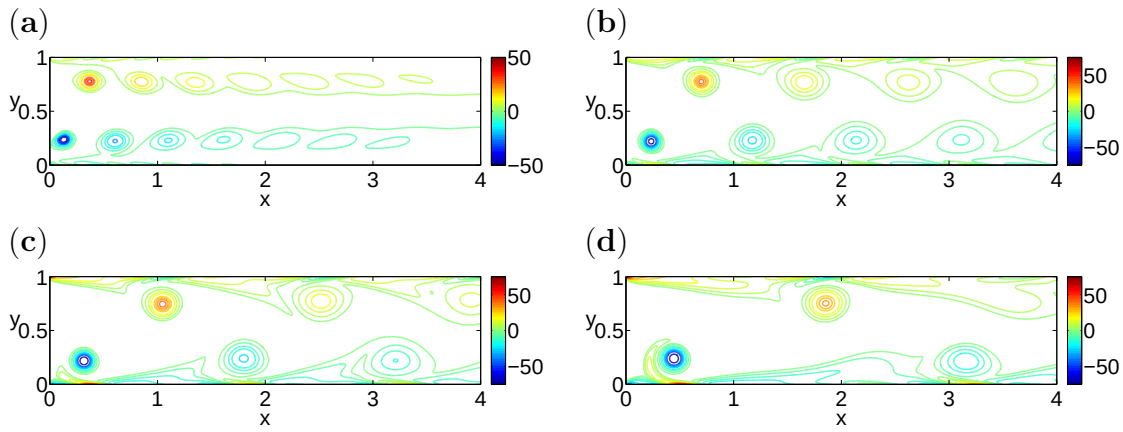

Figure 24: Contour of vorticity obtained with $Re = 500, \Gamma_r = 6, S_b = 0.5$ and (a) $S_a = 0.5$; (b) $S_a = 1.0$; (c) $S_a = 1.5$; (d) $S_a = 2.5$.

the flow is similar to the time averaged solution shown in figure 17 and 18. When S_a tends to infinity, only a single vortex blob is in the channel. A more detailed discussion of this situation is presented in the next section.

3.2 Flows in the Passive Vibration Cases

In the passive vibration cases, the negative vortex blobs enter the channel at the upper half of the channel while the positive ones go into the lower half. The inflow has a structure similar to the flow past an obstacle like a cylinder or a square where a von Kármán vortex street is formed in the wake. In contrast to the active vibration cases, in the passive vibration cases the vortex blobs do not maintain the vortex street structure as they enter the channel.

Figure 25 shows the contours of the vorticity, the stream function and the speed of the velocity at one time instant for a certain set of parameters. We observe vortex moving away from the wall in figure 25 (a). Vortex blobs induce a flow in the downstream direction in the boundary layer regions and accelerate the flow between the blob and the wall. Therefore the external flow reinforces the boundary layer. A strong vortex with opposite sign is created and separates from the wall. The interaction between the incoming vortex blob and the counter-rotating vortex of the

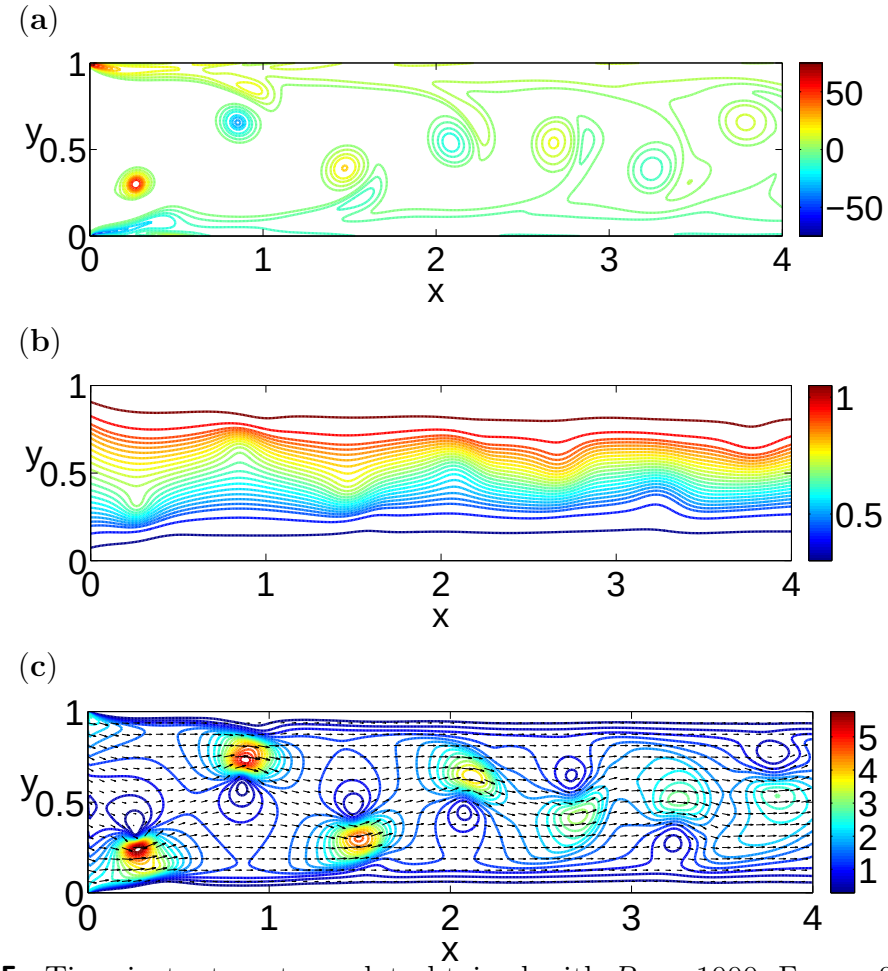

Figure 25: Time instant contour plot obtained with $Re = 1000$, $\Gamma_r = -0.6$, $S_a = 1$ and $S_b = 0.5$ for (a) vorticity; (b) stream function; (c) speed.

adjacent wall boundary layer then pushes the negative vortex blob downwards and the positive vortex blob upwards. They cross the center line and exchange their positions at some distance downstream. After that, the positive blobs stay in the upper half and the negative ones stay in the lower half and form a street with a structure similar to that of the active vibration case.

These observations of the "crisscross motions of vortices" are in agreement with earlier works by Suzuki *et al.* [66], Camarri *et al.* [16], Singha *et al.* [64], etc. . Suzuki *et al.* [66, 67] reported the unsteady flow structure in the wake of a square rod in a channel. They found that at blockage ratio 0.3 the main cause of the inversion of the vortices was the coupling of the wake vorticity and the separation of the boundary layer from the wall. Camarri *et al.* [16] studied the vorticity structure of a confined cylinder and indicated that at small blockage ratio (0.1) the incoming-flow vorticity played the dominant role.

We plot the time-averaged vorticity $\overline{\omega}$ in figure 26. In this figure, we find that

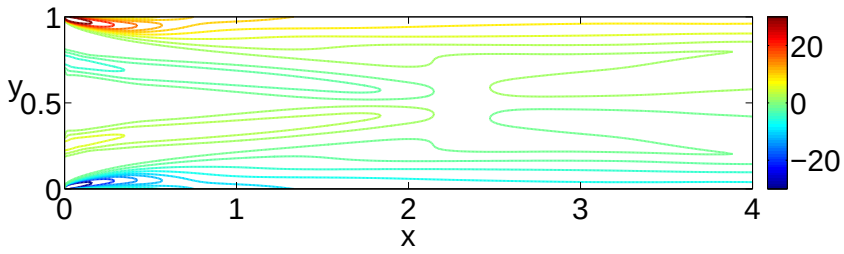

Figure 26: Contour plot of time averaged vorticity obtained with $Re = 1000$, $\Gamma_r = -0.6$, $S_a = 1$ and $S_b = 0.5$.

the positive and negative vortex layers come across each other in the middle of the channel, and then change their positions.

We again recover the pressure from the velocity The time instant pressure contour is shown in figure 27 (a). In panel b of the figure, we plot the value of Δp. The solid line indicate time instant values and the dashed line is for the time-averaged value.

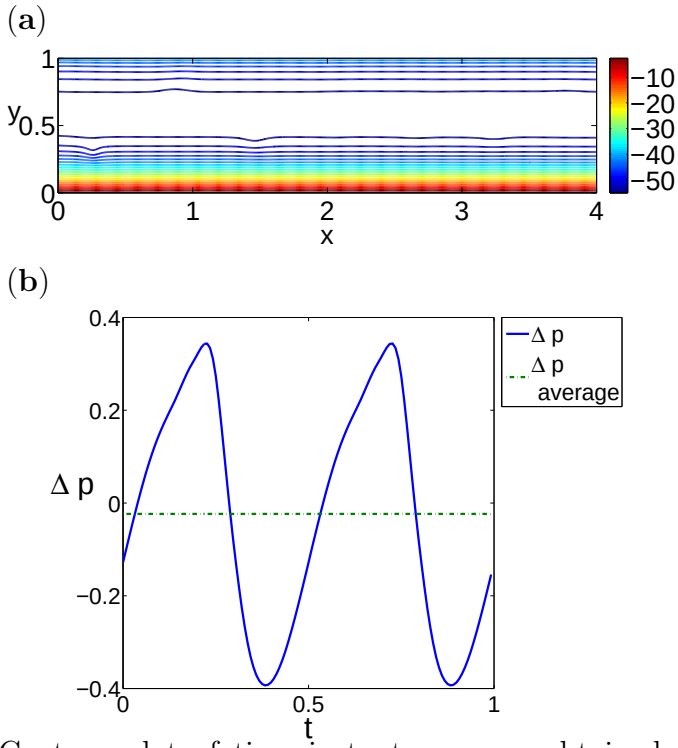

Figure 27: (a) Contour plot of time instant pressure obtained with $Re = 1000$, $\Gamma_r = -0.6$, $S_a = 1$ and $S_b = 0.5$; (b) pressure difference Δp vs. t. The solid line indicate time instant values and the dashed line is for the time-averaged value.

Similarly to the active vibration cases, Δp varies up and down at the same pace as the blobs leaving the channel with a time-averaged value of around -0.1. The time instant contour is taken at the beginning of the period corresponding to figure 25 (a). A positive blob just enters the channel from the lower half and creates a higher pressure along the lower wall.

The crisscross motion happens mainly due to the interaction between the incoming vortex blobs and the wall separated vortices. To illustrate this, we impose a symmetry condition for u instead of the no-slip condition on the wall as $\dfrac{\partial u}{\partial y} = 0$. This condition plus the no-penetration condition lead to $\omega = \nabla \times \mathbf{u} = -u_y + v_x = 0$. As a consequence, no vorticity will be generated and separated from the wall as ω is forced to be zero at the wall boundary. Figure 28 shows the vorticity contours of the flows with the symmetry conditions obtained with same parameters as in figure 25. By eliminating the wall separation, it is clear that the inversion of vortices will not

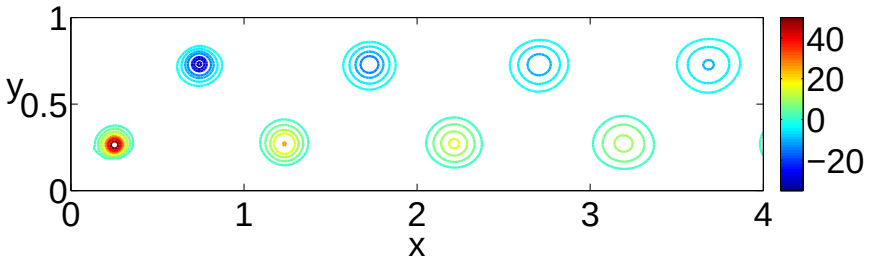

Figure 28: Countour plot of vorticity with symmetry wall boundary conditions and $Re = 1000$, $\Gamma_r = -0.6$, $S_a = 1$ and $S_b = 0.5$.

happen and the structure of the incoming vortex street is maintained as in the active vibration cases.

We also consider the effect of different parameters Re, Γ_r, S_b and S_a on the fluid structures. In figures 29 to 37, we show the instantaneous vorticity contours for various parameter sets, and we take all the contour curves at the same values for comparison. Unlike the active vibration where the street structures are similar to each other under different parameters, we find that in the passive vibration cases, physical parameters play a significant role in determining the flow structures and properties.

In figure 29, we vary the Reynolds number from 100 to 2000 and keep the other parameters unchanged. In this regime, the flows behave similarly. When the Reynolds number is small ($\sim$ 100), the vortex blobs are smeared out before they cross the centerline. As the Reynolds number increases, the diffusion effect becomes weaker. Thus stronger vortices separate from the wall and stay in the channel for longer distance.

We define the exchange distance X_e as the horizontal position where the positive and negative blobs first invert their vertical positions in the channel. We plot X_e versus Reynolds number in figure 30.

When Reynolds number becomes larger, the vortex blobs change their positions at a larger distance. Although in such cases stronger vortices are formed in the boundary

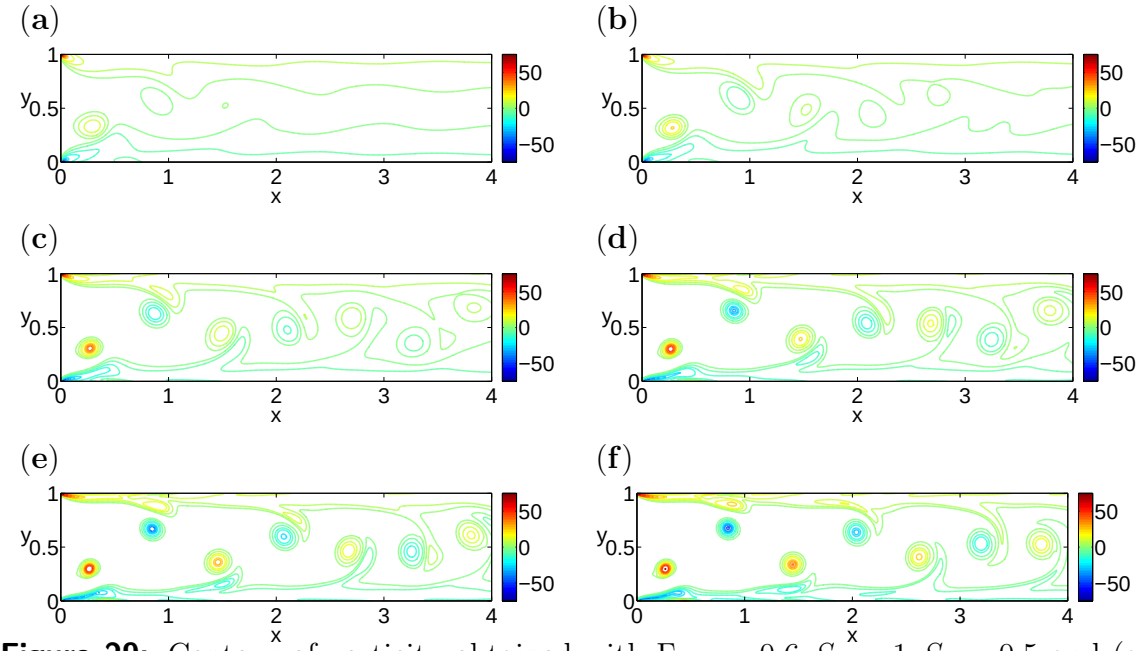

Figure 29: Contour of vorticity obtained with $\Gamma_r = -0.6, S_a = 1, S_b = 0.5$ and (a) Re=100; (b) Re=200; (c) Re=500; (d) Re=1000; (e) Re=1500; (f) Re=2000.

layer and lead to stronger interactions between the blobs and the separated vortices, the blobs themselves contain more fluid momentum which requires longer distance for inversion.

Now, we vary the relative vortex strength Γ_r and fix the other parameters. In the active vibration cases, Γ_r can tend to positive infinity as the background flow tends to zero. However, in the passive vibration case, the induced velocities at the blobs are in the upstream direction, and therefore the background flow is necessary for the vortex blobs to enter the channel. Γ_r must satisfy the following bounds depending on the geometric structure of the incoming flow S_a and S_b:

$$-\frac{2S_a}{\tanh\left(\pi S_b/S_a\right)} \leq \Gamma_r \leq 0 \tag{50}$$

When Γ_r is close to the lower bound, the incoming flow becomes unrealistic with sharp changes between downstream and upstream flow directions. We show some of the incoming flows in figure 31. We choose $S_a = 1$ and $S_b = 0.5$, and the lower bound of Γ_r is around -2.18. As we can see in figure 31, although the velocity of the vortex blob is set to be 1, the horizontal velocity u rapidly changes from around 42 to -42

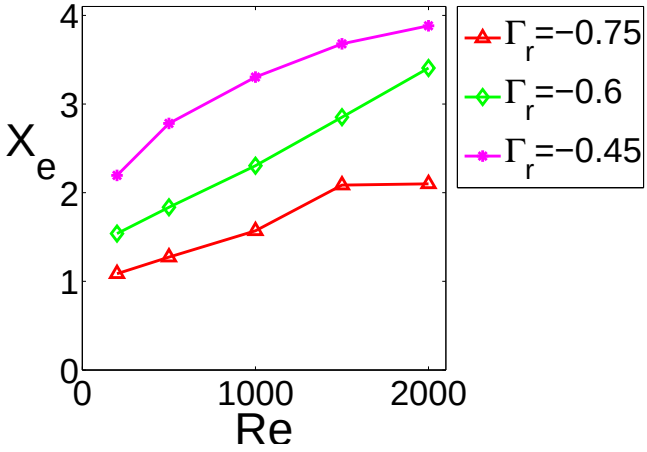

Figure 30: X_e vs. Re with $\Gamma_r = -0.45, -0.6$ and -0.75, $S_a = 1$ and $S_b = 0.5$

for $\Gamma_r = -2$, which seems physically unrealistic. Therefore, in figure 32, we only vary Γ_r from -0.15 to -1.0.

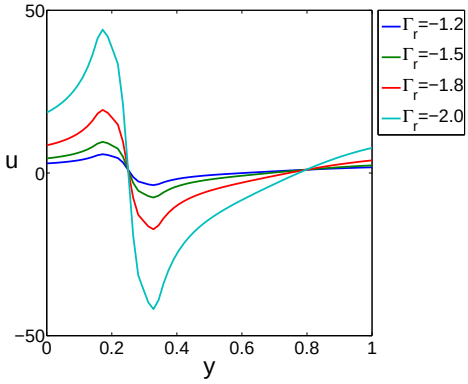

Figure 31: Velocity u of the incoming flow at $t = 1/4\tau_p$, $\Gamma_r = -1.2, -1.5, -1.8, -2.0$, $S_a = 1.0$ and $S_b = 0.5$.

We observe clearly distinct results for different Γ_r in figure 32. In general, as Γ_r becomes more negative, both the background flow and the vortex strength (in the sense of absolute value) will increase accordingly. Unlike the active vibration cases where a trade-off exists for the vortex strength and the background flow, in the passive case we obtain stronger vortex blobs and stronger boundary layer separations as well.

When Γ_r is small as shown in figure 32 (a), the blobs move towards the centerline

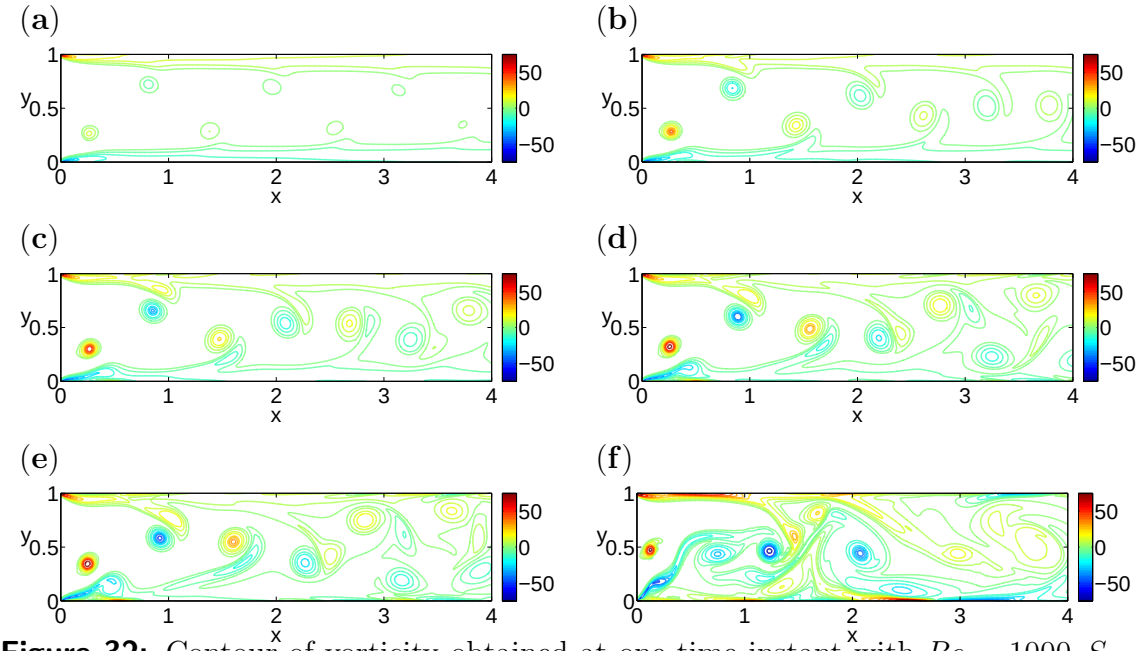

Figure 32: Contour of vorticity obtained at one time instant with $Re = 1000, S_a = 1, S_b = 0.5$ and (a) $\Gamma_r = -0.15$; (b) $\Gamma_r = -0.45$; (c) $\Gamma_r = -0.6$; (d) $\Gamma_r = -0.75$; (e) $\Gamma_r = -0.8$; (f) $\Gamma_r = -1.0$.

but do not cross it in the channel. As the magnitude of Γ_r increases, the flow becomes more and more irregular. We show the contour plot of time-averaged vorticity $\overline{\omega}$ for $\Gamma_r = -0.6, -0.75, -0.8, -1.0$ in figure 33.

We define the flows with $\Gamma_r = -0.6$ and -0.75 as a "regular street" because after the blobs cross the centerline they form a structure similar to the reverse von Kármán street flow and more importantly, the time-averaged flow is symmetric to the centerline as shown in figure 33 (a) and (b). Intuitively, the symmetry should hold for all parameters as the inflow is symmetric as well as the geometric shape of the channel. However, we find that when the interactions of the vortex blobs and the boundary layers are sufficiently strong, the flow becomes asymmetric as shown in figure 33 (c) and (d). We define such cases as "irregular street". Figure 33 (c) shows a transition case from the regular to the irregular street. For $\Gamma_r = -0.8$, the vortex street shifts to the upper half of the channel after negative and positive blobs change the positions, but as we can see in figure 32 (e) the fluid is still similar to a vortex street as the blobs form a staggered array.

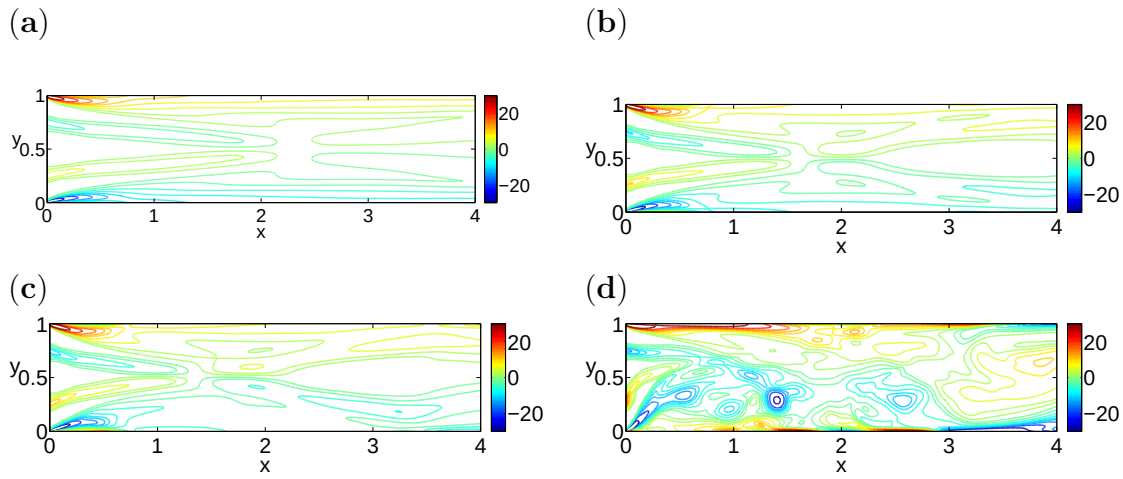

Figure 33: Contour of time-averaged vorticity obtained with $Re = 1000, S_a = 1, S_b = 0.5$ and (a) $\Gamma_r = -0.6$; (b) $\Gamma_r = -0.75$; (c) $\Gamma_r = -0.8$; (c) $\Gamma_r = -1.0$.

Whether the street shifts to the upper half or the lower half depends on which blob comes into the channel first. In figure 32 (e) and 33 (c), the negative blob enters the channel first at the upper half. If we change the order and have the positive blob enter the channel first at the lower half, the street will shift to the lower half.

When $\Gamma_r = -1.0$, the flow almost entirely loses the street structure except that it is still time periodic, and the flow behaves chaotically over the whole channel for both the time instant and the time average solutions. In this case, the vortices separated from the wall are comparable in strength with the vortex blobs, and the interactions between the separated vortices themselves overwhelm the interactions between the blob and the separated vortex, and thus destroy the structure of the vortex street.

For the regular street, we can also measure the exchange distance X_e versus the Γ_r. When Γ_r becomes more negative, both the background flow and the vortex blobs become stronger, therefore the blobs cross the centerline faster as the interactions are stronger. In figure 30 and later in figures 35 and 39, we observe that as Γ_r becomes more negative, X_e decrease accordingly.

In figure 34, we vary the value of S_b and keep the other parameters fixed. As S_b increases, both U_b and Γ (in the sense of absolute value) increase correspondingly.

Moreover, when S_b is large, the vortex blobs are closer to the wall and their interactions with the wall separations are stronger as well. Therefore we expect to observe more irregular streets when S_b becomes larger. Figures 34 (a), (b) and (c) show contour plots of vorticity with regular streets and figure 34 (d) shows an irregular street. We note that although figure 34 (c) looks complicated at the end of the channel, it is still a regular street as its time-averaged vorticity is symmetric with respect to the centerline.

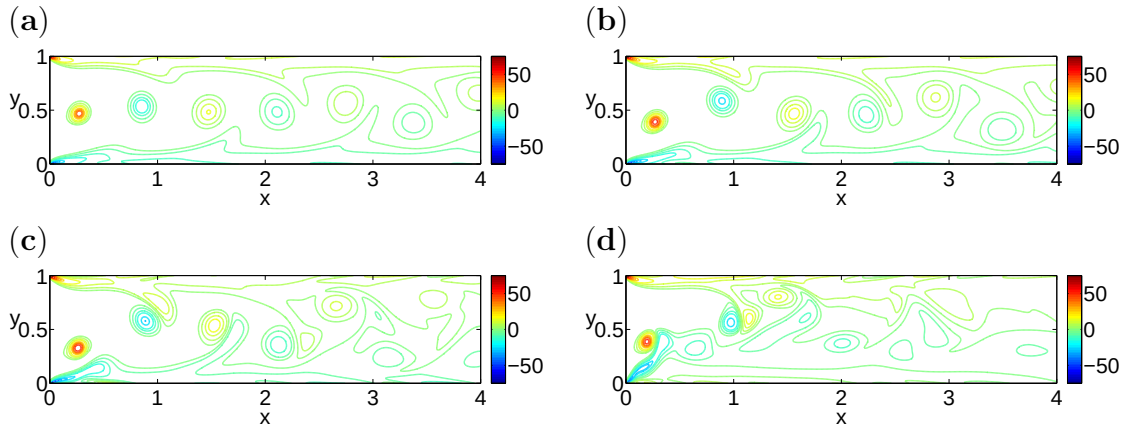

Figure 34: Contour of vorticity obtained with $Re = 500, \Gamma_r = -0.75, S_a = 1$ and (a) $S_b = 0.1$; (b) $S_b = 0.3$; (c) $S_b = 0.5$; (d) $S_b = 0.7$.

Figure 35 shows the relationship between X_e and S_b for different Γ_r. We only consider X_e for regular flows. Therefore, when the data is missing, for example, $\Gamma_r = -0.8$ and $S_b = 0.6$, it indicates that for that parameter value, the flow becomes irregular. When the blobs are closer to the wall, although the wall interactions are stronger, the blobs are also further from the centerline and require a longer distance before inverting their positions. Therefore, the largest X_e is obtained at a moderate value of S_b instead of at the boundaries.

When S_b is zero, all the negative and positive blobs are aligned on the centerline of the channel and the blob induced velocity is zero. They rely on the background flow to be flushed into the channel. Since we obtain U_b by the formula $U_b = \dfrac{1}{1 + \Gamma_r/2S_a(\tanh(\pi S_b/S_a))}$, U_b always equals 1 when $S_b = 0$ regardless of other

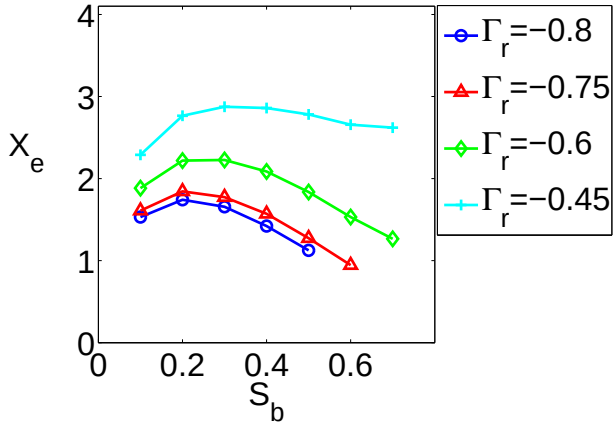

Figure 35: X_e vs. S_b with $\Gamma_r = -0.45, -0.6, -0.75$ and -0.8, $S_a = 1$ and $Re = 500$.

parameters. And the value of Γ_r therefore only determines the blob strength Γ. This position is very unstable and small perturbations lead to very different flows. In fact, when the blobs move into the channel, there will only be a finite number of blobs and their induced velocities do not totally cancel with each other. Therefore, the blobs will shift away from the centerline and form a street similar to the reversed von Kármán street with positive blobs in the upper half and negative blobs in the lower half of the channel. There is no difference between the active and passive vibration case when $S_b = 0$, as we can view the active vibration case as the passive one but taking a half period ahead. We show the contour plot of vorticity when $S_b = 0$ in figure 36.

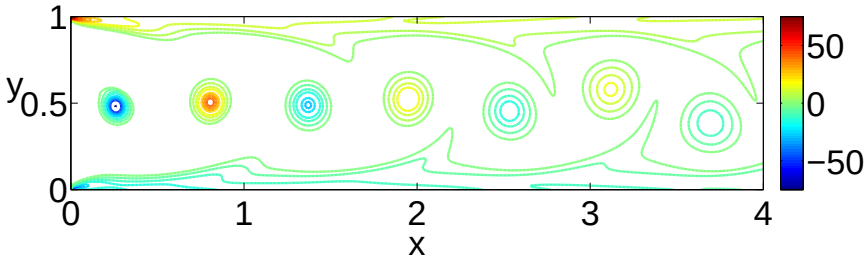

Figure 36: Contour of time instant vorticity with $S_b = 0$, $Re = 500$, $\Gamma_r = 1$ and $S_a = 1$

In figure 37, we change the value of S_a and keep the other parameters unchanged. Similar to S_b, as S_a decreases, both U_b and Γ (in the sense of absolute value) increase correspondingly. And when S_a is small, the vortex blobs are closer to each other as well as the wall separated vorticity corresponding to each blob. The interactions are stronger and we expect to observe more irregular streets when S_a becomes smaller as shown in figure 37 (a).

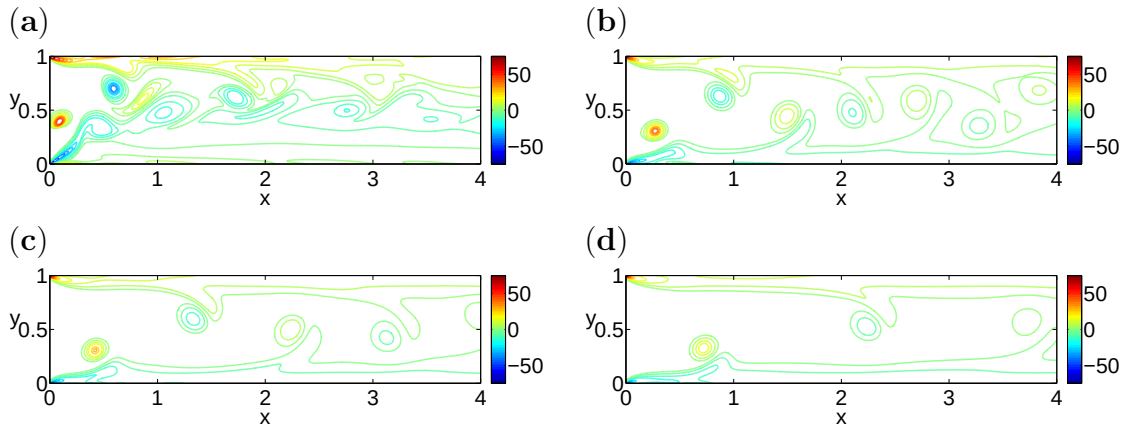

Figure 37: Contour of vorticity obtained with $Re = 500, \Gamma_r = -0.6, S_b = 0.5$ and (a) $S_a = 0.5$; (b) $S_a = 1.0$; (c) $S_a = 1.5$; (d) $S_a = 2.5$.

When S_a tends to zero, the inflow is composed of two vortex layers and the flow in the channel is similar to the time averaged flow as shown in figure 33. When S_a tends to infinity, only a single vortex blob is in the channel. We show the contour plot of vorticity for the active and passive vibration case in figure 38.

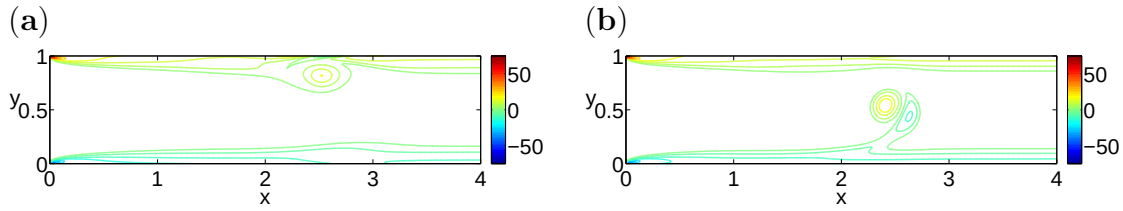

Figure 38: Contour of vorticity obtained with $Re = 1000, S_b = 0.5$ and $S_a \to \infty$ for (a) active vibration $\Gamma_r = 1$; (b) passive vibration $\Gamma_r = -1$.

It is easier to identify the functions of interactions between different blobs and between the blob and the boundary layer when only one blob exists in the channel. In

figure 38 (a), the blob is closer to the wall compared to those in figure 15. The interactions between different blobs help to maintain the vertical positions of the blobs in the channel. In figure 38 (b), the blob crosses the centerline under the pure influence of the wall separation. In another words, the "crisscross" motion happens mainly due to the wall separation instead of the interaction between blobs, and it is consistent with the previous observations in figure 28 that under the symmetry boundary conditions with no wall separations the blobs do not exchange their positions.

Figure 39 shows the relationship between X_e and S_a for different Γ_r. Again we

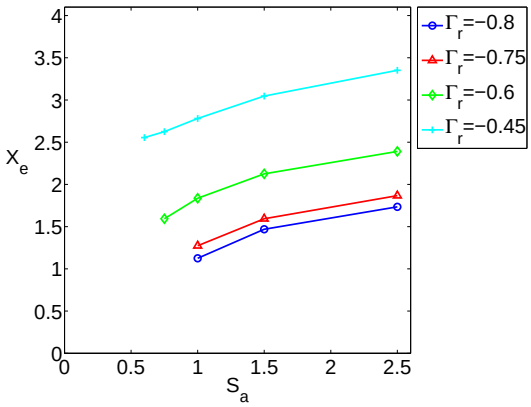

Figure 39: X_e vs. S_a with $\Gamma_r = -0.45, -0.6, -0.75$, and -0.8, $S_b = 0.5$ and $Re = 500$.

only consider X_e for regular vortex streets, and the missing data indicates the flow is irregular at those parameters. When S_a is small, both the wall separations and the blobs are stronger, therefore X_e is smaller as shown in figure 39.

For the irregular street cases, although the flow loses most of its spatial structure, it is still time periodic. But if we let Γ_r decrease further, the flow becomes more complicated. For the time marching scheme, we show the periods required for the flow to reach a time-periodic state for different Γ_r in figure 40.

As shown in the figure, the number of periods increases rapidly as Γ_r becomes more negative. In fact, we set the maximum periods to be 200 in the simulation and for $\Gamma_r = -1.3$ and -1.4, the solutions are still non-periodic when we stop the

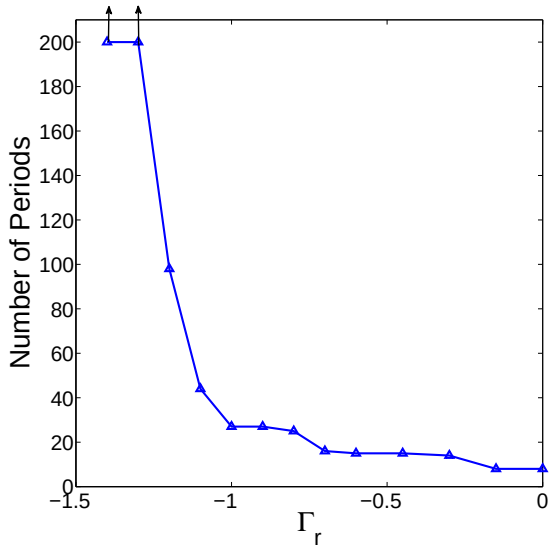

Figure 40: Number of periods to reach time-periodic state vs. Γ_r. Other parameters are $Re = 1000$, $S_a = 1$, and $S_b = 0.5$.

simulation. We define such cases as "non-periodic street" to distinguish them from the irregular street cases.

We plot the diagram of different types of vortex streets corresponding to the fluid parameters Re, Γ_r, S_a and S_b in figure 41. The flow varies from regular streets to irregular streets and then to non-periodic streets as Re increases, Γ_r becomes more negative, S_a is smaller and S_b is larger. In later chapters, we show that the temperature properties are different corresponding to each vortex street type. This diagram helps us choose the right type of vortex street.

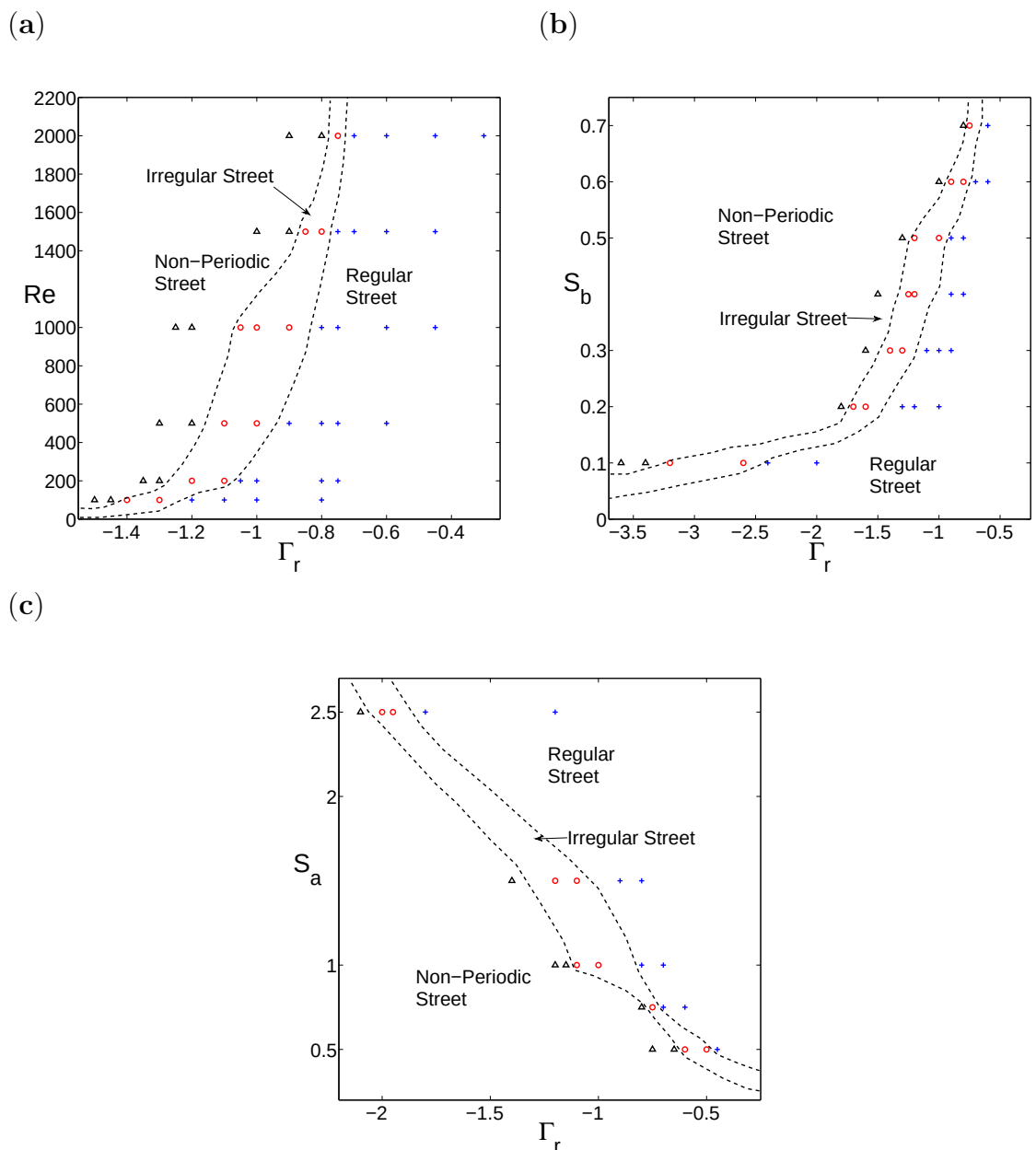

Figure 41: Diagram of vortex street type for (a) Re and Γ_r with $S_a = 1$ and $S_b = 0.5$. (b) S_b and Γ_r with $Re = 500$ and $S_a = 1$. (c) S_a and Γ_r with $Re = 500$ and $S_b = 0.5$.

CHAPTER IV

HEAT TRANSFER ENHANCEMENT BY THE VORTICITY

We now consider the heat transfer process due to the flows just described and investigate how the vorticity in the flow improves the efficiency of the heat transfer. The temperature shows different characteristics for active and passive vibration cases.

4.1 Model

In this section, we derive a model to simulate the heat transfer process. We add two hot solid slabs at the walls of the channel to provide heat sources. Flows with vortices enter the at the left channel and heat exchange occurs on the two walls and throughout the flow. The channel is again of length L and height H, and each solid slab has a height $H/4$. A schematic figure of the computational domain is shown in figure 42.

The temperature of the fluid and the solid are determined by a convection-diffusion equation and a diffusion equation with a source term , respectively:

$$\frac{\partial T_f}{\partial t} + \mathbf{u} \cdot \nabla T_f = \alpha_f \Delta T_f \tag{51}$$

$$\frac{\partial T_s}{\partial t} = \alpha_s \Delta T_s + q \tag{52}$$

Here $T_f(x, y, t)$ and $T_s(x, y, t)$ stand for the temperature of the flow and the solid. q is the heat source strength with units (K/s). In this work, we only consider a constant heat source for simplicity, and the work can be generalized to more complicated heat sources without any difficulties. $\mathbf{u} = (u, v)$ is the fluid velocity in the channel. α_f and α_s are the thermal diffusivities of the fluid and the solid respectively. We neglect the affect of temperature on fluid density, and only consider the one-way coupling

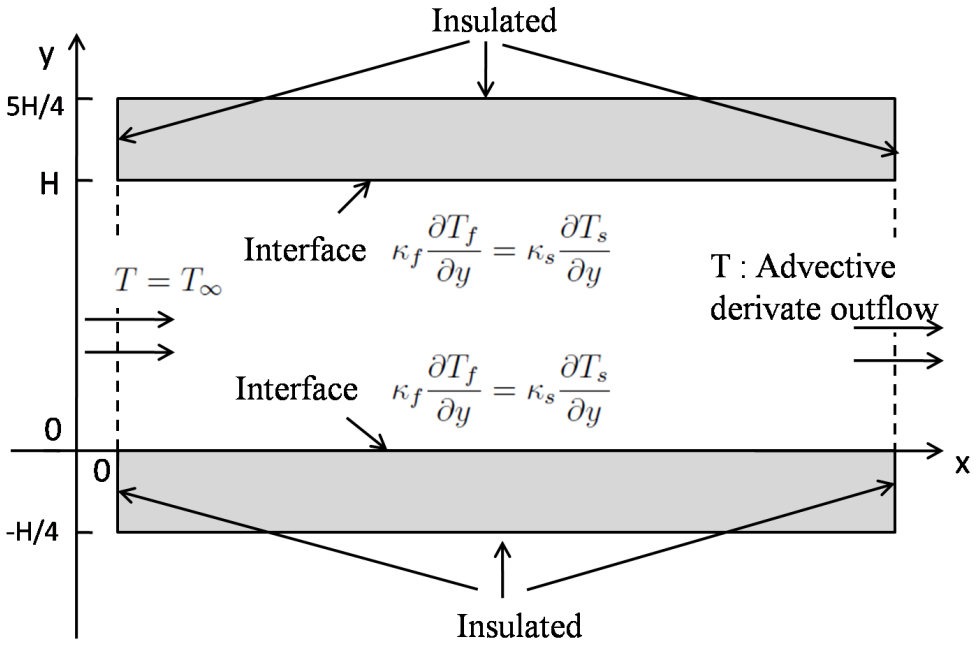

Figure 42: Schematic of the computational domain. The channel has a length L and height H, and each solid is of the same length and height $H/4$. Dirichlet boundary conditions of the temperature are applied at the entrance of the channel. Advective derivative condition is applied to fluid temperature at the outflow. Insulated conditions are applied at all sides of the solids except the wall where interface equations are used.

from fluid to the temperature. This assumption is acceptable as in the regime of the interested parameter spaces, the Grashof number (Gr) which approximates the ratio of buoyancy to viscous force on the fluid, is typically small, and $Gr/Re^2 \ll 1$ which indicates that the natural convection can be neglected.

The fluid and solid temperatures are coupled on the wall interface by the following equations:

$$\kappa_f \left.\frac{\partial T_f}{\partial y}\right|_{y=0^+,H^-} = \kappa_s \left.\frac{\partial T_s}{\partial y}\right|_{y=0^-,H^+} \tag{53}$$

It states that the heat flux out of the solid is equal to that into the fluid at their interface.

Insulating conditions, i.e. adiabatic conditions, are applied for the temperature at all sides of the solids except the fluid interfaces. Therefore, the heat can only leave

the solids through the fluid. The temperature of the incoming flow is chosen to be the far field temperature T_∞, and an advective derivative boundary condition similar to that of ω and ψ in equations (14) and (15) is prescribed at the outflow boundary. We summarize all the boundary conditions and list them here:

$$T_f = T_\infty \quad , \quad x = 0, 0 \le y \le H \tag{54}$$

$$\frac{\partial T_f}{\partial t} + \bar{u}\frac{\partial T_f}{\partial x} = 0 \quad , \quad x = L, 0 \le y \le H \tag{55}$$

$$\frac{\partial T_s}{\partial y} = 0 \quad , \quad 0 \le x \le L, y = -\frac{H}{4}, \frac{5H}{4} \tag{56}$$

$$\frac{\partial T_s}{\partial x} = 0 \quad , \quad -\frac{H}{4} \le y < 0, x = 0, L \tag{57}$$

$$\frac{\partial T_s}{\partial x} = 0 \quad , \quad H < y \le \frac{5H}{4}, x = 0, L \tag{58}$$

4.2 Nondimensionalization

We nondimensionalize the equations based on the the far field temperature T_∞, the velocity of the incoming vortex blob U, and the height of the channel H.

The following dimensionless variables are obtained:

$$x^* = \frac{x}{H}, \quad y^* = \frac{y}{H}, \quad \mathbf{u}^* = \frac{\mathbf{u}}{U}$$
$$t^* = \frac{tU}{H}, \quad q^* = \frac{qU}{HT_\infty}, \quad T^* = \frac{T - T_\infty}{q^* T_\infty}$$

For simplicity, we will use the original notation to indicate all the dimensionless variables, so equations (51) and (52) become

$$\frac{\partial T_f}{\partial t} + \mathbf{u} \cdot \nabla T_f = \frac{1}{Pe_f}\Delta T_f \tag{59}$$

$$\frac{\partial T_s}{\partial t} = \frac{1}{Pe_s}\Delta T_s + 1 \tag{60}$$

$$\tag{61}$$

and the interface equation becomes

$$\gamma_{fs} \left.\frac{\partial T_f}{\partial y}\right|_{y=0^+,1^-} = \left.\frac{\partial T_s}{\partial y}\right|_{y=0^-,1^+} \tag{62}$$

with several important dimensionless parameters:

1. $Pe_f = \dfrac{HU}{\alpha_f}$, the Péclet number of the fluid.

2. $Pe_s = \dfrac{HU}{\alpha_s}$, the Péclet number of the solid.

3. $\gamma_{fs} = \dfrac{\kappa_f}{\kappa_s}$, the ratio of thermal conductivities of the fluid and the solid.

Péclet number functions similarly to the Reynolds number and measures the ratio of the advective heat transfer to the diffusive heat transfer.

4.3 Numerical Methods

The fluid temperature is governed by a convection diffusion equation in which the velocity is determined by the Navier-Stokes equations. When the velocity is time-periodic, we expect time periodic solutions to the advection-diffusion equation as well. The most standard numerical methods for solving such system of equations is to apply a time-marching scheme and solve the initial value problems until time periodic solutions are achieved. This is the method we apply when solving the Navier-Stokes equations in chapter 2.

In active vibration cases, the development of the periodic flow typically takes approximately 20 periods to achieve the time periodic solutions starting from a still flow. In passive vibration cases, the number of periods depends on the parameters as shown in figure 40. For most regular and irregular streets, it takes at most 100 periods to obtain a time periodic solution from a still flow. However, the temperature equations develop comparatively slow than the fluid equations. For example, if the initial value of the fluid and solid temperature are set to be the far field temperature T_∞, it generally takes more than 1500 periods to obtain the time periodic temperature field.

Therefore, instead of the standard initial value problems and the time marching scheme, we consider the time periodic problem directly and design a numerical scheme that can solve the values of the temperature over the whole period simultaneously.

We design our scheme based on the multigrid algorithm proposed by Hackbusch [32] for solving time-periodic parabolic problems. We first rewrite the equations as the following:

$$\frac{\partial T}{\partial t} + ET = g_1, \quad (\mathbf{x}, t) \in \Omega \times (0, \tau_p) \tag{63}$$

$$BT = 0, \quad (\mathbf{x}, t) \in \partial\Omega \times (0, \tau_p) \tag{64}$$

$$T(\cdot, 0) = T(\cdot, \tau_p), \qquad \mathbf{x} \in \Omega \tag{65}$$

where $\Omega = [0, L] \times \left[-\frac{H}{4}, \frac{5H}{4}\right]$ is the spatial domain, τ_p is the time period, $E = (\mathbf{u} \cdot \nabla + \Delta)$ is the convection diffusion operator for fluid temperature and Laplacian operator for solid temperature, and B defines all the boundary conditions except the fluid temperature at the exit. At that boundary, T satisfies the advective derivative condition $\frac{\partial T}{\partial t} + \bar{u}\frac{\partial T}{\partial x} = 0$, and we combine it in equation (63). Therefore, all the other boundary conditions are either Dirichlet condition $T = 0$ at the entrance of the channel, or Neumann condition $\frac{\partial T}{\partial \mathbf{n}} = 0$ where $\mathbf{n}$ is the outer normal vector at the boundary.

We introduce a new linear mapping $\mathbf{K}$ which maps any $T_0 = T(\cdot, 0)$ to $T(\cdot, \tau_p)$ according to equations (63) and (64) but with homogenous right hand side $g_1 = 0$. And we define $T_I = T(\cdot, \tau_p)$ as the solution of equations (63) and (64) obtained at $t = \tau_p$ with the non-homogeneous condition g_1 and initial value $T(\cdot, 0) = 0$. Therefore, we can view the original periodic problem (63) - (65) as finding T satisfying the following equation:

$$T = \mathbf{K}T + T_I. \tag{66}$$

Similarly, we can define the corresponding discretized operator and equations as

$$T_h = \mathbf{K}_h T_h + T_{Ih}. \tag{67}$$

$\mathbf{K}_h$ depends on the discretization of the original problem. For example, if we apply an implicit scheme to equation (63) as

$$T(\mathbf{x}, t) - T(\mathbf{x}, t - dt) + \Delta t\, L_h(\mathbf{x}) T(\mathbf{x}, t) = 0 \tag{68}$$

Then $\mathbf{K}_h$ is the matrix

$$\mathbf{K}_h = (I + \Delta t L_h)^{-\tau_p/\Delta t} \tag{69}$$

In the actual computation, we do not need to form $\mathbf{K}_h$ explicitly. Instead, we only need to apply a standard time marching scheme with the initial value T_h and simulate from $t = 0$ to $t = \tau_p$.

Therefore, we can consider the following multigrid algorithm: Let l be the actual level number, i be the number of iterations, and T_I be the non-homogeneous solution at any step. We define K_l to be the discretized mapping at level l,

$$R_{l,l-1} : L_l^2 \to L_{l-1}^2$$

as the restriction from level l to level $l-1$, and

$$P_{l,l+1} : L_l^2 \to L_{l+1}^2$$

as the piecewise linear interpolation from grid level l to level $l+1$. Then we have the following multigrid algorithm $mgm(i, l, T, T_I)$ on level l:

Algorithm 1 Multigrid V-Cycle

Multigrid V-Cycle:mgm(i, l, T, T_I)

```
1: if l = 1 then
2:     T := (I − K_0)^{-1} * T_I;
3: else
4:     for j = 1 : i do
5:         T := K_l T + T_I;
6:         d := R_{l,l−1} * (T − K_l T − T_I);
7:         v := mgm(2, l − 1, 0, d);
8:         T := T − P_{l−1,l} * v;
9:     end for
10: end if
```

And a full-cycle multigrid algorithm with total level L is given in algorithm 2.

The procedure mgm requires a repeated performance of the mapping $T_j \to K_j T_j + T_I$ at different grid levels. For the coarsest grid, the solution of $T_1 := (I - K_1)^{-1} * T_I$ is obtained by solving the original time periodic problem directly. We consider the

Algorithm 2 Multigrid Full-Cycle

Multigrid Full-Cycle

1: $T_1 := (I - K_1)^{-1} * T_I$;
2: **for** $j = 2 : L$ **do**
3: Compute T_I at level j;
4: $T_j = P_{j-1,j} * T_{j-1}$;
5: mgm$(1, j, T_j, T_I)$
6: **end for**

time variable as the third dimension and construct a 3-dimensional grid. The total number of equations is $N \times M \times S$ where S is the number of grid points in time. We apply a Crank-Nicolson scheme to discretize equations (59) and (60) and central difference are used for spatial derivatives.

$$\frac{T_f(i,j,k+1) - T_f(i,j,k)}{dt} + \frac{1}{2}\left(u^k \cdot \nabla T_f(\cdot,k) + u^{k+1} \cdot \nabla T_f(\cdot,k+1)\right) = \frac{1}{2Pe_f}(\Delta T_f(\cdot,k) + \Delta T_f(\cdot,k+1)) \tag{70}$$

$$\frac{T_s(i,j,k+1) - T_s(i,j,k)}{dt} = \frac{1}{2Pe_s}(\Delta T_s(\cdot,k) + \Delta T_s(\cdot,k+1)) + 1 \tag{71}$$

The interface equations are discretized by one-sided difference schemes since the spatial derivative represents heat flux and should be calculated through points in the same material. The discretized matrix is close to a double banded sparse matrix except at $k = 1$. We show the sparsity pattern obtained with $N = 9, M = 17$ and $S = 8$ in figure 43 and we can see the extra bands of non-zeros on the right top corner.

For other grid sizes, $K_j T_j$ is obtained by solving an initial value problem with $T(\cdot, 0) = T_j$ up to $t = \tau_p$.

Hackbusch [32] showed certain smooth properties for $\mathbf{K}$ and $\mathbf{K}_h$ and convergence results in his work. He proved that with a sequence of decreasing size step: $h_l = \frac{h_1}{2^l}, \Delta t_l = \lambda h_l^2 = \frac{\Delta t_1}{4^l}$ and a piecewise linear interpolation P, the iteration error of the above algorithm between each levels is proportional to h_l^s, $(0 \leq s \leq 2)$. Therefore one or two step of the iteration usually yields a result with sufficiently small iteration error, provided that h_1 and t_1 is small enough. The convergence study of the numerical

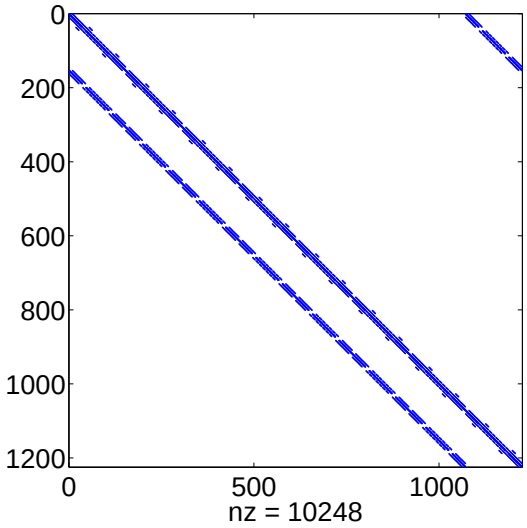

Figure 43: Pattern for the sparse matrix at the coarsest grid.

solver is shown in Appendix.

Therefore, in the actual computation, we first obtain the velocity profile **u** of one period from methods described in chapter 2, and then use it to compute the time period solutions of the temperature equations.

4.4 Results and Discussions

There are many quantities that can be applied to measure the heat transfer performance. In this work, we mainly consider the Nusselt number (Nu) and the wall temperature.

In heat transfer at a fluid boundary, the Nusselt number is the ratio of convective to conductive heat transfer across the boundary [42]:

$$Nu = \frac{hL}{\kappa} \tag{72}$$

where h is the convective heat transfer coefficient of the flow, L is the characteristic length of flow variations normal to the boundary and κ is the thermal conductivity of the fluid.

At a flat boundary, the heat transfer rate for a small region with area A and constant temperature T_w can be written as

$$Q = hA(T_w - T_\infty) \tag{73}$$

here T_∞ is the far field temperature. Neglecting radiation, the heat transfer is only through conduction at a surface:

$$Q = \kappa A \frac{\partial}{\partial y} (T - T_w)|_{y=wall} \tag{74}$$

Therefore, we have

$$\frac{hL}{\kappa} = \frac{\frac{\partial}{\partial y} (T - T_w)|_{y=wall}}{\frac{T_w - T_\infty}{L}} \tag{75}$$

According to the previous nondimensionalization:

$$x^* = \frac{x}{H}, \quad q^* = \frac{qU}{HT_\infty}, \quad T^* = \frac{T - T_\infty}{q^* T_\infty}$$

We have the following dimensionless expression for Nu:

$$Nu(x,t) = \frac{hH}{\kappa} = \frac{1}{T_w(x,t)} \left. \frac{\partial T(x,y,t)}{\partial y} \right|_{y=wall} \tag{76}$$

We note that all the variables in the above equation are dimensionless. We keep them as in the old notations just for simplicity. The above expression is a local definition and we also consider the following averaged Nusselt numbers:

1. $Nu_t(x) = \frac{1}{\tau_p} \int_0^{\tau_p} Nu(x,t)\, dt$ - time averaged Nu over one period τ_p.
2. $Nu_g = \frac{1}{L} \frac{1}{\tau_p} \int_0^{\tau_p} \int_0^L Nu(x,t)\, dxdt$ - spatial and time averaged Nu over the channel within one period.

Nusselt number can be viewed as a dimensionless temperature gradient at the wall. If κ is fixed, then larger Nu indicates larger heat flux through the channel wall and therefore better heat transfer performance. Nusselt number is affected by the fluid

parameters Re, Γ_r, S_a and S_b through their affect on velocity profile $\mathbf{u}$, as well as the temperature parameters γ_{fs}, Pe_f and Pe_s. In the following sections, we will discuss the affect of fluid and temperature parameters separately.

4.4.1 Fluid Parameters

4.4.1.1 Active Vibration Cases

We first consider the active vibration cases. As we have shown in previous sections, in the active vibration cases, all the flows have similar structures with vortex blobs mainly moving in the downstream direction. Therefore, temperature profiles corresponding to different fluid parameters are similar as well.

In figure 44 (a), we show the contour plot of both fluid and solid temperatures at one time instant, and we plot the corresponding vorticity contour at the same time instant in figure 44 (b).

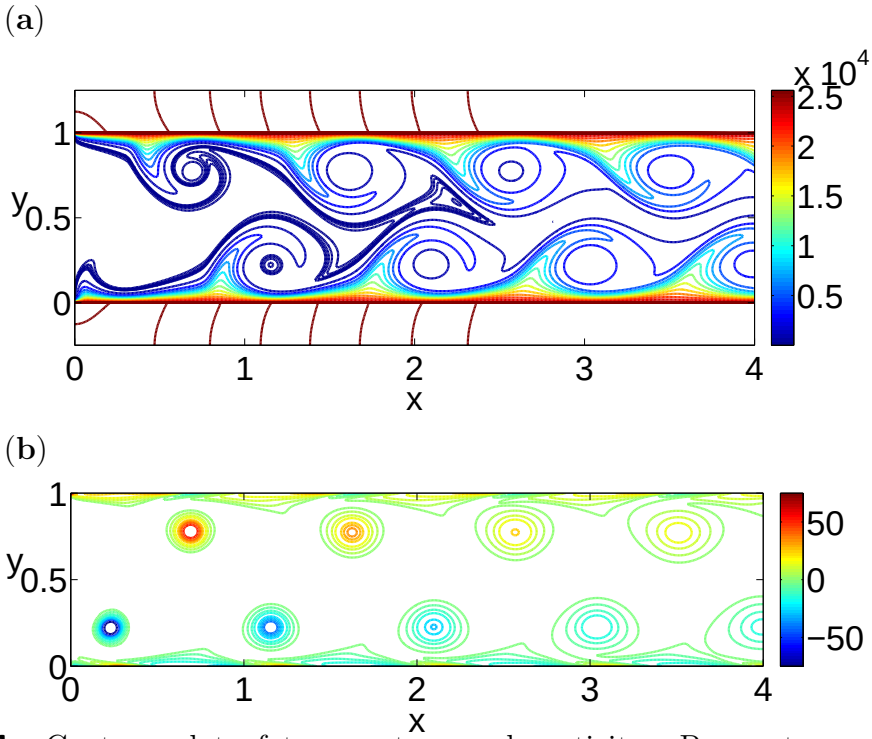

Figure 44: Contour plot of temperature and vorticity. Parameters used in this simulation are $Re = 1000$, $\Gamma_r = 6$, $S_b = 0.5$, $S_a = 1$, $\gamma_{fs} = 1e-4$, $Pe_f = 500$, and $Pe_s = 125$. (a) Fluid and solid temperature contour plot; (b) corresponding vorticity contour plot.

The two channel walls are located at $y = 0$ and $y = 1$, and they are the fluid-solid interfaces. The solid temperature is close to uniform along the y-direction and the main variation is along the x-direction. Due to the vorticity, the fluid temperature forms a structure similar to the vortex street. The vortex blob brings cooler fluid from the center of the channel to the hotter boundary layer in front of the blob, and takes the hotter fluids out of the boundary layer at the back of the blob. Therefore, the vortex blob cools down the region between the vortex blob and the wall, and at the same time create a larger temperature gradient. We illustrate this by plotting the wall temperature and the local Nusselt number at the beginning of the period in figure 45. We plot data for the lower wall at $y = 0$ with solid lines and data for the upper wall at $y = 1$ with dashed lines. We also plot the centers of the vortex blobs using upward pointing triangles for the negative blobs and downward pointing triangles for the positive ones.

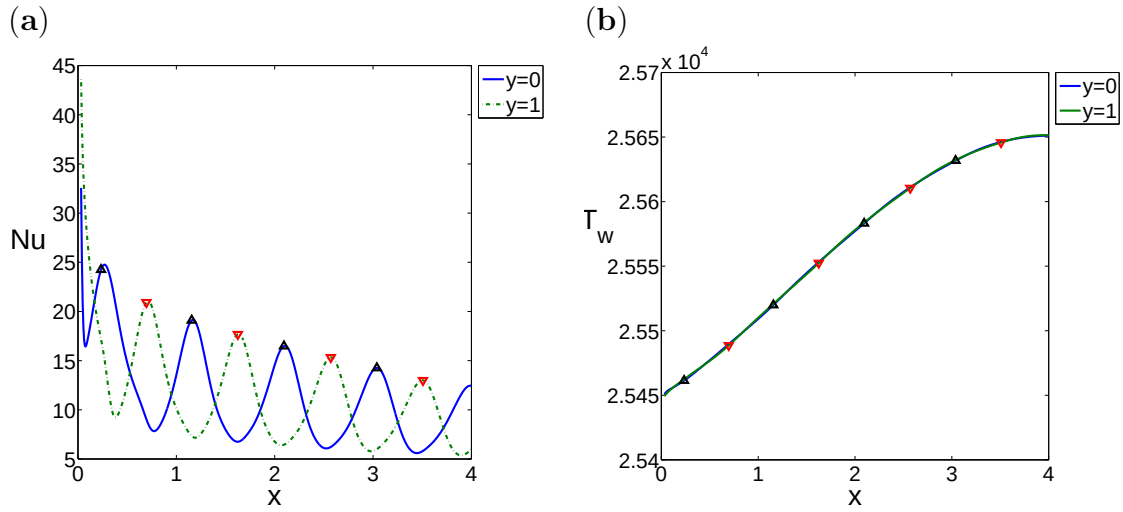

Figure 45: (a) Nu vs. x; (b) wall temperature T_w vs. x. The values are time instant ones obtained at the beginning of a period. The solid lines indicate values for the lower wall at $y = 0$, and the dashed lines are for values at the upper wall $y = 1$. Upward pointing triangles show the center of the negative vortex blobs and downward pointing triangles are for the positive ones. Parameters used here are $Re = 1000$, $\Gamma_r = 6$, $S_b = 0.5$, $S_a = 1$, $\gamma_{fs} = 1e-4$, $Pe_f = 500$, and $Pe_s = 125$.

In figure 45 (a), the Nusselt number varies up and down over the channel with

the local peaks located at the vortex blobs' centers. The Nusselt number has a large variation across the channel. The wall temperature, on the other hand, is close to constant over the channel with a variance less than 1%. Therefore, the maximum Nu is obtained at the entrance of the channel as the cool far field flow create the largest temperature gradient near the wall.

To better understand how the Nusselt number is improved by the vorticity, we compare the result for $\Gamma_r = 6$ with the result for $\Gamma_r = 0$ in figure 46.

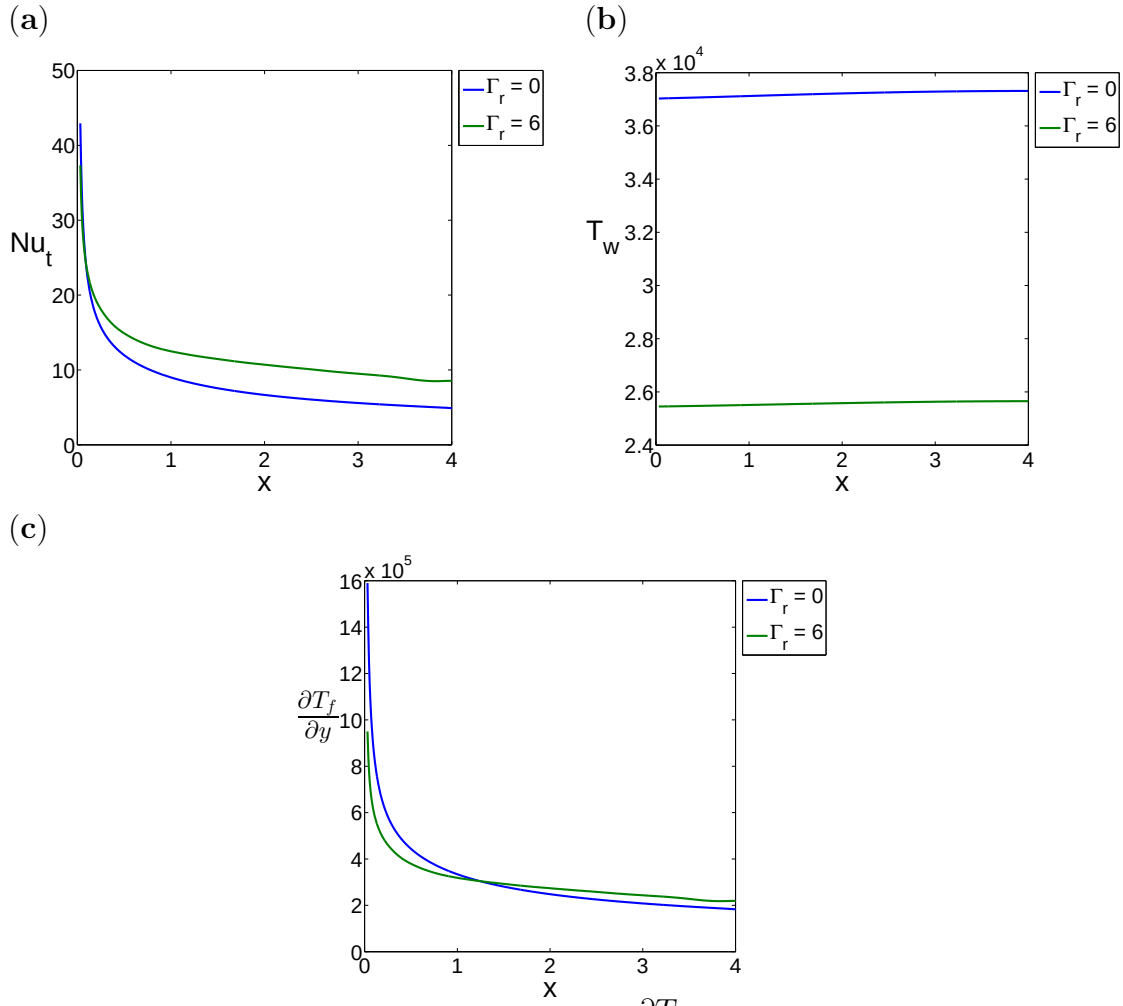

Figure 46: (a) Nu_t vs. x; (b) T_w vs. x; (c) $\dfrac{\partial T_f}{\partial y}$ vs. x for $\Gamma_r = 0$ and 6. Other parameters used here are $Re = 1000$, $S_a = 1$, $S_b = 0.5$, $Pe_f = 500$, $Pe_s = 125$, $\gamma_{fs} = 1e-4$.

We note that $\Gamma_r = 0$ corresponds to the flow without incoming vortex blobs and that flow becomes a Poiseuille flow in the steady state. We compare the local Nusselt

number, the wall temperature and the wall temperature gradient in panels (a), (b) and (c). Instead of the time instantaneous values, we use time-averaged ones in the comparison. We note that in active vibration cases, the time-averaged values are the same for both walls, and thus we only plot the values for lower wall in figure 46.

At the beginning of the channel, we notice that the wall temperature gradient is larger for $\Gamma_r = 0$. However, it decreases rapidly along the channel, while for $\Gamma_r = 6$, the wall temperature gradient varies little and is larger than that of the Poiseuille flow eventually as shown in figure 46 (c). Meanwhile, the wall temperature is much smaller for $\Gamma_r = 6$, and thus improves the Nusselt number Nu_t as shown in figure 46 (a). Therefore, the vorticity improves the heat transfer performance in two aspects: it decreases the temperature of the solids and reduces the decay of the temperature gradient in the channel.

Now, we vary the fluid parameters to better understand how the heat transfer efficiency is affected by the fluid parameters. We first vary Γ_r and fix the other parameters. We consider the global Nusselt number as an overall measurement for the heat transfer efficiency:

$$Nu_g = \frac{1}{L}\frac{1}{\tau_p}\int_0^{\tau_p}\int_0^{L} Nu(x,t)\,dxdt$$

We note that Nu_g is defined on each wall separately, and we can further take the averaged values for both wall Nu_g to globally measure the heat transfer performance. In active vibration cases, the time-periodic temperatures are symmetric to the centerline of the channel, therefore the Nu_g for both walls and the averaged one are essentially the same. We plot Nu_g versus different Γ_r in figure 47 (a) and we can see that all three lines collapse with each other very well.

The global Nusselt number increases according to Γ_r. We also plot the local Nu_t, the wall temperature T_w and the wall temperature gradient $\dfrac{\partial T_f}{\partial y}$ for different Γ_r in figures 47 (b), (c) and (d). Again, all the results shown in these panels are time-averaged values.

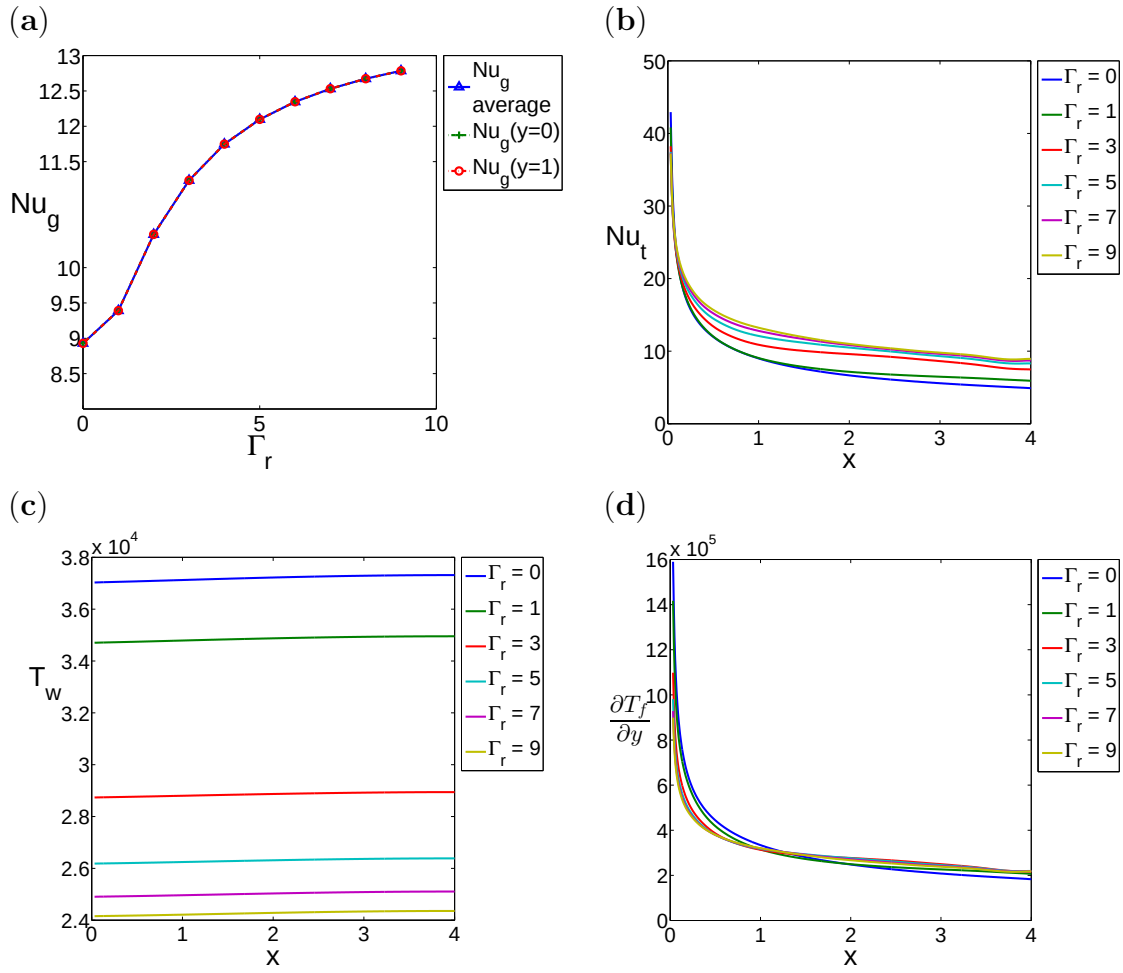

Figure 47: (a) Nu_g vs. Γ_r. (b) Nu_t vs. x; (c) T_w vs. x; (d) $\dfrac{\partial T_f}{\partial y}$ vs. x for $\Gamma_r = 0, 1, 3, 5, 7, 9$. Other parameters used here are $Re = 1000$, $S_a = 1$, $S_b = 0.5$, $Pe_f = 500$, $Pe_s = 125$, $\gamma_{fs} = 1e-4$.

We notice that the temperature gradient doesn't have big variances for different Γ_r as shown in panel (d). The change in the Nusselt number is mainly caused by the decrease of the wall temperature as Γ_r increases. And we also noticed that local Nu_t for nonzero Γ_r is larger the $\Gamma_r = 0$ case throughout the channel, and moreover, the largest difference happens at the exit of the channel. This is in consistent with the observation in Gerty's experiments [29].

Now, We vary Re and fix the other parameters. We plot the global Nusselt number Nu_g, the local Nusselt number Nu_t, the wall temperature T_w and the temperature gradient $\frac{\partial T_f}{\partial y}$ for different Re in figure 48. Again, all the local values in the figures 48 (b), (c) and (d) are time-averaged values. And for Nu_g, the value for both walls and the averaged one collapse with each other in figure 48 (a).

As Re increases, the diffusion effect is weaker and the vortex blobs are able to maintain their strength throughout the channel. Therefore, the temperature gradient at the wall decreases more slowly along the x direction for larger Re as shown in figure 48 (d). Meanwhile, the wall temperature is also smaller, as the stronger vortex blobs are able to take away more heat from the boundary layer by forced convection due to the vorticity. Therefore, Nu_g increases with Re. In fact, the variance of the temperature gradient is very small for different Reynolds numbers, and the decrease of the wall temperature plays more significant role in the increase of the Nusselt number.

Similarly, we consider the effect of S_b in figure 49.

From previous analysis, the strengths of the vortex blobs and the background flow are both smaller when S_b increases, and thus $\frac{\partial T_f}{\partial y}$ decreases more quickly with larger S_b. The change of wall temperature with S_b is more complicated. Although the stronger blobs for smaller S_b are able to bring more cooler fluids from the center of the channel to the boundary layer, these blobs are also further from the wall and have fewer interactions as shown in figure 23. Therefore, the maximum wall temperature

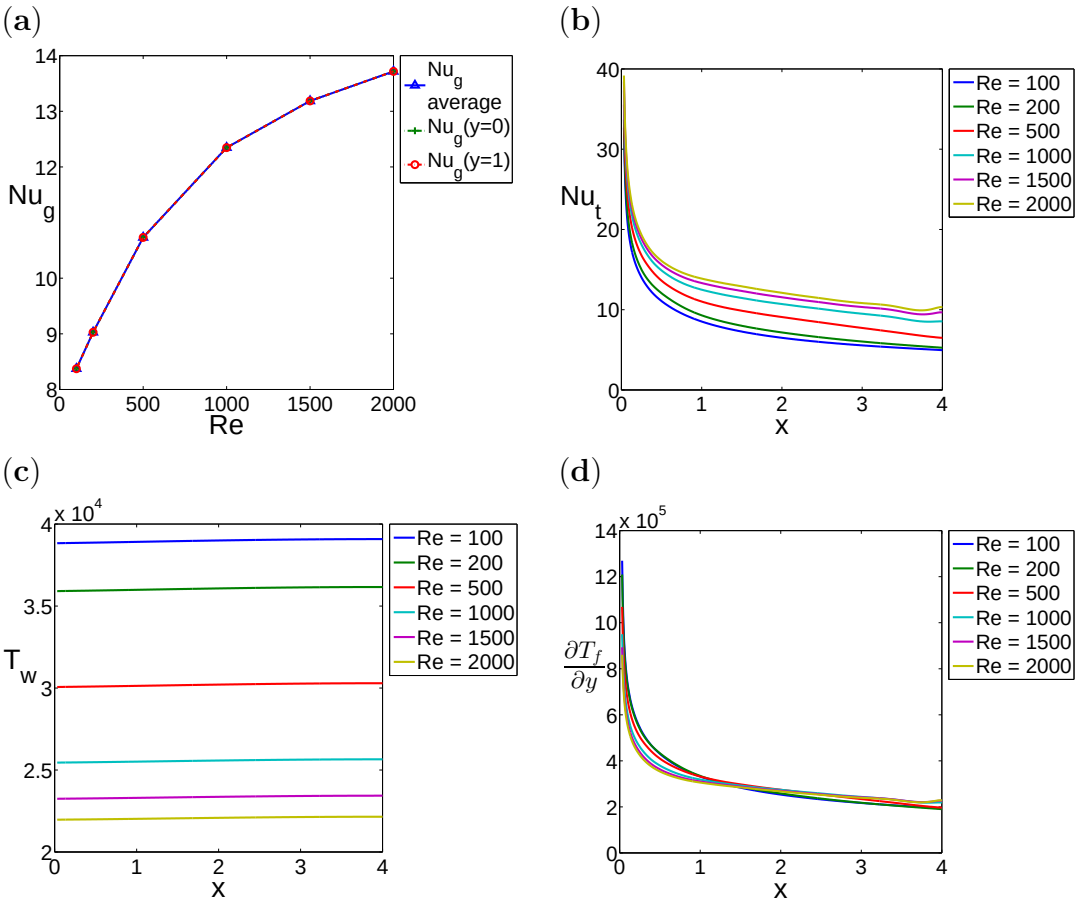

Figure 48: (a) Nu_g vs. Re. (b) Nu_t vs. x; (c) T_w vs. x; (d) $\dfrac{\partial T_f}{\partial y}$ vs. x for $Re = 100, 200, 500, 1000, 1500, 2000$. Other parameters used here are $\Gamma_r = 6$, $S_a = 1$, $S_b = 0.5$, $Pe_f = 500$, $Pe_s = 125$, $\gamma_{fs} = 1e-4$.

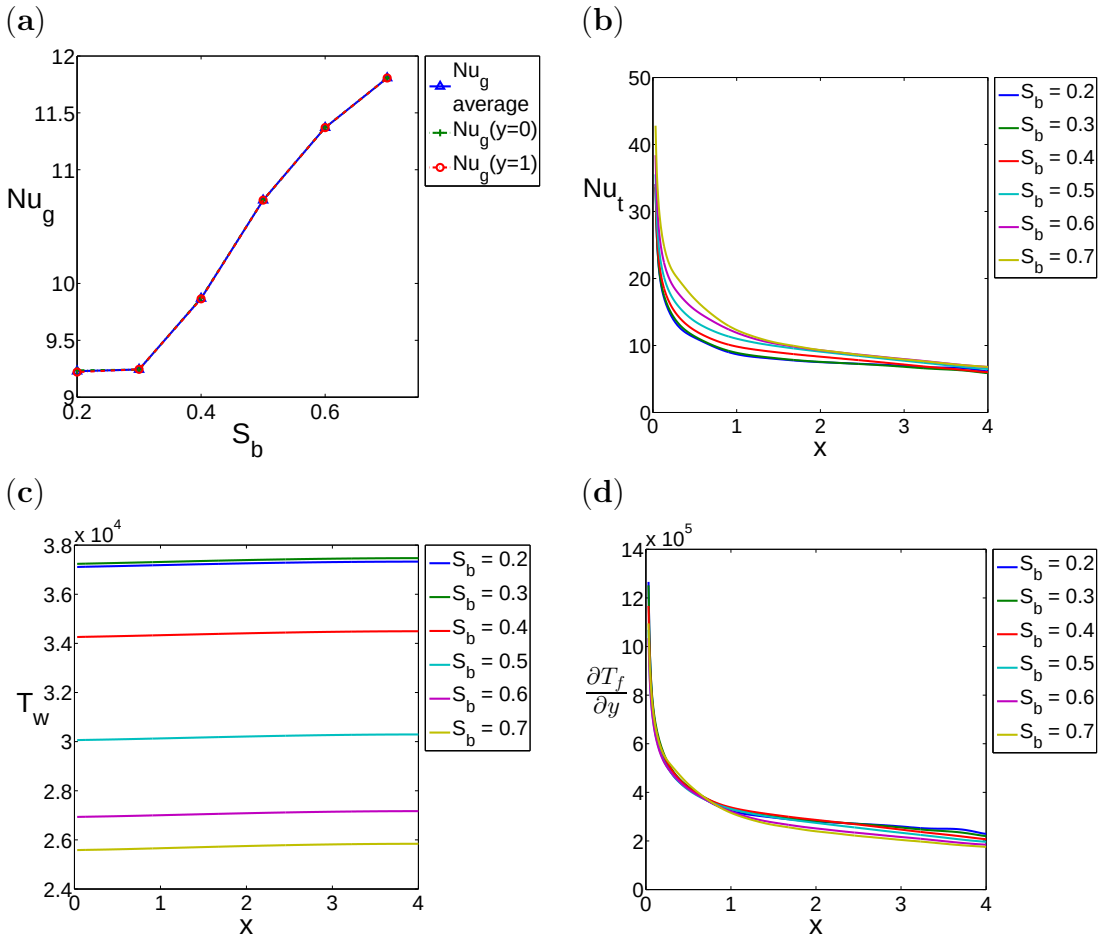

Figure 49: (a) Nu_g vs. S_b. (b) Nu_t vs. x; (c) T_w vs. x; (d) $\frac{\partial T_f}{\partial y}$ vs. x for $S_b = 0.2, 0.3, 0.4, 0.5, 0.6, 0.7$. Other parameters used here are $Re = 500$, $\Gamma_r = 6$, $S_a = 1$, $Pe_f = 500$, $Pe_s = 125$, $\gamma_{fs} = 1e-4$.

is obtained when $S_b = 0.3$ and the wall temperature decreases with S_b after that as shown in figure 49 (c). The decrease of the temperature gradient is smaller than the decrease of the wall temperature, therefore the global Nusselt number Nu_g is almost the same when S_b goes from 0.2 to 0.3 and then increases with S_b.

When S_a goes up, both the vortex blobs and the background flow becomes stronger, which improves the heat transfer efficiency. On the other hand, as S_a increases, the time period is larger and the number of blobs in the channel is less. This reduces the effect of the vorticity on the heat transfer performance. Therefore, in figure 50 (a), the maximum Nu_g is obtained at $S_a = 1$.

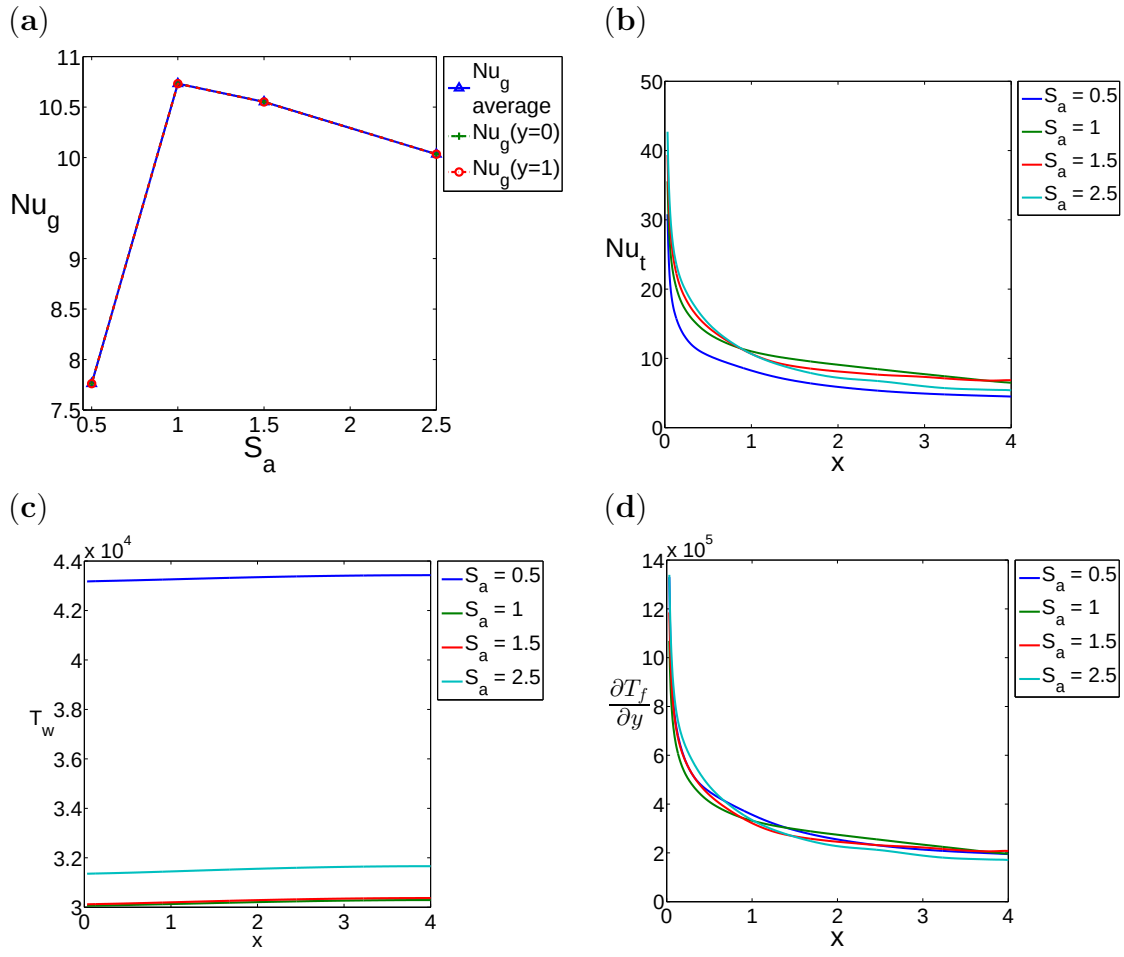

Figure 50: (a) Nu_g vs. S_a. (b) Nu_t vs. x; (c) T_w vs. x; (d) $\frac{\partial T_f}{\partial y}$ vs. x for $S_a = 0.5, 1.0, 1.5, 2.5$. Other parameters used here are $Re = 500$, $\Gamma_r = 6$, $S_b = 0.5$, $Pe_f = 500$, $Pe_s = 125$, $\gamma_{fs} = 1e-4$.

In summary, for the active vibrations, the vorticity improves the heat transfer efficiency in two aspects: it brings cooler fluids into the hotter boundary layer and maintains a high wall temperature gradient throughout the channel, and it takes out the hotter fluid in the boundary layer and lowers the wall temperature. For the parameter space that we are interested in, the effect of the vorticity on the temperature gradient is much smaller than its effect on the wall temperature. This implies that when the global Nusselt number is large, the corresponding wall temperature is small as well.

4.4.1.2 Passive Vibration Cases

Now, we consider the effect of the fluid in the passive vibration cases. For negative Γ_r, the flow is more complicated as shown in the previous analysis. The positive and negative vortex blobs exchange their positions in the channel due to the separated wall vorticity, and for different parameter sets, the flow varies from regular streets to irregular streets and to more chaotic dynamics.

We first consider the regular street cases. We show the contour plot of the temperatures at one time instant, and the corresponding vorticity contours at the same time instant in figure 51.

Similarly to the active vibration cases, the variation of the solid temperature is mainly along the x-direction. In the passive vibration cases, the vortex blobs are pushed away from the boundary layer by the separated wall vortex and move across the centerline in the channel. The vortex blobs again are able to bring cooler fluids from the center of the channel to the boundary layer and improve the mixing of the fluid in the whole channel. However, if we plot the local Nu and the wall temperature for $\Gamma = -0.6$ and compare it with values for $\Gamma = 0$ in figure 52, we realize the vorticity actually decreases the heat transfer efficiency. The wall temperature is higher for $\Gamma_r = -0.6$ as shown in figure 52 (b). The instantaneous local Nusselt number has

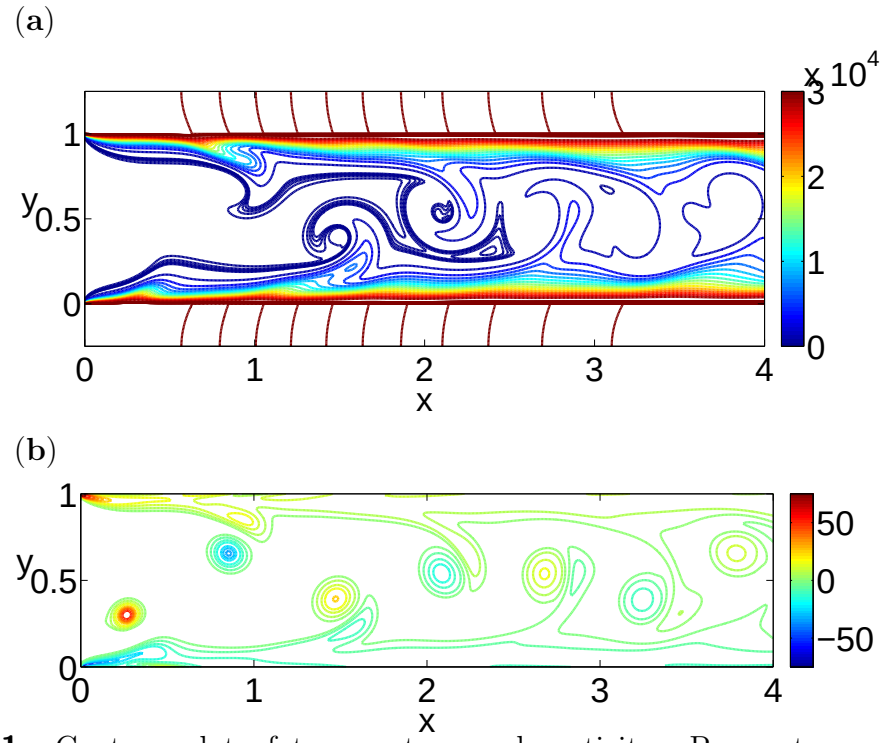

Figure 51: Contour plot of temperature and vorticity. Parameters used in this simulation are $Re = 1000$, $\Gamma_r = -0.6$, $S_b = 0.5$, $S_a = 1$, $\gamma_{fs} = 1e-4$, $Pe_f = 500$, and $Pe_s = 125$. (a) Fluid and solid temperature contour plot; (b) corresponding vorticity contour plot.

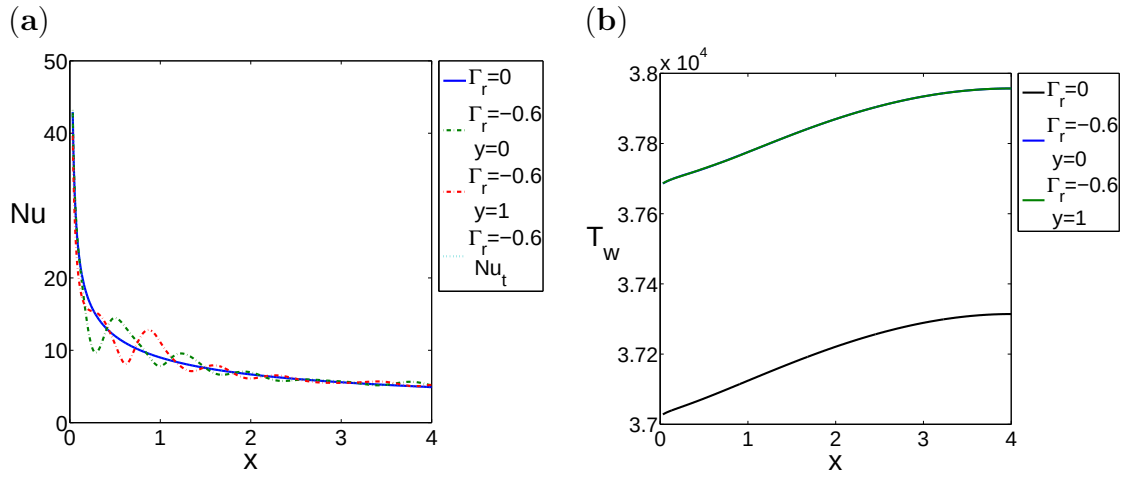

Figure 52: (a) Nu vs. x; (b) wall temperature T_w vs. x. The solid line indicates the value for $\Gamma_r = 0$, the dashed lines are for values of $\Gamma_r = -0.6$ and the dotted line denotes the time averaged value for $\Gamma_r = -0.6$. Other parameters used here are $Re = 1000$, $S_b = 0.5$, $S_a = 1$, $\gamma_{fs} = 1e-4$, $Pe_f = 500$, and $Pe_s = 125$.

large variations at the beginning of the channel which shows the effect of the vortex blob, but the variations become smaller in the channel. And the time-averaged Nu_t is almost identical to the no blob case as the dotted and the solid line collapse with each other in figure 52 (a).

To explain this phenomena, we take the positive blob as an example. The blob rotates in the counterclockwise direction and brings cooler fluid to the boundary layer along the left of its center. After the fluid is heated up by the boundary layer, it is taken away along the right of the blob's center. In the passive vibration cases, we notice that the vortex blob will generate an opposite vortex on its right lower side as shown in figure 51 (b). This negative vortex rotates clockwise and brings the heated fluid back to near wall regions, which further heats up the boundary layer. We notice that the separated vortex has more effect on the boundary layer compared to the vortex blob, but its strength is smaller. Therefore before the vortex blobs exchange their positions, they only increase the local temperature gradient by a small amount. As the vortex blobs move towards the centerline, they are further away from the boundary layer. The vortex induced forced convection does not work on the boundary layer directly and only affects it through diffusion. The boundary layer is then similar to the flat plate boundary layer solution for a unidirectional flow. For instance, in figure 51 (a), the thermal boundary layer for the lower wall in region $x \in (2, 3)$ is similar to the flat plate boundary layer solution. After the blobs exchange their positions, they function similarly to the active vibration cases. However, vortex blobs lose part of their momentum during the exchange and become much weaker with little effect on the heat transfer performance. Therefore, we can observe in figure 52 (a) that at the end of the channel, the instantaneous Nu becomes larger for $\Gamma_r = -0.6$ to a small extent.

Now we consider the effect of fluid parameters on the heat transfer efficiency in figures 53 to 56. We vary Re, Γ_r, S_b and S_a one by one and fix the other variables. In

these figures, we compare the global Nusselt number Nu_g versus different parameters in panel a. We again consider the Nu_g obtained on each wall and the averaged ones. In regular street cases, the time-averaged temperature is symmetric, and therefore these three values are essentially the same. We show the local Nu_t in panel b, the wall temperature T_w in panel c and the wall temperature gradient in panel d. In these three panels, all the value are time-averaged ones.

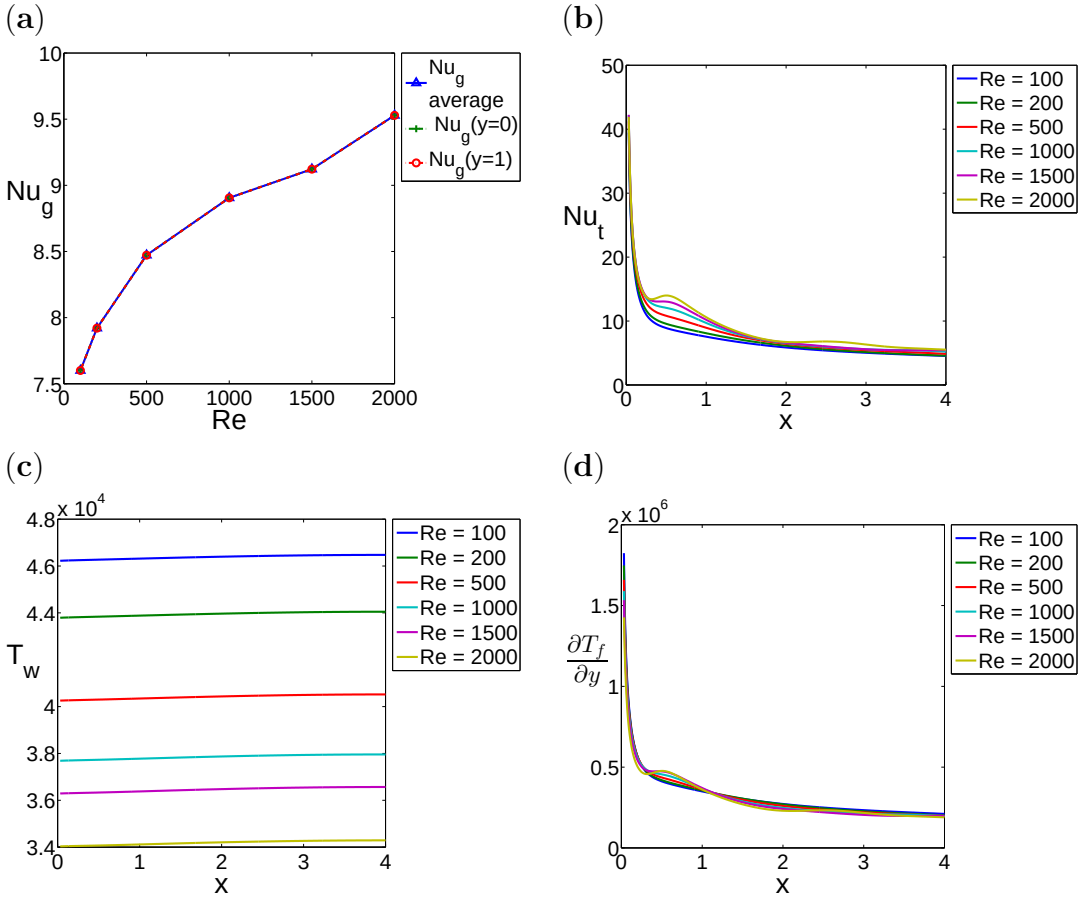

Figure 53: (a) Nu_g vs. Re. (b) Nu_t vs. x; (c) T_w vs. x; (d) $\frac{\partial T_f}{\partial y}$ vs. x for $Re = 100, 200, 500, 1000, 1500, 2000$. Other parameters used here are $\Gamma_r = -0.6$, $S_a = 1$, $S_b = 0.5$, $Pe_f = 500$, $Pe_s = 125$, $\gamma_{fs} = 1e-4$.

In figure 53, we vary the Reynolds number from 100 to 2000. As Re increases, the diffusion effect is less, and the vortex blobs as well as the separated vortices are able to maintain their strengths for longer distances in the channel and exhibit larger effects on the heat transfer performance. Therefore, the wall temperature in figure 53

(c) is smaller for larger Re as more heat is taken away by the vortex blob. In figure 53 (d), the wall temperature gradient varies much smaller than the change of the wall temperature. Thus the global Nusselt number increases with respect to Re due to the lower wall temperature.

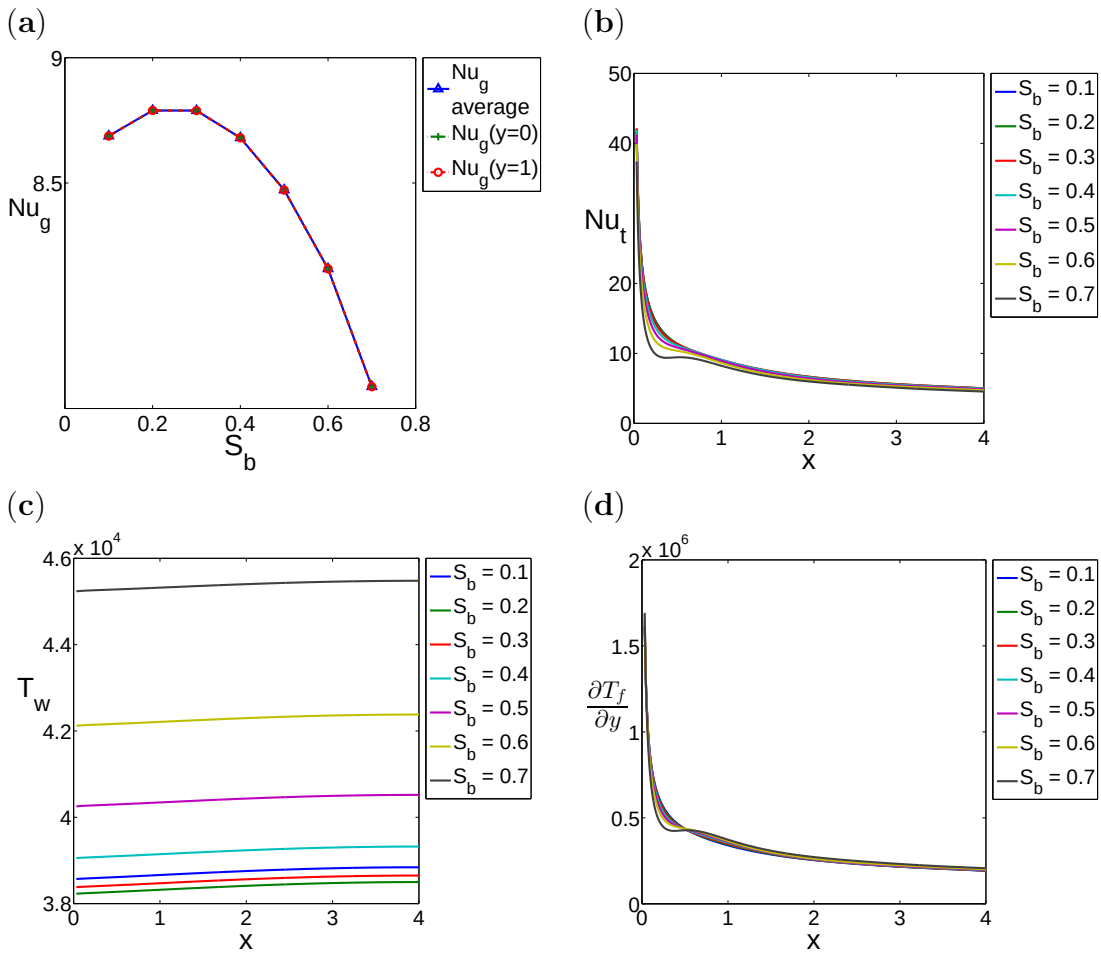

Figure 54: (a) Nu_g vs. S_b. (b) Nu_t vs. x; (c) T_w vs. x; (d) $\frac{\partial T_f}{\partial y}$ vs. x for $S_b = 0.1, 0.2, 0.3, 0.4, 0.5, 0.6, 0.7$. Other parameters used here are $Re = 500$, $\Gamma_r = -0.6$, $S_a = 1$, $Pe_f = 500$, $Pe_s = 125$, $\gamma_{fs} = 1e-4$.

In figure 54, we vary S_b and keep the other parameters fixed. From previous analysis, we know that when S_b increases, both the vortex blobs and the background flow become stronger for the passive vibration cases. Therefore, in figure 54 (d) we find that the temperature gradient is larger for as S_b increases. Even though, the change of the temperature gradient is again much smaller than the variance of the

wall temperature. Since the lowest wall temperature is obtained at $S_b = 0.2$, the maximum Nu_g is also achieved at the same point as shown in figure 54 (a).

We notice that the lower wall temperature actually corresponds to larger exchange distance X_e. This is true for both S_b and Re if we compare figures 30 with 53 (c), and figures 35 with 54 (c). We show the time instant contour plot of the temperature for $S_b = 0.2$ and $S_b = 0.7$ in figure 55. As shown in the figure, the heat is actually taken out of the boundary layer by the separated vortices as they move towards the center-line. Although this indicates a smoother thermal boundary layer which decreases the wall temperature gradient, it also helps to keep the wall temperature low. Whether the Nusselt number is improved depends on the extent that the temperature and its gradient change.

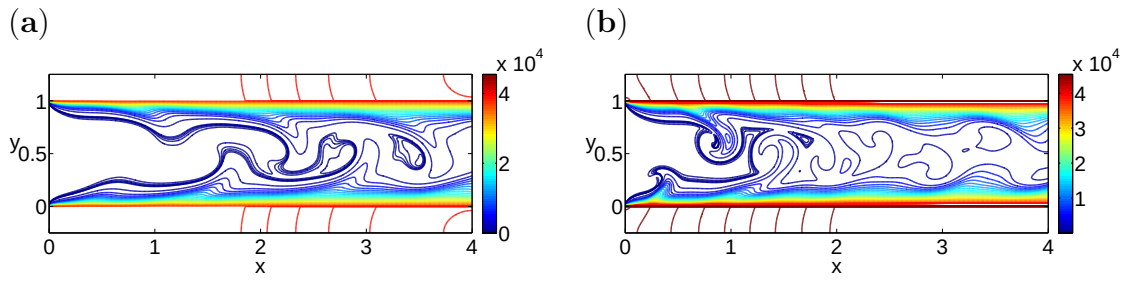

Figure 55: Time instant contour plot of the temperature for (a) $S_b = 0.2$; (b) $S_b = 0.7$. Other parameters used here are $Re = 500$, $\Gamma_r = -0.6$, $S_a = 1$, $Pe_f = 500$, $Pe_s = 125$, $\gamma_{fs} = 1e-4$.

Now we vary S_a and fix the other parameters in figure 56. According to previous analysis, as S_a increases, both the vortex blobs' strength and the background flow decreases rapidly. U_b decreases to 1 in the speed of S_a^{-2} as the $\tanh(x) \sim x$ when $x \to 0$. And there exists less number of vortex blobs in the channel as S_a increases which further decreases the effect of the vorticity. Therefore, Nu_g decreases with S_a as the background flow is smaller.

Finally, we vary Γ_r and keep the other parameters unchanged in figure 57. As Γ_r becomes more negative, the vortex blobs' strength and the background flow are both larger. From $\Gamma_r = 0$ to -0.3, the vortex blobs are weak and diffuse quickly

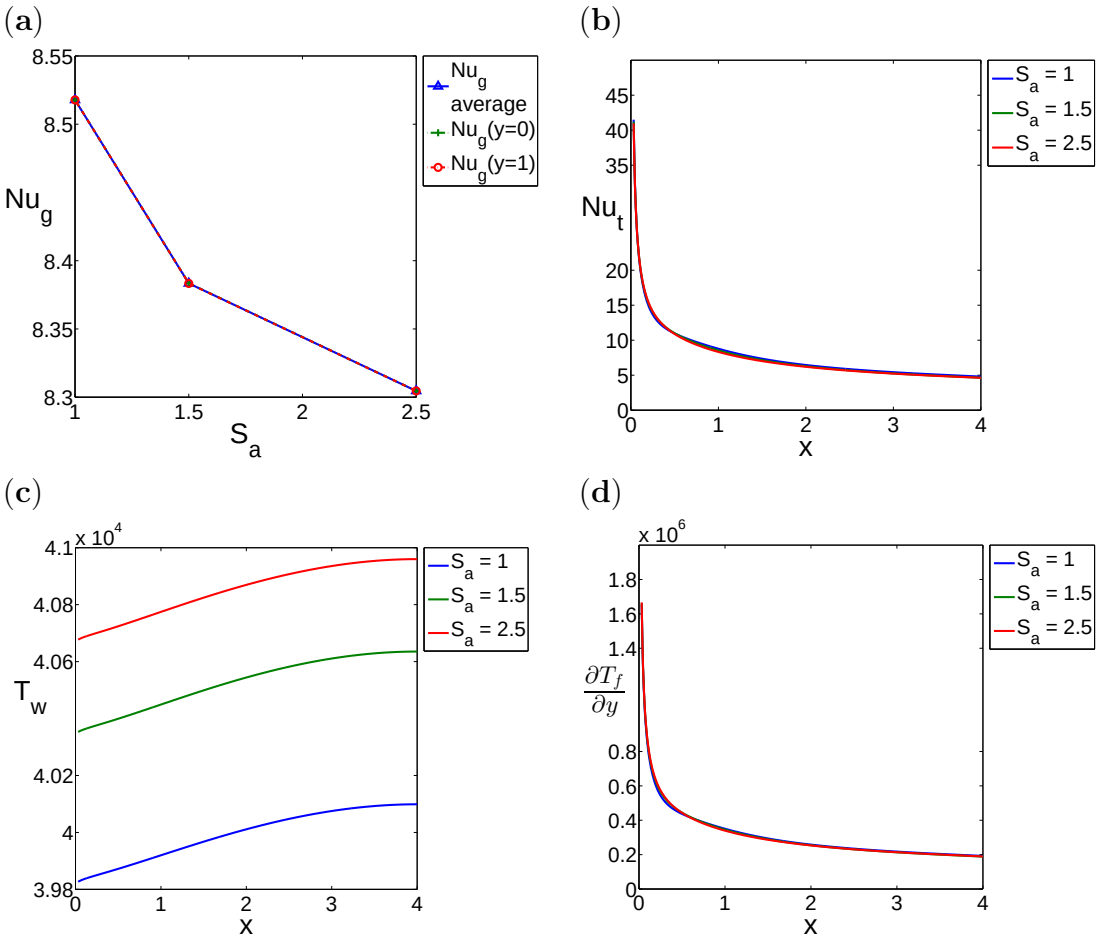

Figure 56: (a) Nu_g vs. S_a. (b) Nu_t vs. x; (c) T_w vs. x; (d) $\frac{\partial T_f}{\partial y}$ vs. x for $S_a = 1, 1.5, 2.5$. Other parameters used here are $Re = 500$, $\Gamma_r = -0.45$, $S_b = 0.5$, $Pe_f = 500$, $Pe_s = 125$, $\gamma_{fs} = 1e-4$.

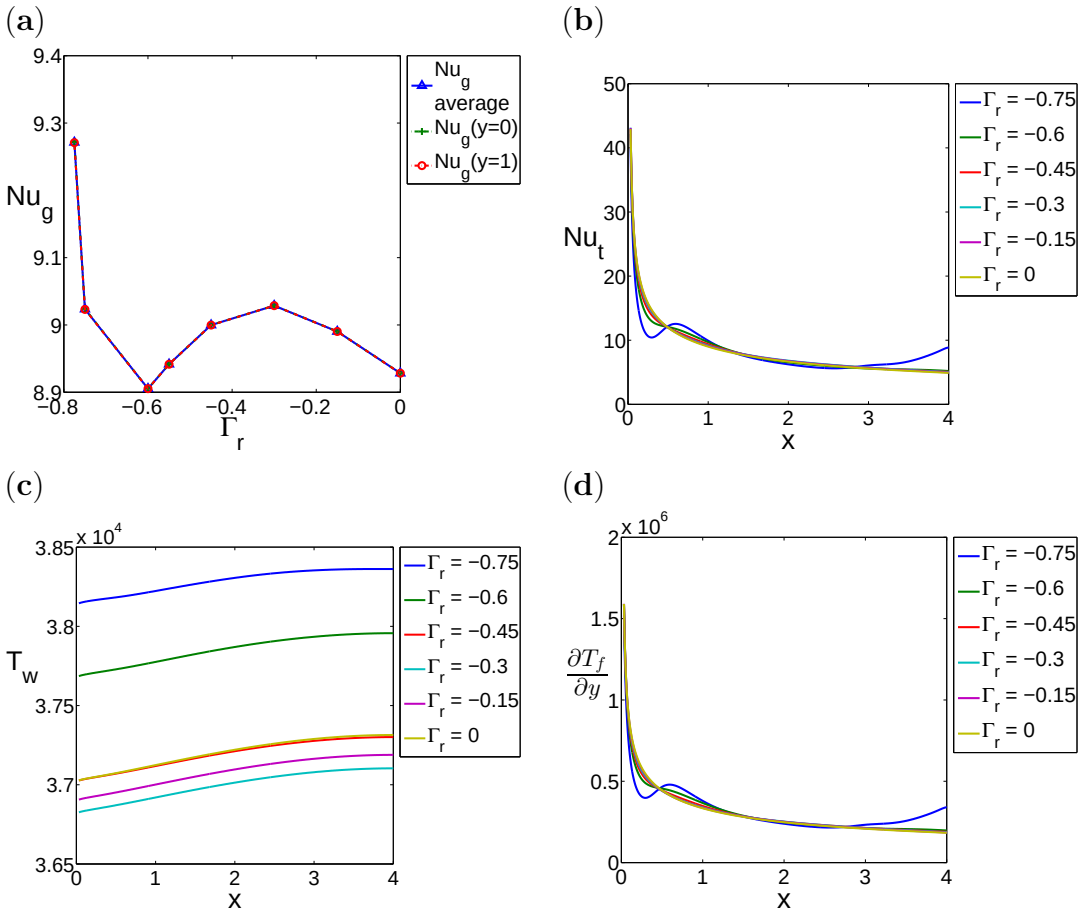

Figure 57: (a) Nu_g vs. Γ_r. (b) Nu_t vs. x; (c) T_w vs. x; (d) $\dfrac{\partial T_f}{\partial y}$ vs. x for $\Gamma_r = 0, -0.15, -0.3, -0.45, -0.6$. Other parameters used here are $Re = 1000$, $S_a = 1$, $S_b = 0.5$, $Pe_f = 500$, $Pe_s = 125$, $\gamma_{fs} = 1e-4$.

in the channel. The thermal boundary layer is close to the one due to a Poiseuille flow. Nu_g only depends on the strength of the background flow. When Γ_r becomes more negative, the behavior of the vortex blobs is similar to what we describe in the cases with Re and S_b varied. The variance of the temperature gradient is small and the Nusselt number mainly depends on the wall temperature. Therefore, the exchange distance X_e decreases as Γ_r becomes more negative, which leads to a larger wall temperature and smaller Nu_g. When Γ_r is -0.75, we notice that the temperature gradient increases at the end of the channel in figure 57 (d). In this case, the blobs are strong enough that they are still able to maintain strength after the exchange and behave as in the active vibration cases. Therefore, although the wall temperature is still larger in this case as shown in figure 57 (c), the local Nusselt number increases due to the large change of the temperature gradient.

As Γ_r becomes more negative, the streets become irregular. We show Nu_g versus Γ_r in figure 58. Since the velocity is asymmetric, the temperature becomes asymmetric as well and we can see the different Nu_g for each wall.

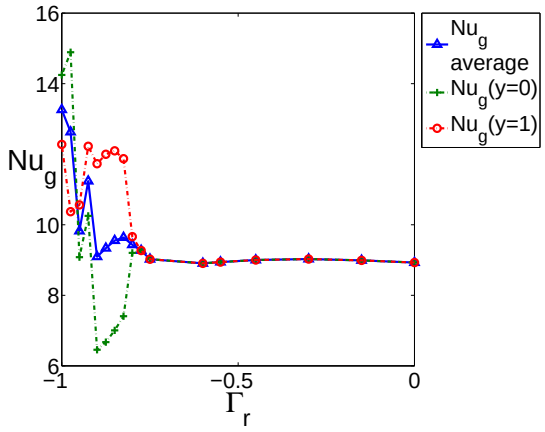

Figure 58: Nu_g vs. Γ_r. Other parameters used here are $Re = 1000$, $S_a = 1$, $S_b = 0.5$, $Pe_f = 500$, $Pe_s = 125$, $\gamma_{fs} = 1e-4$.

We plot the contour of time-averaged vorticity $\overline{\omega}$ corresponding to the turning points of figure 58 ($\Gamma_r = -0.8, -0.875, -0.925, -0.95, -0.975, -1$) in figure 59. And

we show the corresponding time-averaged temperature profile in figure 60.

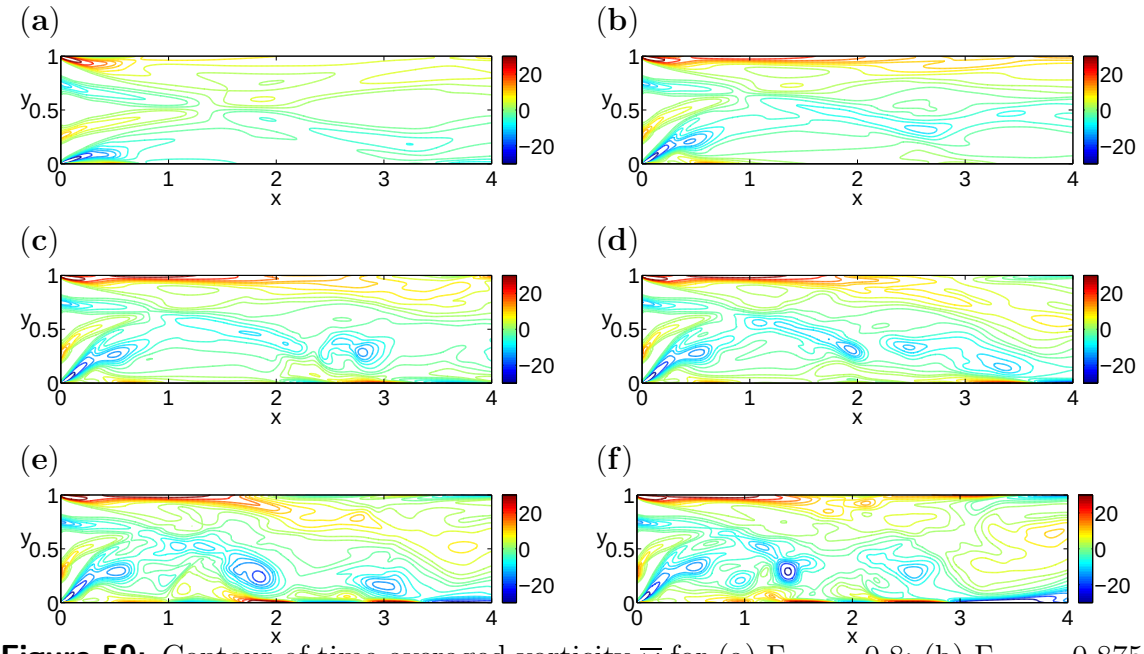

Figure 59: Contour of time-averaged vorticity $\overline{\omega}$ for (a) $\Gamma_r = -0.8$; (b) $\Gamma_r = -0.875$; (c) $\Gamma_r = -0.925$; (d) $\Gamma_r = -0.95$; (e) $\Gamma_r = -0.975$; (f) $\Gamma_r = -1$. Other parameters are $Re = 1000$, $S_a = 1$ and $S_b = 0.5$.

As the flow becomes irregular, it first shifts the symmetric $\overline{\omega}$ to asymmetric ones as shown in figure 59. During this process, the flow is compressed along one side of the channel (the upper wall in figure 59). The wall temperature is thus lower along this side and the temperature gradient is larger. The thermal boundary layer is thinner, which leads to a larger Nusselt number. For the same reason, the Nusselt number becomes smaller along the other wall. This can be observed in figure 58 for $\Gamma_r = -0.8$ and $\Gamma_r = -0.825$. As Γ_r becomes more negative, an extra negative vortex blob is observed in the middle of the channel at $x \approx 2.8$ in figure 59. The extra vortex blob is located on the lower half of the channel and behaves similarly to the active vibration cases which helps to improve the Nusselt number on the lower wall. Nu_g thus increases rapidly from $\Gamma_r = -0.925$ to more negative values. But we note that this observation is based on time-averaged vorticity value, and the time instant values is more chaotic. As Γ_r becomes more negative, the flow is more complicated, and there is hardly any pattern even for the time-averaged values, and the Nu_g varies

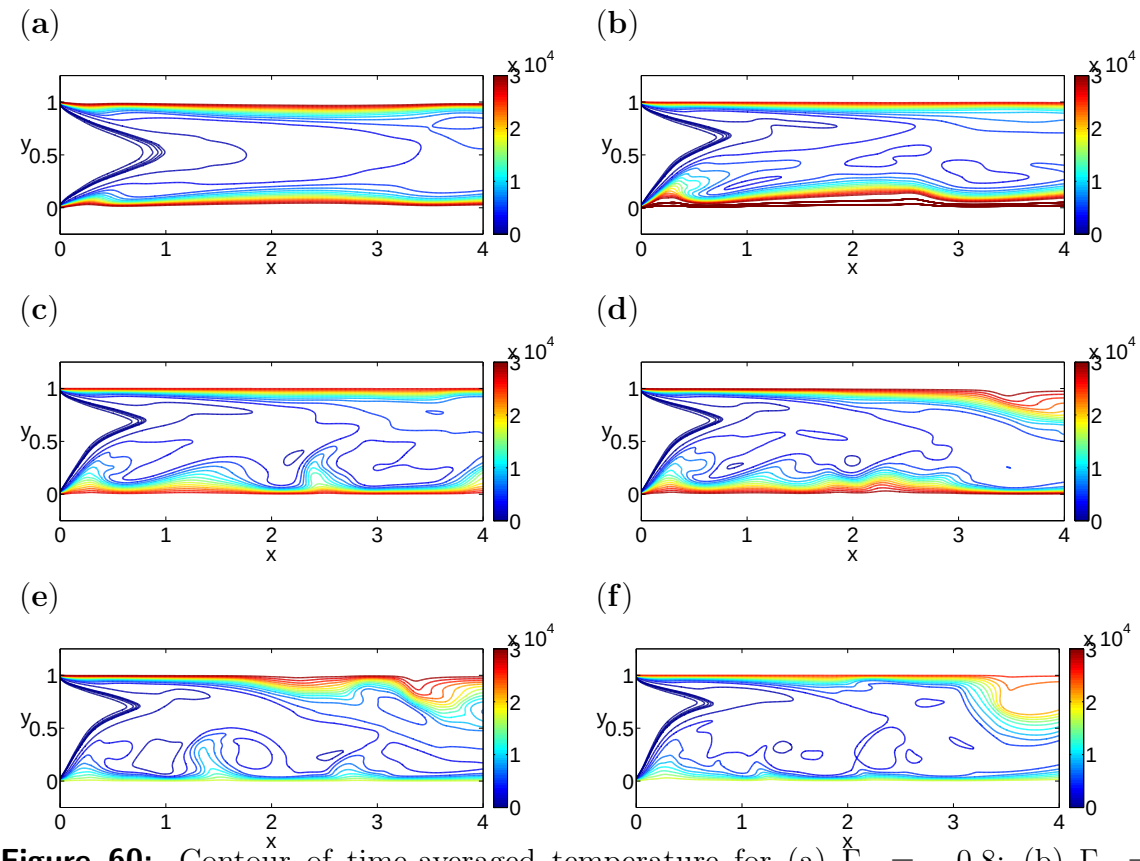

Figure 60: Contour of time-averaged temperature for (a) $\Gamma_r = -0.8$; (b) $\Gamma_r = -0.875$; (c) $\Gamma_r = -0.925$; (d) $\Gamma_r = -0.95$; (e) $\Gamma_r = -0.975$; (f) $\Gamma_r = -1$. Other parameters are $Re = 1000$, $S_a = 1$ and $S_b = 0.5$, $Pe_f = 500$, $Pe_s = 125$, $\gamma_{fs} = 1e-4$.

rapidly up and down.

The largest Nu_g is obtained at $\Gamma_r = -1$ which seems to indicate that the more complicated irregular flow leads to better a heat transfer performance, but when $\Gamma_r = -0.95$, we notice that the Nu_g decreases rapidly as well, which indicates that the behavior of Nu_g is unpredictable in the passive vibration cases. In this sense, the active vibration is better than the passive vibration in improving the heat transfer efficiency as its behavior is predictable and easier to control. And we notice that we can obtain a Nu_g as large as that corresponding to the complicated irregular streets with the active vibration. We show the value of Nu_g varying with Γ_r across the active and passive vibration cases in figure 61. For simplicity, we only plot the averaged Nu_g of the two walls in the figure.

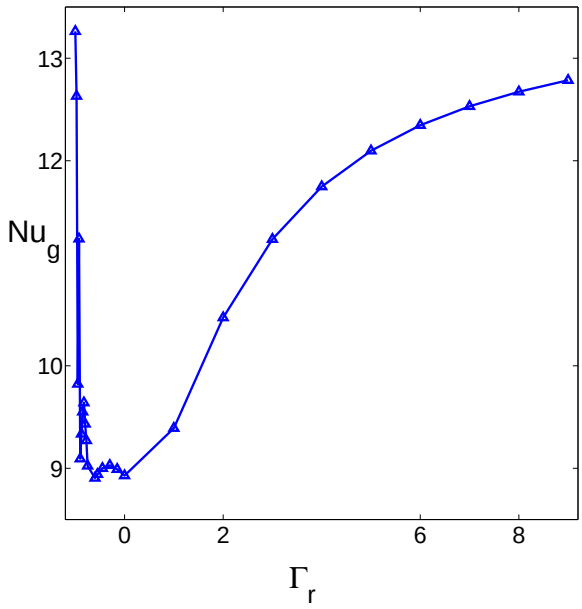

Figure 61: Nu_g vs. Γ_r for both active and passive vibrations. The other parameters are $Re = 1000$, $S_a = 1$ and $S_b = 0.5$, $Pe_f = 500$, $Pe_s = 125$, $\gamma_{fs} = 1e-4$.

More importantly, in the active vibration cases, the temperature is symmetric which means the heat transfer performance is the same along different walls. This is an important property since the design of an actual heat sink is base on its worst performance. In other words, if the passive vibration is applied to enhance the heat

transfer efficiency, then the wall with the lower Nusselt number should be used for measurement. Therefore, we believe that the active vibration is more useful for enhancing the heat transfer efficiency in the channel flow.

4.4.2 Temperature Parameters

In this section, we discuss the effect of the temperature parameters Pe_f, Pe_s and γ_{fs} on the heat transfer performance. In fact, changing the thermal conductivity of either the fluids or the solids is a common way to enhance the heat transfer. For example, there are many previous studies about using nano-particles to increase the Péclet number of the fluids and thus enhance the heat transfer [17, 18, 79]. Some other work focused on changing the shape or the thermal property of the solids to improve the heat transfer efficiency [45, 15].

Now we fix all the fluid parameters and vary the thermal parameters in figure 62. We note that the three dimensionless parameters Pe_f, Pe_s and γ_{fs} are actually related to each other. The Péclet number which is defined as $Pe = \dfrac{HU}{\alpha}$, depends on the thermal diffusivity α, and $\alpha = \dfrac{\kappa}{\rho C_p}$ depends on the thermal conductivity κ with ρ and C_p are corresponding density and specific heat capacity. Therefore, $\gamma_{fs} = \dfrac{\kappa_f}{\kappa_s}$ is related to Pe_f and Pe_s. To simplify the problem, we assume that ρ and C_p are fixed, and α varies with κ accordingly, for the reason that variation of κ is generally much larger than the change of ρC_p for most materials. Salazar [58] showed the thermal diffusivity versus conductivity for a wide variety of homogeneous materials from gas to condensed matter and the figure is close to a straight line which indicates the change of α mainly depends on the change of κ. This assumption reduces the thermal parameters to Pe_f and Pe_s.

The effects of the thermal parameters are more obvious than those of the fluid parameters. When Pe_f is larger, the convection term in the fluid temperature equation is enhanced and the effect of the vortex blob is more obvious. Therefore, in figure 62

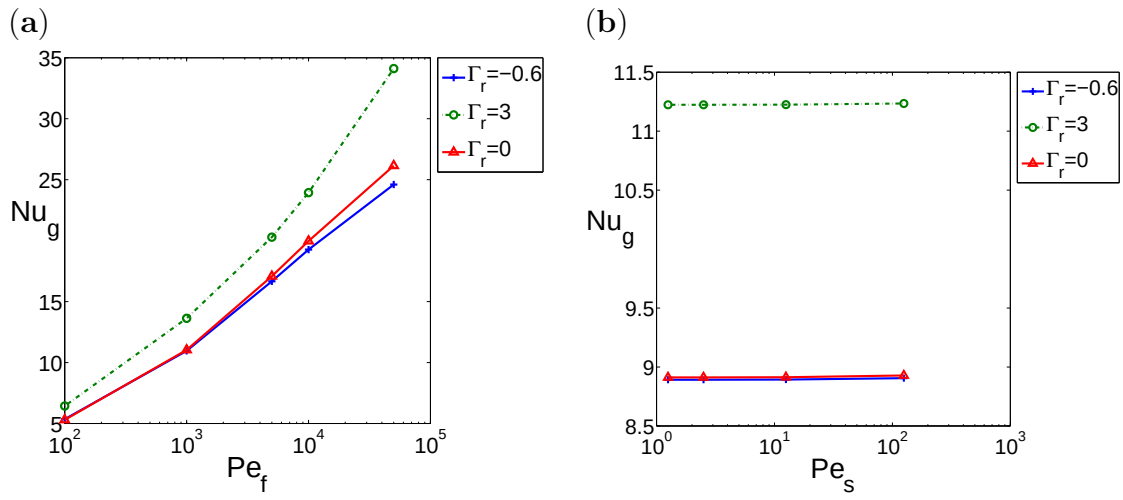

Figure 62: (a) Nu_g vs. Pe_f for $\Gamma_r = 0, 3, -0.6$, $Pe_s = 125$; (b) Nu_g vs. Pe_s for $\Gamma_r = 0, 3, -0.6$, $Pe_f = 500$, other parameters are $Re = 1000$, $S_a = 1.0$ and $S_b = 0.5$.

(a), as Pe_f increases, the Nu_g changes to a larger extent for active vibration cases than for $\Gamma_r = 0$. When $\Gamma_r = -0.6$, the Nu_g actually decreases compared to $\Gamma_r = 0$ due to the vortex blob, and with larger Pe_f, the decrease is more obvious. On the other hand, Pe_s has a much smaller effect as shown in figure 62 (b). This is expected as in the heat equation Pe_s mainly determines the rate of the diffusion. It affects the Nu_g number only through the interface equation.

In general, increasing the fluid Péclet number is an effective way of enhancing the heat transfer, but it is not a simple task to do so. Most cooling materials, like air or water, have little variances on thermal conductivity, and the choice of characteristic length L and U is limited by the fact that the flow requires a decent Re to stay laminar. On the other hand, we notice that in figure 62 (a) when Pe_f increases from 5000 to 10000 and $\Gamma_r = 0$, the increase of Nu_g can be easily achieved by simply varying the fluid parameters Γ_r from 0 to 3 with the same $Pe_f = 5000$. And the Nusselt number obtained with $\Gamma_r = 0$ and $Pe_f = 50000$ is the almost same as that obtained with $\Gamma_r = 3$ and $Pe_f = 10000$.

This shows the significant role of the vorticity in the heat transfer enhancement and confirms the importance of our studies.

4.5 Optimization Problem

We have shown the improvement of the heat transfer efficiency by vorticity in previous sections. A more practical aspect to consider the problem is to define some type of energy and look for the best heat transfer performance under the same amount of energy.

First, we need to propose an appropriate measurement for the energy. For active vibration cases, energy is required to generate the background flow and vibrate the flat plate. For passive vibration cases, the vibration is generated through the fluid-solid interactions and does not require extra power. However, forces are still required to counteract the drag generated by the vibration and keep the object in a fixed position. Therefore, for both cases, we define the kinetic energy flux of the incoming flow as a measurement of the input energy.

The kinetic energy flux is defined as:

$$\langle KE_{flux} \rangle = \int_0^{\tau_p} \int_0^H \frac{1}{2} \rho_f \|\mathbf{u}\|^2 \cdot u \, dydt \tag{77}$$

which measures the amount of the kinetic energy of the incoming flow into the channel over one period. Since the velocity of the vortex blob U is constant as equation (32), we can rewrite the time variable with spatial variable as:

$$\langle KE_{flux} \rangle = \frac{1}{U} \int_0^a \int_0^H \frac{1}{2} \rho_f \|\mathbf{u}\|^2 u \, dydx \tag{78}$$

We define the velocity for the incoming flow with background flow $U_b = 0$ and the blob's strength $\Gamma = 1$ to be u_{blob} and v_{blob} which is obtained by equation (21). Then any incoming flow with arbitrary U_b and Γ can be written as

$$u = U_b(1 + \Gamma_r u_{blob}), \; v = U_b(\Gamma_r v_{blob}) \tag{79}$$

where $\Gamma_r = \dfrac{\Gamma}{U_b H}$, and u_{blob} and v_{blob} are functions of dimensionless number S_a and S_b. And the velocity of the vortex blob is

$$U_c = U_b(1 + \Gamma_r u_c) \tag{80}$$

where u_c is obtained by equation (32). Therefore, the kinetic energy flux can be written as

$$\langle KE_{flux} \rangle = \frac{\rho_f}{2} \frac{1}{U_c} \int_0^a \int_0^H (u^2 + v^2) u \, dydx \tag{81}$$

If we nondimensionalize the length by H and the velocity by some characteristic velocity U which will be described later, then we obtain

$$\langle KE_{flux} \rangle = (\rho_f U^2 H^2) \frac{1}{2} \frac{1}{U_c} \int_0^{S_a} \int_0^1 (u^2 + v^2) u \, dydx \tag{82}$$

Note that U_c, u, v, x and y are all dimensionless variables, and we just keep the same notations for simplicity. Now if we define the characteristic velocity U in the following way:

$$U = \sqrt{\frac{\langle KE_{flux} \rangle}{\rho_f H^2}} \tag{83}$$

then the dimensionless kinetic energy will always be 1 and satisfy the following equation:

$$\begin{aligned} 1 &= \frac{1}{2} \frac{1}{U_c} \int_0^{S_a} \int_0^1 (u^2 + v^2) u \, dydx \\ &= \frac{1}{2} \frac{1}{U_b (1 + \Gamma_r u_c)} \int_0^{S_a} \int_0^1 U_b^3 ((1 + \Gamma_r u_{blob})^2 + \Gamma_r^2 v_{blob}^2)(1 + \Gamma_r u_{blob}) \, dydx \\ &= \frac{1}{2} U_b^2 \int_0^{S_a} \int_0^1 \frac{(1 + 2\Gamma_r u_{blob} + \Gamma_r^2 u_{blob}^2 + \Gamma_r^2 v_{blob}^2)(1 + \Gamma_r u_{blob})}{1 + \Gamma_r u_c} \, dydx \end{aligned} \tag{84}$$

Therefore, given $\langle KE_{flux} \rangle$ and a parameter set $\{\Gamma_r, S_a, S_b\}$, we are able to calculate the corresponding U_b and Γ.

This nondimensionalization is different from the one that we applied in previous chapters. In previous chapters, we nondimensionalized the problem based on the velocity of the vortex blob U_c. Therefore, for different parameter sets, the problem has the same time period. Here, we fix the kinetic energy flux and the U defined by equation (83), and the vortex blob therefore has different velocities for different parameter sets. In figure 63, we plot U_c versus Γ_r and corresponding U_b versus Γ for fixed kinetic energy flux. For a given kinetic energy flux, the input energy is now

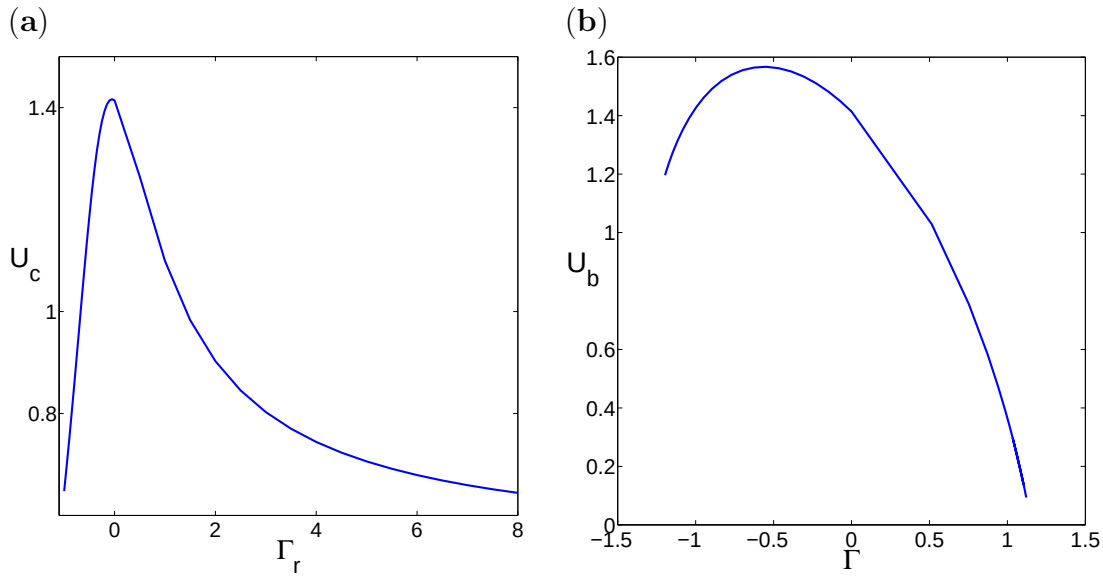

Figure 63: (a) Velocity of the vortex blob U_c vs. Γ_r for fixed kinetic energy flux. (b) Background flow U_b vs. blob strength Γ for fixed kinetic energy flux. Other parameters are $S_a = 1$ and $S_b = 0.5$.

allocated between generating the background flow and the vortex blob based on Γ_r.

Now for fixed input energy $\langle KE_{flux} \rangle$, we consider the following optimization problem:

$$\min \max\{T_s : 0 \leq t \leq \tau_p\} \tag{85}$$

Many electronic devices have a tolerance temperature and once the temperature of the device is higher than the tolerance temperature, it malfunctiones. The maximum solid temperature over one period indicates the largest temperature a device can achieve. Therefore, we look for the parameter sets that provide the minimum value among the maximum temperatures.

In figure 64, we plot $\max\{T_s : 0 \leq t \leq \tau_p\}$ versus Γ_r.

It turns out that the minimum value is obtained with the largest Γ_r. In fact, Γ_r can be $+\infty$ when the background flow $U_b = 0$. And the incoming flow velocity is then:

$$u = \Gamma u_{blob}, \quad v = \Gamma v_{blob} \tag{86}$$

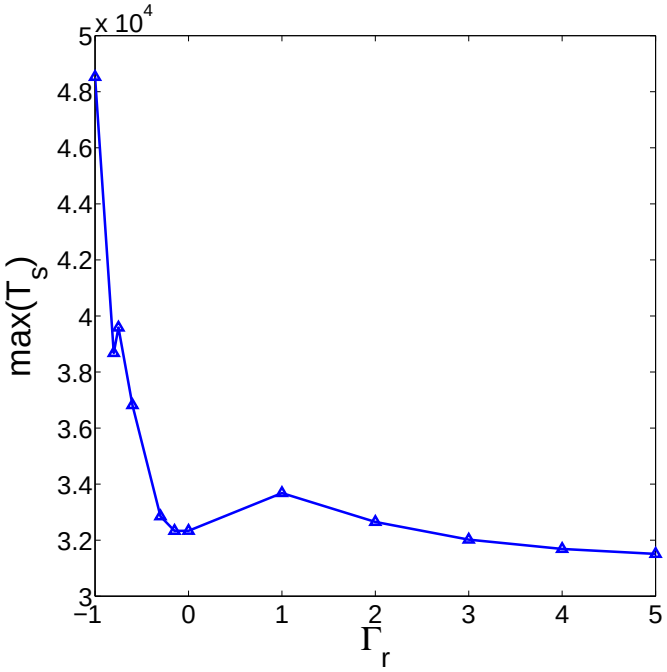

Figure 64: $\max\{T_s : 0 \leq t \leq \tau_p\}$ vs. Γ_r. Other parameters used here are $Re = 1000$, $S_b = 0.5$, $S_a = 1$, $Pe_f = 500$, $Pe_s = 125$, $\gamma_{fs} = 1e-4$.

The vortex blob has as velocity $U_c = \Gamma u_c$, and the dimensionless kinetic energy flux satisfies

$$\frac{\Gamma^2}{2} \int_0^{S_a} \int_0^1 \frac{(u_{blob}^2 + v_{blob}^2) u_{blob}}{u_c} \, dydx = 1 \tag{87}$$

and therefore we can solve for the optimal Γ with any given S_a and S_b.

In reality, when the vortex wake is generated in the flow by a generator, Γ, S_a and S_b are related to each other and we do not have the freedom to choose Γ as it is in equation (87). Nevertheless, our model can be applied to any vortex generator as long as its generated wake is modelled by a von Kármán street. It is possible that in future there are certain types of vortex generators satisfying the requirement of our model. And our work is useful as a guidance for the design of both the vortex generator and a more efficient heat sink.

CHAPTER V

CONCLUSION

In this work, we have numerically studied the effect of the vorticity on the enhancement of heat transfer in a channel flow. We develop models to simulate both the fluid dynamixcs and the heat transfer process. Instead of modelling the actual vortex generator, we approximate the wake of the vortex generators and apply it as inflow boundary conditions based on the idea of vortex blob methods and the well-known von Kármán vortex street. This approximation not only allows us to explore a larger parameter space of $\{Re, \Gamma_r, S_b, S_a\}$ and further understand the vortex dynamics of the channel flows, but also provides a natural classification of different flows based on the sign of Γ_r.

The flow exhibits different properties depending on the values of four dimensionless parameters. Among them, the Reynolds number determines the diffusion rate of the vortex blob. Γ_r provides a ratio between the strength of the vortex blob and the background flow speed. S_a and S_b define the geometric characteristics of the vortex street and also change the strength of the vortex blob and the speed of the background flow.

We define the flows with positive Γ_r as the active vibration cases. In the active vibration cases, we find that vortex blobs are able to maintain the same spatial structures as the inflow and mainly move in the downstream direction. These properties hold for all parameters as long as Γ_r is positive, and different parameters determine the flows without changing its street structures. As a consequence, the corresponding heat transfer processes also exhibit similar structures with different parameters. In the active vibration cases, we find that the vortex blob improves the heat transfer by

disrupting the thermal boundary layer and preventing the decay of the wall temperature gradient throughout the channel, and by enhancing the forced convection to cool down the wall temperature. In general, the flow with larger vortex blobs' strengths and stronger background flow and the vorticity that is closer to the wall and diffuses more slowly will result in a better heat transfer performance.

We define the flows with negative Γ_r as the passive vibration cases. We find that the vortex blobs move towards the centerline and exchange their positions in the channel. This "criss-cross" motion is due to the interactions between the blobs and the separated vortices from the wall. And the location where the inversion happens also depends on the strength of this interaction, as well as the momentum of the vortex blobs and the vertical spaces S_b.

In passive vibration cases, different parameters lead to totally different flow profiles. Based on the flow's spatial and temporal properties, we further classify it as a regular, irregular or non-periodic street. The flow of the regular street cases has symmetric time-averaged vorticity while it is asymmetric in the irregular street cases. The transition happens as the separated vortices become strong enough that the interactions between separated vortices are comparable to those between the blob and the wall separations. The spatial structure is then destroyed and the flow becomes irregular. We obtain diagrams of the flow type depending on parameter sets $\{Re, \Gamma_r, S_b, S_a\}$. In general, as Re increases, Γ_r tends to more negative, S_a becomes smaller and S_b becomes larger, the flow varies from regular to irregular and to non-periodic street cases.

The corresponding heat transfer process is complicated and varies dramatically as the flow changes its properties. In the regular street cases, when the vortex blobs are weak and not able to cross the centerline in the channel, the thermal boundary layer is similar to a flat plate solution and the performance of the heat sink only depends on the speed of the background flow. When the vortex blobs have moderate

strengths, the separated vortex has more effect on the boundary layer compared to the vortex blob. But their strength is much smaller compared to the vortex blob. Therefore temperature gradient only changes by a small amount. As the vortex blobs move away from the boundary layer, they are able to take the heat out of the thermal boundary layer and thus cools down the wall temperature. The heat transfer efficiency therefore depends on the exchange distance X_e and larger X_e leads to a better performance. If the strength of the vortex blobs is considerably strong after the inversion, they behave similarly to the blobs in the active vibration cases and improve the heat transfer performance. The heat transfer efficiency then depends on the strength of the vortex blobs.

In the irregular street cases, the flow varies rapidly and loses most of its spatial structure. The Nusselt number changes rapidly as well and the effect of the fluid parameters on the Nusselt number is unpredictable. The asymmetric properties lead to different heat transfer performances at the two walls.

Compared to the fluid parameters, we find that the thermal parameters of solids have much less effect on the heat transfer enhancement. The thermal properties of the fluid play an important role in determining the amount of heat transfer by convection and by conduction. The Nusselt number can be largely improved by increasing the Péclet number of the fluid, which turns out to be a challenging task. We realize that we can achieve the same heat transfer performance by simply adding vortices in the incoming flow, and this is an important results of our current work.

Finally, we propose a more realistic optimization problem which is to minimize the maximum temperature of the solids with a given input energy. Kinetic energy flux of the incoming flow is applied as a measurement for the input energy. We find that the best heat transfer performance is obtained in the active vibration case with zero background flow.

APPENDIX A

CONVERGENCE STUDY

A.1 Convergence Study for Fluid Solver

In this section, we display the results of convergence tests with respect to dt and dx for the fluid solver. For a smooth problem, second order convergence is expected for both time and spatial variables. For all the numerical results obtained here, we use the following dimensionless parameters: the length of the channel $L = 4$, the height of the channel $H = 1$, $S_a = 1$ and $S_b = 0.5$. We choose the relative vortex strength $\Gamma_r = 1$ for the active vibration and $\Gamma_r = -0.5$ for the passive vibration. In Navier-Stokes solutions, there is usually a boundary layer of thickness $\delta \sim Re^{-1/2}$ adjacent to a no-slip boundary, within which there are potentially large velocity and vorticity gradients. For accurate results it is necessary to choose a mesh spacing which resolves the boundary layer. Therefore, we take $Re = 500$ in convergence studies so that even for the coarsest grid where $dx = 1/64$, the boundary layer solution is resolved.

A.1.1 dx-Convergence

In Tables 2 and 3, we show the convergence results for spatial variables by comparing the value of ω obtained at certain locations and a fixed time instant $t = 6\tau_p$ where τ_p is the time period. These locations include interior points at the center line of the channel $(x, y) = (2, 0.5)$ and near one of the vortex blobs $(x, y) = (2, 0.25)$, and the boundary point at $(x, y) = (4, 0.5)$. Tables 2 and 3 show the results for the active vibration and passive vibration respectively. The ratio is calculated by the following formula:

$$Ratio = \frac{|\omega(dx) - \omega(\frac{dx}{2})|}{|\omega(\frac{dx}{2}) - \omega(\frac{dx}{4})|}$$

Table 2: dx-convergence in ω for active vibration

	(x,y)=(2,0.5)			(x,y)=(2,0.25)		
dx	$\omega(x,y)$	$\lvert\omega(dx)-\omega(\frac{dx}{2})\rvert$	Ratio	$\omega(x,y)$	$\lvert\omega(dx)-\omega(\frac{dx}{2})\rvert$	Ratio
2^{-6}	6.022e-3	2.196e-3	2.8	-2.966	3.124e-3	2.5
2^{-7}	8.218e-3	7.759e-4	3.5	-2.969	1.237e-3	2.3
2^{-8}	8.994e-3	2.248e-4	-	-2.970	5.289e-4	-
2^{-9}	9.219e-3	-	-	-2.970	-	-
	(x,y)=(4,0.5)					
2^{-6}	5.326e-2	8.167e-3	4.5			
2^{-7}	4.509e-2	1.830e-3	1.4			
2^{-8}	4.326e-2	1.292e-3	-			
2^{-9}	4.197e-2	-	-			

Table 3: dx-convergence in ω for passive vibration

	(x,y)=(2,0.5)			(x,y)=(2,0.25)		
dx	$\omega(x,y)$	$\lvert\omega(dx)-\omega(\frac{dx}{2})\rvert$	Ratio	$\omega(x,y)$	$\lvert\omega(dx)-\omega(\frac{dx}{2})\rvert$	Ratio
2^{-6}	-3.269	0.940	1.8	-0.355	0.119	2.6
2^{-7}	-4.209	0.537	2.4	-0.236	4.523e-2	2.8
2^{-8}	-4.746	0.225	-	-0.191	1.627e-2	-
2^{-9}	-4.971	-	-	-0.175	-	-
	(x,y)=(4,0.5)					
2^{-6}	1.493	0.511	1.3			
2^{-7}	0.982	0.395	6.5			
2^{-8}	0.586	6.069e-2	-			
2^{-9}	0.526	-	-			

and it should be 4 when second order convergence is achieved.

As shown in Tables 2 and 3, only first order convergence is achieved. This is mainly caused by the leading edge singularity due to the violation of no-slip and no-penetration condition of the inflow condition. To show this, we consider a smooth problem where the inflow condition is given by a Poiseuille flow according to equation (40). This problem eventually becomes a steady problem and the value of the velocity only varies along the y-direction. We show the steady state solutions obtained at several locations in Table 4 and a second order convergence is achieved.

Table 4: dx-convergence in ω for Poiseuille inflow

	(x,y)=(2,0.5)			(x,y)=(2,0.25)		
dx	$\omega(x,y)$	$\lvert\omega(dx)-\omega(\frac{dx}{2})\rvert$	Ratio	$\omega(x,y)$	$\lvert\omega(dx)-\omega(\frac{dx}{2})\rvert$	Ratio
2^{-6}	-1.831e-2	2.353e-4	3.9	-3.972	1.685e-4	3.9
2^{-7}	-1.807e-2	6.086e-5	4.1	-3.97208	4.270e-5	4.1
2^{-8}	-1.801e-2	1.494e-5	-	-3.97204	1.050e-5	-
2^{-9}	-1.799e-2	-	-	-3.97203	-	-

Table 5: dt-convergence in ω for active vibration

	(x,y)=(2,0.5)			(x,y)=(2,0.25)		
dt	$\omega(x,y)$	$\lvert\omega(dt)-\omega(\frac{dt}{2})\rvert$	Ratio	$\omega(x,y)$	$\lvert\omega(dt)-\omega(\frac{dt}{2})\rvert$	Ratio
2^{-6}	5.762e-3	2.458e-3	3.6	-3.027	5.341e-2	7.0
2^{-7}	8.218e-3	6.805e-4	5.4	-2.974	7.706e-3	3.1
2^{-8}	8.994e-3	1.264e-4	-	-2.966	2.451e-4	-
2^{-9}	9.025e-3	-	-	-2.963	-	-
	(x,y)=(4,0.5)					
2^{-6}	2.952e-2	1.556e-2	2.4			
2^{-7}	4.509e-2	6.567e-3	2.2			
2^{-8}	5.166e-2	2.977e-3	-			
2^{-9}	5.464e-2	-	-			

A.1.2 dt-Convergence

In Tables 5 and 6, we show the convergence results for time variables again by comparing the value of ω obtained at certain locations and the fixed time instant $t = 6\tau_p$. Tables 5 and 6 show the results for the active vibration and passive vibration respectively. The ratio is calculated by the following formula:

$$Ratio = \frac{|\omega(dt) - \omega(\frac{dt}{2})|}{|\omega(\frac{dt}{2}) - \omega(\frac{dt}{4})|}$$

As shown in Tables 5 and 6, the convergence ratios for some points are actually larger than 2. This may be caused by the sudden start of the fluids as the inflow changes from 0 to some nonzero values rapidly at $t = 0$. We also consider a smooth problem where the inflow condition is given by a combination of two Poiseuille flow $u(y,t) = 8e^{-t^3}y(1-y) + 6(1-e^{-t^3})y(1-y)$ and initially the flow in the channel is set

Table 6: dt-convergence in ω for passive vibration

	(x,y)=(2,0.5)			(x,y)=(2,0.25)		
dt	$\omega(x,y)$	$\lvert\omega(dt)-\omega(\frac{dt}{2})\rvert$	Ratio	$\omega(x,y)$	$\lvert\omega(dt)-\omega(\frac{dt}{2})\rvert$	Ratio
2^{-6}	-4.453	0.244	4.9	-0.243	6.987e-3	3.5
2^{-7}	-4.209	4.934e-2	6.9	-0.236	1.976e-3	5.5
2^{-8}	-4.160	7.117e-3	-	-0.234	6.366e-4	-
2^{-9}	-4.153	-	-	-0.233	-	-
	(x,y)=(4,0.5)					
2^{-6}	1.493	0.321	4.4			
2^{-7}	0.982	7.407e-2	3.3			
2^{-8}	1.056	2.449e-2	-			
2^{-9}	1.080	-	-			

Table 7: dt-convergence in ω for Poiseuille inflow

	(x,y)=(2,0.75)			(x,y)=(2,0.25)		
dt	$\omega(x,y)$	$\lvert\omega(dt)-\omega(\frac{dt}{2})\rvert$	Ratio	$\omega(x,y)$	$\lvert\omega(dt)-\omega(\frac{dt}{2})\rvert$	Ratio
2^{-6}	2.998613	2.924e-6	4.02	-2.998613	2.924e-6	4.02
2^{-7}	2.998615	7.272e-7	4.11	-2.998615	7.272e-7	4.11
2^{-8}	2.998617	1.768e-7	-	-2.9986177	1.768e-7	-
2^{-9}	2.998617	-	-	-2.998617	-	-

to be $u(x,y,t) = 8y(1-y)$. The problem is smooth in time and its derivatives at the beginning. We show the steady state solutions obtained at several locations in Table 7 and a second order convergence is achieved.

A.2 Convergence Study for Temperature Solver

In this section, we display the results of convergence tests with respect to dt and dx for the temperature solver. For a smooth problem, second order convergence is expected for both time and spatial variables. For all the numerical results obtained here, we use the following dimensionless parameters: the length of the channel $L = 4$, the height of the channel $H = 1$, $S_a = 1$ and $S_b = 0.5$. We choose the relative vortex strength $\Gamma_r = 6$ for the active vibration cases and $\Gamma_r = -0.6$ for the passive vibration.

Table 8: dx-convergence in T for active vibration

	(x,y)=(2,0.5)			(x,y)=(2,0)		
dx	$T(x,y)$	$\lvert T(dx) - T(\frac{dx}{2})\rvert$	Ratio	$\omega(x,y)$	$\lvert T(dx) - T(\frac{dx}{2})\rvert$	Ratio
2^{-6}	239.587	2.442	2.1	25577.178	14.592	2.5
2^{-7}	237.145	1.163	2.3	25562.586	5.837	2.8
2^{-8}	235.982	0.507	-	25556.745	2.085	-
2^{-9}	235.475	-	-	25554.660	-	-
	(x,y)=(2,-0.125)					
2^{-6}	25580.257	20.132	3.5			
2^{-7}	25560.125	5.752	3.4			
2^{-8}	25554.373	1.692	-			
2^{-9}	25552.681	-	-			

Table 9: dx-convergence in T for passive vibration

	(x,y)=(2,0.5)			(x,y)=(2,0.25)		
dx	$T(x,y)$	$\lvert T(dx) - T(\frac{dx}{2})\rvert$	Ratio	$T(x,y)$	$\lvert T(dx) - T(\frac{dx}{2})\rvert$	Ratio
2^{-6}	592.428	4.783	3.2	37869.573	40.258	2.6
2^{-7}	587.645	1.495	3.3	37829.315	14.378	2.8
2^{-8}	586.150	0.453	-	37814.937	5.135	-
2^{-9}	585.697	-	-	37809.802	-	-
	(x,y)=(2,-0.125)					
2^{-6}	37871.935	35.142	2.7			
2^{-7}	37836.793	13.016	3.0			
2^{-8}	37823.777	4.339	-			
2^{-9}	37819.438	-	-			

A.2.1 dx-Convergence

In Tables 8 and 9, we show the convergence results for spatial variables by comparing the value of T obtained at the center line of the channel $(x, y) = (2, 0.5)$, the wall temperature $(x, y) = (2, 0)$, and the interior point of the solid at $(x, y) = (2, -0.125)$. The time-periodic temperature is obtained by the numerical solver, and we show the value of T at the beginning of the period.

Tables 8 and 9 show the results for the active vibration and passive vibration respectively.

Table 10: dt-convergence in T for active vibration

	(x,y)=(2,0.5)			(x,y)=(2,0.25)		
dt	T	$\lvert T(dt) - T(\frac{dt}{2})\rvert$	Ratio	$T(x,y)$	$\lvert T(dt) - T(\frac{dt}{2})\rvert$	Ratio
2^{-6}	239.587	3.782	1.8	25577.178	20.862	2.1
2^{-7}	235.805	2.101	3.3	25556.216	9.934	2.2
2^{-8}	233.704	0.637	-	25546.282	4.516	-
2^{-9}	233.067	-	-	25541.766	-	-
	(x,y)=(2,-0.125)					
2^{-6}	25580.257	19.563	2.5			
2^{-7}	25560.634	7.825	2.1			
2^{-8}	25552.868	3.726	-			
2^{-9}	25549.142	-	-			

As shown in Tables 8 and 9, we obtain an order between 1 and 2. This is due to the singularity at the entrance. For the two points $x = 0, y = 0$ and $x = 0, y = 1$, the temperature satisfies both the far field temperature and the interface equation. Unlike the fluid solver, we are not able to obtain a smooth problem that still satisfies all requirements of the boundary conditions.

A.2.2 dt-Convergence

In Tables 10 and 11, we show the convergence results for time variables again by comparing the value of T obtained at certain locations at the beginning of a period. Tables 10 and 11 show the results for the active vibration and passive vibration respectively.

Similarly to the dx convergence result, we only obtain an order between 1 and 2 for the time variable. This is expected as the velocity is not smooth enough with respect to time variable.

Table 11: dt-convergence in T for passive vibration

	(x,y)=(2,0.5)			(x,y)=(2,0.25)		
dt	T	$\lvert T(dt) - T(\frac{dt}{2})\rvert$	Ratio	$T(x,y)$	$\lvert T(dt) - T(\frac{dt}{2})\rvert$	Ratio
2^{-6}	592.428	5.165	2.8	37869.573	20.476	2.5
2^{-7}	587.263	1.845	3.3	37849.097	8.190	2.5
2^{-8}	585.418	0.559	-	37840.907	3.276	-
2^{-9}	584.859	-	-	37837.631	-	-
	(x,y)=(2,-0.125)					
2^{-6}	37871.935	20.693	2.6			
2^{-7}	37851.247	7.959	3.0			
2^{-8}	37843.288	2.653	-			
2^{-9}	37840.635	-	-			

REFERENCES

[1] Acheson, D., *Elementary Fluid Dynamics*. Oxford Univ. Press, 1990.

[2] Açikalin, T., Garimella, S. V., Raman, A., and Petroski, J., "Characterization and optimization of the thermal performance of miniature piezoelectric fans," *International Journal of Heat and Fluid Flow*, vol. 28, no. 4, pp. 806–820, 2007.

[3] Açikalin, T., Wait, S. M., Garimella, S. V., and Raman, A., "Experimental investigation of the thermal performance of piezoelectric fans," *Heat Transfer Engineering*, vol. 25, no. 1, pp. 4–14, 2004.

[4] Alben, S., "Simulating the dynamics of flexible bodies and vortex sheets," *Journal of Computational Physics*, vol. 228, no. 7, pp. 2587–2603, 2009.

[5] Alben, S. and Shelley, M. J., "Flapping states of a flag in an inviscid fluid: bistability and the transition to chaos," *Physical Review Letters*, vol. 100, no. 7, p. 074301, 2008.

[6] Anderson, J., Streitlien, K., Barrett, D., and Triantafyllou, M., "Oscillating foils of high propulsive efficiency," *Journal of Fluid Mechanics*, vol. 360, pp. 41–72, 1998.

[7] Argentina, M. and Mahadevan, L., "Fluid-flow-induced flutter of a flag," *Proceedings of the National Academy of Sciences of the United States of America*, vol. 102, no. 6, pp. 1829–1834, 2005.

[8] Avila, K., Moxey, D., de Lozar, A.and Avila, M., Barkley, D., and Hof, B., "The onset of turbulence in pipe flow," *Science*, vol. 333, no. 6039, pp. 192–196, 2011.

[9] Baker, A., *Finite Element Computational Fluid Mechanics*. Taylor and Francis US, 1983.

[10] Biswas, G., *Introduction to Fluid Mechanics and Fluid Machines, 2e*. Tata McGraw-Hill Education, 2003.

[11] Borah, A., "Computational study of streamfunction-vorticity formulation of incompressible flow and heat transfer problems," *Applied Mechanics and Materials*, vol. 52, pp. 511–516, 2011.

[12] Briley, W., "A numerical study of laminar separation bubbles using Navier-Stokes equations," *Journal of Fluid Mechanics*, vol. 47, pp. 713–736, 1971.

[13] Buchholz, J. H. and Smits, A. J., "The wake structure and thrust performance of a rigid low-aspect-ratio pitching panel," *Journal of Fluid Mechanics*, vol. 603, pp. 331–365, 2008.

[14] Burggraf, O. R., "Analytical and numerical studies of the structure of steady separated flows," *Journal of Fluid Mechanics*, vol. 24, no. 01, pp. 113–151, 1966.

[15] Calmidi, V. and Mahajan, R., "Forced convection in high porosity metal foams," *Journal of Heat Transfer*, vol. 122, no. 3, pp. 557–565, 2000.

[16] Camarri, S. and Giannetti, F., "On the inversion of the von Kármán street in the wake of a confined square cylinder," *Journal of Fluid Mechanics*, vol. 574, pp. 169–178, 2007.

[17] Choi, S. U. and Eastman, J., "Enhancing thermal conductivity of fluids with nanoparticles," tech. rep., Argonne National Lab., IL (United States), 1995.

[18] Choi, S., Zhang, Z., Yu, W., Lockwood, F., and Grulke, E., "Anomalous thermal conductivity enhancement in nanotube suspensions," *Applied physics letters*, vol. 79, no. 14, pp. 2252–2254, 2001.

[19] Clements, R., "An inviscid model of two-dimensional vortex shedding," *Journal of Fluid Mechanics*, vol. 57, no. 02, pp. 321–336, 1973.

[20] Comini, G. and Manzan, M., "Inflow and outflow boundary conditions in the finite element solution of the stream function-vorticity equations," *Communications in Numerical Methods in Engineering*, vol. 11, pp. 33–40, 1995.

[21] Connell, B. S. and Yue, D. K., "Flapping dynamics of a flag in a uniform stream," *Journal of Fluid Mechanics*, vol. 581, pp. 33–67, 2007.

[22] Coutanceau, M. and Defaye, J.-R., "Circular cylinder wake configurations: A flow visualization survey," *Applied Mechanics Reviews*, vol. 44, no. 6, pp. 255–305, 1991.

[23] D'alessio, S. and Dennis, S., "A vorticity model for viscous flow past a cylinder," *Computers and fluids*, vol. 23, no. 2, pp. 279–293, 1994.

[24] E, W. and Liu, J., "Vorticity boundary condition and related issues for finite difference schemes," *Journal of Computational Physics*, vol. 124, no. 2, pp. 368–382, 1996.

[25] Fiebig, M., Kallweit, P., Mitra, N., and Tiggelbeck, S., "Heat transfer enhancement and drag by longitudinal vortex generators in channel flow," *Experimental Thermal and Fluid Science*, vol. 4, no. 1, pp. 103–114, 1991.

[26] Gerrard, J., "The mechanics of the formation region of vortices behind bluff bodies," *Journal of Fluid Mechanics*, vol. 25, no. 02, pp. 401–413, 1966.

[27] Gerty, D., Mahalingam, R., and Glezer, A., "Fluidic-driven ducted heat ejector," *Bulletin of the American Physical Society*, 2005.

[28] Gerty, D., Mahalingam, R., and Glezer, A., "Design and characterization of a heat sink cooled by an integrated synthetic jet matrix," in *The Tenth Intersociety Conference on Thermal and Thermomechanical Phenomena in Electronics Systems, 2006 (ITHERM'06)*, pp. 356–360, IEEE, 2006.

[29] Gerty, D., *Fluidic-driven Cooling of Electronic Hardware*. PhD dissertation, Georgia Institute of Technology, 2008.

[30] Godoy-Diana, R., Aider, J.-L., and Wesfreid, J. E., "Transitions in the wake of a flapping foil," *Physical Review E*, vol. 77, no. 1, p. 016308, 2008.

[31] Gresho, P., "Incompressible fluid dynamics: some fundamental formulation issues," *Annual Review of Fluid Mechanics*, vol. 23, pp. 413–453, 1991.

[32] Hackbusch, W., "Fast numerical solution of time-periodic parabolic problems by a multigrid method," *SIAM Journal of Scientific and Statistical Computing*, vol. 2, pp. 198–206, 1981.

[33] Hald, O., "Convergence of vortex methods for euler's equations," *SIAM Journal of Numerical Analysis*, vol. 16, pp. 726–755, 1979.

[34] Holman, J. P., *Heat Transfer*. McGraw-Hill, 1997.

[35] Jensen, V., "Viscous flow round a sphere at low Reynolds number ($\leq$ 40)," *Proceedings of the Royal Society of London. Series A*, vol. 249, pp. 346–366, 1959.

[36] Kiya, M. and Arie, M., "A contribution to an inviscid vortex-shedding model for an inclined flat plate in uniform flow," *Journal of Fluid Mechanics*, vol. 82, no. 02, pp. 223–240, 1977.

[37] Koochesfahani, M. M., "Vortical patterns in the wake of an oscillating airfoil," *AIAA Journal*, vol. 27, no. 9, pp. 1200–1205, 1989.

[38] Krasny, R., "Computation of vortex sheet roll-up in the Trefftz plane," *Journal of Fluid Mechanics*, vol. 184, pp. 123–155, 1987.

[39] Kumar De, A. and Dalal, A., "Numerical simulation of unconfined flow past a triangular cylinder," *International Journal for Numerical Methods in Fluids*, vol. 52, no. 7, pp. 801–821, 2006.

[40] Leonard, A., "Vortex methods for flow simulation," *Journal of Computational Physics*, vol. 37, pp. 289–335, 1980.

[41] Li, J. G., "A mechanism for heat transfer enhancements by vortex shedding," *Fluids Engineering Division Conference, FED, San Diego, California, ASME*, vol. 239, p. 533, 1996.

[42] Lienhard, J. H., *A Heat Transfer Textbook*. Courier Dover Publications, 2013.

[43] Lighthill, M., "Large-amplitude elongated-body theory of fish locomotion," *Proceedings of the Royal Society of London. Series B. Biological Sciences*, vol. 179, no. 1055, pp. 125–138, 1971.

[44] Liu, S.-F., Huang, R.-T., Sheu, W.-J., and Wang, C.-C., "Heat transfer by a piezoelectric fan on a flat surface subject to the influence of horizontal/vertical arrangement," *International Journal of Heat and Mass Transfer*, vol. 52, no. 11, pp. 2565–2570, 2009.

[45] Lu, T., "Heat transfer efficiency of metal honeycombs," *International Journal of Heat and Mass Transfer*, vol. 42, no. 11, pp. 2031–2040, 1998.

[46] Mallock, A., "On the resistance of air," *Proceedings of the Royal Society of London. Series A*, vol. 79, no. 530, pp. 262–273, 1907.

[47] Mancera, P. d. A. and Hunt, R., "Fourth–order method for solving the navier–stokes equations in a constricting channel," *International Journal for Numerical Methods in Fluids*, vol. 25, no. 10, pp. 1119–1135, 1997.

[48] Michelin, S., Llewellyn Smith, S. G., and Glover, B. J., "Vortex shedding model of a flapping flag," *Journal of Fluid Mechanics*, vol. 617, pp. 1–10, 2008.

[49] Napolitano, M., Pascazio, G., and Quartapelle, L., "A review of vorticity conditions in the numerical solution of the $\zeta - \psi$ equations," *Computers and Fluids*, vol. 28, pp. 139–195, 1999.

[50] Oertel Jr, H., "Wakes behind blunt bodies," *Annual Review of Fluid Mechanics*, vol. 22, no. 1, pp. 539–562, 1990.

[51] Ol'Shanskii, M. and Staroverov, V., "On simulation of outflow boundary conditions in finite difference calculations for incompressible fluid," *International Journal for Numerical Methods in Fluids*, vol. 33, no. 4, pp. 499–534, 2000.

[52] Perry, A., Chong, M., and Lim, T., "The vortex-shedding process behind two-dimensional bluff bodies," *Journal of Fluid Mechanics*, vol. 116, pp. 77–90, 1982.

[53] Perry, A., Chong, M., and Lim, T., "The vortex-shedding process behind two-dimensional bluff bodies," *Journal of Fluid Mechanics*, vol. 116, pp. 77–90, 1982.

[54] Peyret, R., *Spectral Methods for Incompressible Viscous Flow*, vol. 148. Springer, 2002.

[55] Peyret, R. and Taylor, T. D., "Computational methods for fluid flow," *New York, Springer-Verlag, 1985, 368 p.*, vol. 1, 1985.

[56] Saad, Y. and Schultz, M. H., "Gmres: A generalized minimal residual algorithm for solving nonsymmetric linear systems," *SIAM Journal on Scientific and Statistical Computing*, vol. 7, no. 3, pp. 856–869, 1986.

[57] Saffman, P., *Vortex Dynamics*. Cambridge Univ. Press, 1992.

[58] Salazar, A., "On thermal diffusivity," *European journal of physics*, vol. 24, no. 4, p. 351, 2003.

[59] Sani, R. and Gresho, P., "Résumé and remarks on the open boundary condition minisymposium," *International Journal for Numerical Methods in Fluids*, vol. 18, pp. 983–1008, 1994.

[60] Sarpkaya, T. and Schoaff, R. L., "Inviscid model of two-dimensional vortex shedding by a circular cylinder," *AIAA Journal*, vol. 17, no. 11, pp. 1193–1200, 1979.

[61] Schnipper, T., Andersen, A., and Bohr, T., "Vortex wakes of a flapping foil," *Journal of Fluid Mechanics*, vol. 633, pp. 411–423, 2009.

[62] Sharma, A. and Eswaran, V., "Heat and fluid flow across a square cylinder in the two-dimensional laminar flow regime," *Numerical Heat Transfer, Part A: Applications*, vol. 45, no. 3, pp. 247–269, 2004.

[63] Shelley, M. J. and Zhang, J., "Flapping and bending bodies interacting with fluid flows," *Annual Review of Fluid Mechanics*, vol. 43, pp. 449–465, 2011.

[64] Singha, S. and Sinhamahapatra, K., "Flow past a circular cylinder between parallel walls at low reynolds numbers," *Journal of Ocean Engineering*, vol. 37, pp. 757–769, 2010.

[65] Sutera, S. P. and Skalak, R., "The history of poiseuille's law," *Annual Review of Fluid Mechanics*, vol. 25, no. 1, pp. 1–20, 1993.

[66] Suzuki, H., Inoue, Y., Nishimura, T., Fukutani, K., and Suzuki, K., "Unsteady flow in a channel obstructed by a square rod (crisscross motion of vortex)," *International Journal of Heat and Fluid Flow.*, vol. 14, pp. 2–9, 1993.

[67] Suzuki, K. and Suzuki, H., "Instantaneous structure and statical feature of unsteady flow in a channel obstructed by a square rod," *International Journal of Heat and Fluid Flow*, vol. 15, pp. 426–437, 1994.

[68] Taneda, S., "Waving motions of flags," *Journal of the Physical Society of Japan*, vol. 24, no. 2, pp. 392–401, 1968.

[69] Tang, S. and Aubry, N., "On the symmetry breaking instability leading to vortex shedding," *Physics of Fluids (1994-present)*, vol. 9, no. 9, pp. 2550–2561, 1997.

[70] Tezduyar, T. and Liou, J., "On the downstream boundary conditions for the vorticity-stream function formulation of two-dimensional incompressible flow," *Computer Methods in Applied Mechanics and Engineering*, vol. 85, pp. 207–217, 1991.

[71] Tezduyar, T., Liou, J., and Ganjoo, D., "Incompressible flow computations based on the vorticity-stream function and velocity-pressure formulations," *Computers and Structures*, vol. 35, pp. 445–472, 1990.

[72] Thom, A., "The flow past circular cylinders at low speeds," *Proceedings of the Royal Society of London. Series A, Containing Papers of a Mathematical and Physical Character*, pp. 651–669, 1933.

[73] Triantafyllou, M. S., Techet, A. H., and Hover, F. S., "Review of experimental work in biomimetic foils," *IEEE Journal of Oceanic Engineering*, vol. 29, no. 3, pp. 585–594, 2004.

[74] Triantafyllou, M., Triantafyllou, G., and Yue, D., "Hydrodynamics of fishlike swimming," *Annual Review of Fluid Mechanics*, vol. 32, no. 1, pp. 33–53, 2000.

[75] Von Kármán, T., *Aerodynamics: Selected Topics in the Light of Their Historical Development*. Courier Dover Publications, 2004.

[76] Williamson, C. H., "Vortex dynamics in the cylinder wake," *Annual Review of Fluid Mechanics*, vol. 28, no. 1, pp. 477–539, 1996.

[77] Woods, L., "A note on the numerical solution of 4th order differential equations," *Aeronautical Quarterly*, vol. 5, no. 3, pp. 176–184, 1954.

[78] Young, J. and S. Lai, J. C., "Oscillation frequency and amplitude effects on the wake of a plunging airfoil," *AIAA Journal*, vol. 42, no. 10, pp. 2042–2052, 2004.

[79] Yu, W., France, D. M., Routbort, J. L., and Choi, S. U., "Review and comparison of nanofluid thermal conductivity and heat transfer enhancements," *Heat Transfer Engineering*, vol. 29, no. 5, pp. 432–460, 2008.

[80] Zhang, J., Childress, S., Libchaber, A., and Shelley, M., "Flexible filaments in a flowing soap film as a model for one-dimensional flags in a two-dimensional wind," *Nature*, vol. 408, no. 6814, pp. 835–839, 2000.

VITA

Xiaolin Wang was born on February 27, 1987 in Yantai, China to Chuanshu Sun and Jiancheng Wang. After receiving her Bachelor's degree of Mathematics in Peking University in July 2009, she moved to Atlanta where she attended Georgia Institute of Technology to pursue her Ph.D. degree. She was in the interdisciplinary program organized by school of Mathematics and school of Computational Science and Engineering, and she worked with Dr. Silas Alben on problems in computational fluid dynamics. Five year later, she earned her Ph.D. in August 2014. She'll be starting as a postdoc at University of Michigan.